Low Speed Open Loop Field Oriented Control for Permanent Magnet Machines

INSTITUTE OF ENERGY TECHNOLOGY

CONDUCTED BY GROUP PED4-1031
SPRING SEMESTER, 2011

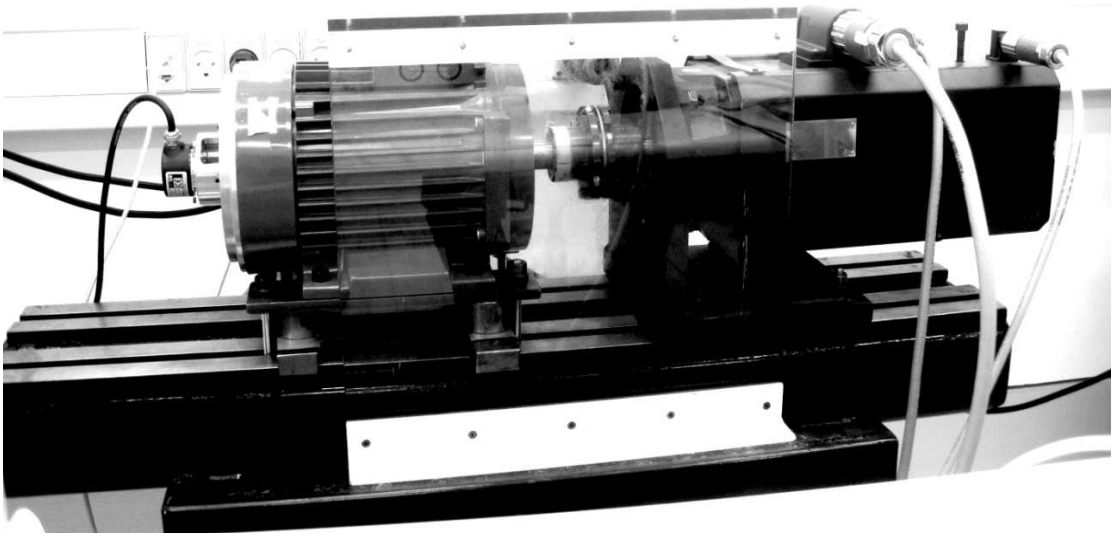

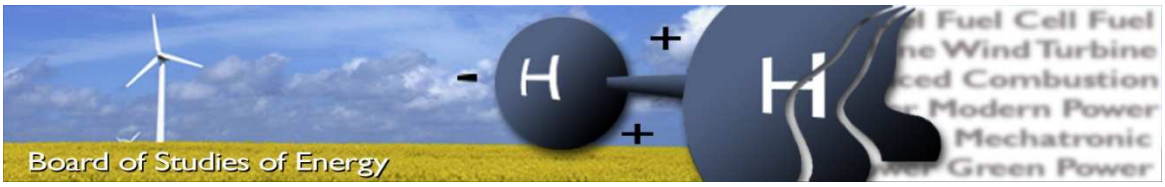

Title: Low Speed Open Loop Field Oriented Control for Permanent Magnet Machines
Semester: 10th semester
Semester theme: Master thesis
Project period: 1st February 2011 – 31th May 2011
ECTS: 30
Supervisor: Kaiyuan Lu
Project group: PED4 - 1031

_____
Javier Fernández Martínez

_____
Tatiana Pérez Soriano

SYNOPSIS:

Sensorless control of AC drives has been a field of research for many years. Nevertheless, sensorless control at zero speed is still a challenge, especially for surface mounted Permanent Magnet Synchronous Machines (sPMSM), where the magnet saliency is really small.

The main goal of this project is to develop a sensorless control for a sPMSM able to work in zero and low speed.

Literature about sensorless control strategies is studied and the suitability of the proposed estimator is tested by simulations and experimental tests in various operating conditions. The proposed estimator method is stable in low speed, including loading conditions.

High frequency signal injection method strategy was implemented using Danfoss power converter and dSpace as well as Matlab/Simulink.

Even the topic of the project is sensorless control the simulations and the laboratory was also carried in close loop, in order to compare the results.

Copies: 2
Pages, total: 93
Appendix: 6
Supplements: CD

By signing this document, each member of the group confirms that all participated in the project work and thereby that all members are collectively liable for the content of the report.

Preface

This dissertation is submitted to the faculty of Institute of Energy Technology at Aalborg University in the requirement for the credits of 10th semester M. Sc-Degree. The work and research documented in the project have been carried out by group PED4-1031 between the period of the 1st February and the 31th May at Aalborg University, Denmark.

The main idea of this project is to study sensorless control methods for low-speed operation of PMSM. High frequency signal injection method strategy was implemented, using Danfoss power converter and dSpace, as well as Matlab/Simulink.

Reading Instructions

The project is documented in a main report and appendixes. The main report can be read as a self-contained work, while the appendixes contain details about other data. In this project, the chapters are consecutively numbered whereas the appendixes are labelled with letters.

Figures, equations and tables are numbered in succession within the chapters. For example, Fig. 1.1 is the first figure in chapter 1.

The references are written with the “ISO-690” method. More detailed information about the sources is given at the end of the main report in references.

All simulations have been implemented in Matlab/Simulink and C-language .The laboratory work has been carried out in the dSpace laboratory, Pontoppidanstrade 109, Aalborg University.

A CD-ROM containing the main report, appendixes, the Matlab/Simulink models and the references is attached to the project.

Acknowledgements

The project has been skilfully supervised by Prof Kaiyuan Lu. We would like to strongly thank him, for his patience and generosity devoted valuable time and provided great help to the development of this work.

Furthermore, the help of Mads Lund is very much appreciated We gratefully appreciate all the guidance and professional support from Torben N. Matzen.

We would like to thank all the faculty of the Institute of Energy Technology for making this possible.

Index

List of figures

Nomenclature

Abbreviations

AC	Alternating Current
BPF	Bandpass filter
CTA	Constant Torque Angle
DC	Direct Current
EMF	Electromotive Force
FOC	Field Oriented Control
GM	Gain Margin
IM	Induction Machine
INFORM	Indirect Flux evaluation by Online Reactance Measurement
iPMSM	Interior Permanent Magnet Synchronous Motor
LPF	Low-pass filter
OMC	Optimal Modulus Criterion
OSM	Optimum Symmetric Method
PI	Proportional integral
PM	Phase Margin
PMSM	Permanent Magnet Synchronous Motor
PWM	Pulse Width Modulation
sPMSM	Surface Permanent Magnet Synchronous Motor
SVM	Space Vector Modulation
VSC	Voltage Source Converter

Symbols

S_x	Converter state values
V_{AN} , V_{BN} , V_{CN}	Phase voltages
V_{AB} , V_{BC} , V_{CA}	Line to line voltages
V_{DC}	DC-link voltage
v	Voltage
i	Current
T_{PWM}	Sampling period
T_1, T_2	Time active vectors
V_0, V_7,	Zero vectors
$V_1 - V_6$,	Active vectors
D_x	Duty cycles
L	Inductance
R	Resistance
ω	Angular speed
ϕ	Flux linkage
T	Torque
npp	Number of pole pairs
B	Viscous friction
θ	Rotor angle
J	Moment of inertia
T_s	Sampling time
k_{pi}	Proportional gain

k_{ii}	Integral gain
T_{ii}	Integrator time
f_s	Sampling frequency
T_q	Time constant of the motor
k	Inverse stator resistance
k_a	Anti-windup gain
ξ	Damping factor
n	Speed
$k_{p\hat{\omega}}$,, $k_{i\hat{\omega}}$	Proportional and integral gains of proportional-integral (PI) controller in rotor position estimator, respectively
p	Differential operator (*d/dt*)
$R(\tilde{\theta}_r)$	Coordinate transformation matrix $R(\tilde{\theta}_r) = \begin{bmatrix} cos\tilde{\theta}_r & sin\tilde{\theta}_r \\ -sin\tilde{\theta}_r & cos\tilde{\theta}_r \end{bmatrix}$
k_{err}	Coefficient of rotor position information signal
j	Operator ($1_{\llcorner \pi/2}$)
$\hat{\theta}_r$	Estimated rotor position (electrical)
$\hat{\omega}_r$	Estimated rotor speed
$\tilde{\theta}_r$	Rotor position estimation error (electrical)

Subscripts

α,β	Alpha and beta axis, respectively
d,q	*d* and *q* axis, respectively
s	Stator quantity
h	High frequency component
diff	Difference value between *d* and *q* axis
c	Cross-coupling component
avg	Average value between *d* and *q* axis
r	Rotor
e	Electrical
l	Load
n	Natural frequency of the system
m	Mutual
meas	Measured
ref	Reference
inj	Injected

Superscripts

*	Reference value
r	Actual rotor reference frame
$\hat{r}$	Estimated rotor reference frame

1. Introduction

This chapter introduces the background of the project, where the main advantages of the sensorless control are presented. Finally, the chapter is ended with a list of objectives, project motivation and limitations.

1.1. Background

Cost reduction and performance improvement are the main concerns in modern industry applications of electrical drives. Permanent Magnet (PM) machine drives have become the most promising candidates for their high performance, high efficiency and high torque to inertia ratio.

An essential requirement in controlling PM machines is to determine the rotor position information. Rotor shaft sensors are usually fitted, increasing the machine size, noise interferences, total cost and reliability reduction. These reasons lead to eliminate the position sensor and obtain the rotor position information indirectly. In fact the rotor position and speed can be estimated by the measured voltage and currents of the electrical motor. So the mechanical sensorless control is becoming a research focus (1).

Sensorless control of PMSM can be divided basically into two methods. The first one is based on the fundamental component model of the back-Electromotive force (EMF) for rotor position and speed detection, the second one is based on the saliency tracking (2). Back-EMF has good performance in medium and high speed but at low speed the voltage is really small or zero, for this reason some estimation schemes based on saliency phenomena of PM have been developed. Nevertheless, the control at low speed stills a challenge, especially in sPMSM because it is considered non salient. But a small amount of asymmetry is normally present due to the semi-insertion of the magnets, producing the stator inductance to be function of the rotor position (3).

1.1. Project motivation

The demand for variable speed drives in both low and high power applications has resulted in a great variety of products from different manufacturers, each offering a great variety of features. In this respect, the control strategy plays a great role in fulfilling the demands of each application

The operation of AC drives in speed open loop requires the estimation of internal state variables of the machine. This is done by measuring the currents or the voltages on the machine terminals. Low cost, medium performance sensorless drives can be designed using simple algebraic speed estimators. The adjustable speed drives employs various control methods to ensure satisfactory performances considering a specific application. The application with this project deals is low speed control of a current controlled PM motor by means of a Voltage Source Converter (VSC), in open loop. The control strategy should be capable to handle with load.

1.2. Objectives

The project should study different sensorless control strategies. The most promising must be simulate and implemented in a laboratory setup. The goal of the project proposal is to control a PM motor, by means of VSC, in open loop at low speed.

The main objectives of this project may be summarized as:

- Search literature about sensorless control strategies.
- Implement the selected control strategy in Matlab/Simulink.
- Control the sPMSM without using encoder
- Validate the simulations in the laboratory with dSpace.
- Test the performance of the control strategy in different study cases.
- Compare the results between close loop Field Oriented Control (FOC) and sensoreless control.
- Sensorless control strategy must be able to provide torque at low speed.

1.3. Project limitations

During this project, some limitations had to be considered and they are summarized as follows:

- Measurement of the real parameters of the motor in the laboratory was not done. The parameters from the datasheet were used.
- In simulation, some components are considered to be ideal and mechanical and electrical losses have been neglected.
- In sensorless control the maximum load torque that could be applied was 1 Nm.
- Zero speed under load conditions test was not achieved in the laboratory experiments.
- Large starting error form the angle estimator could not be neglected.

2. System description

In this chapter a general description of the whole system is presented. From the control point of view, the converter and the Space Vector Modulation (SVM) strategy are presented. Different characteristics of the sPMSM are presented and also a mathematical model in dq-frame has been developed.

2.1. Overview of the system

The PMSM is controlled using SVM. Fig. 2.1 shows the operation scheme. The system components are described in the next paragraphs, first the converter and the SVM strategy for determining the duty cycles. The second part is a description of the PMSM including the mathematical model.

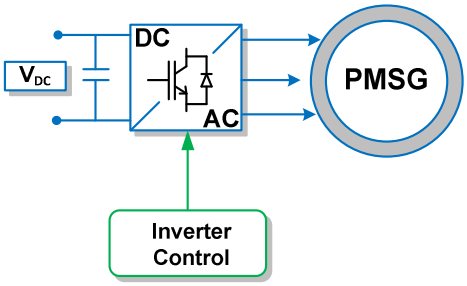

Fig. 2.1 Set up configuration

2.2. Voltage Source Converter

The main purpose of the VSC is to convert the DC voltage from the DC link into AC voltage. A simple scheme of the converter is presented in Fig. 2.2.

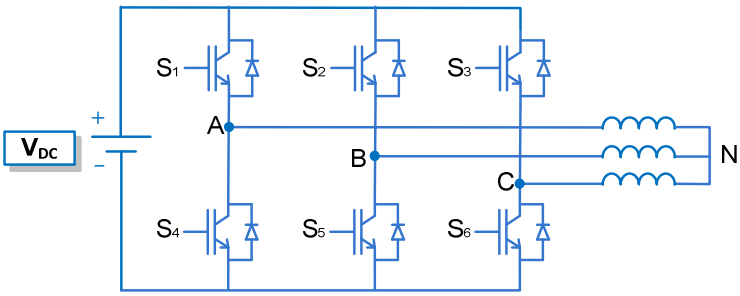

Fig. 2.2 Converter scheme

The converter has 6 semiconductors IGBT in three legs. There are two switches in each leg, which can have either a state value S_x of 1 (ON) or 0 (OFF). If one switch is turned on, the other from the same leg is turned off. Otherwise, a short circuit in the DC-link capacitor would be produced or the voltage in each terminal would be undetermined. Freewheeling diodes are used in order to create an alternative path for the reactive load current.

The line to line voltages of the converter are given by:

$$\begin{bmatrix} V_{AB} \\ V_{BC} \\ V_{CA} \end{bmatrix} = V_{DC} \begin{bmatrix} 1 & -1 & 0 \\ 0 & 1 & -1 \\ -1 & 0 & 1 \end{bmatrix} \begin{bmatrix} S_a \\ S_b \\ S_c \end{bmatrix} \qquad \textit{Eq 2.1}$$

When the same control principle is applied to all three phases of a converter feeding a balanced wye-connected load, the individual line-to neutral voltages V_{AN} , V_{BN} and V_{CN} are balanced too.

$$V_{AN} + V_{BN} + V_{CN} = 0 \qquad \textit{Eq 2.2}$$

Unconditionally

$$V_{AN} - V_{BN} = V_{AB} \qquad \textit{Eq 2.3}$$

And

$$V_{BN} - V_{CN} = V_{BC} \qquad \textit{Eq 2.4}$$

Solving Eq 2.2, Eq 2.3 and Eq 2.4 yields:

$$\begin{bmatrix} V_{AN} \\ V_{BN} \\ V_{CN} \end{bmatrix} = \frac{1}{3} \begin{bmatrix} 1 & 0 & -1 \\ -1 & 1 & 0 \\ 0 & -1 & 1 \end{bmatrix} \begin{bmatrix} V_{AB} \\ V_{BC} \\ V_{CA} \end{bmatrix} \qquad \textit{Eq 2.5}$$

And combined with Eq 2.1 the phase voltages can be expressed as a function of the DC-link voltage, where S_a S_b and S_c are the switching state values (4).

$$\begin{bmatrix} V_{AN} \\ V_{BN} \\ V_{CN} \end{bmatrix} = \frac{V_{DC}}{3} \begin{bmatrix} 2 & -1 & -1 \\ -1 & 2 & -1 \\ -1 & -1 & 2 \end{bmatrix} \begin{bmatrix} S_a \\ S_b \\ S_c \end{bmatrix} \qquad \textit{Eq 2.6}$$

2.3. Space Vector Modulation

In order to generate a rotating field, the converter has to be switched between six of the eight states. This mode of operation is called six-step mode.

Phase C	Phase B	Phase A	V_{ab}	V_{bc}	V_{ca}	V_{α}	V_{β}
0	0	0	0	0	0	0	0
0	0	1	V_{DC}	0	$-V_{DC}$	$2V_{DC}/3$	0
0	1	1	0	V_{DC}	$-V_{DC}$	$V_{DC}/3$	$V_{DC}/\sqrt{3}$
0	1	0	$-V_{DC}$	V_{DC}	0	$-V_{DC}/3$	$V_{DC}/\sqrt{3}$
1	1	0	$-V_{DC}$	0	V_{DC}	$-2V_{DC}/3$	0
1	0	0	0	$-V_{DC}$	V_{DC}	$-V_{DC}/3$	$-V_{DC}/\sqrt{3}$
1	0	1	V_{DC}	$-V_{DC}$	0	$V_{DC}/3$	$-V_{DC}/\sqrt{3}$
1	1	1	0	0	0	0	0

Table 2.1 Space vector (5)

There are two inactive states, this means that the voltage applied in the motor windings is null (000,111). The others are active states and produce output voltages (100,101,110,101,011,001) (6).

The vectors are represented by a hexagon in Fig. 2.3 and it is divided in six sectors. It can be noted that the zero vectors are located in the middle of the hexagon and can be used to regulate the amplitude of the space vector.

The angle between any two vectors is $\pi/3$. The length of active vectors has a maximum value of $2/3\, V_{DC}$ (7) and the maximum value of V^* is $1/\sqrt{3}\, V_{DC}$ (8). V* is the reference vector and can be decomposed into two components:

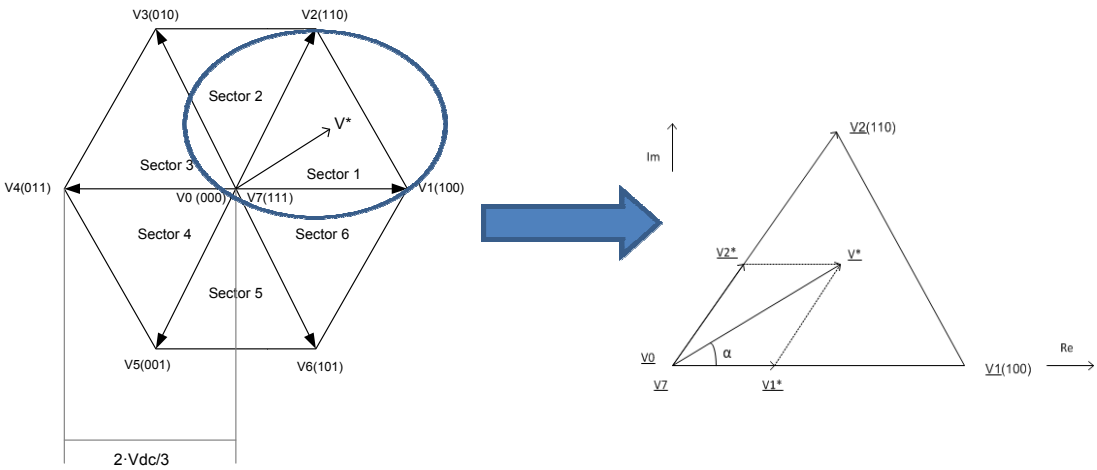

Fig. 2.3 Space vector representation in sector 1

Where $\overline{V}^* = \overline{V_1^*} + \overline{V_2^*}$

The reference vector can be expressed in a complex plane as in Eq 2.7.

$$\overline{V^*} = \overline{V_\alpha} + j\overline{V_\beta} \qquad \textit{Eq 2.7}$$

For example, in sector one, the sampling period is T_{PWM}, so the stator voltage is:

$$\overline{V}^* T_{PWM} = \overline{V_1} T_1 + \overline{V_2} T_2 + \frac{\overline{V_0} T_0}{2} + \frac{\overline{V_7} T_0}{2} \qquad \textit{Eq 2.8}$$

The voltage is determined by the vector sum of V_1, V_2 and zero vectors. The active vector time (T_1, T_2) can be expressed as a percentage of T_{PWM} (8).

$$T_1 = \sqrt{3}\frac{V^*}{Vdc} T_{PWM} \sin\left(\frac{\pi}{3} - \alpha\right) \qquad \textit{Eq 2.9}$$

$$T_2 = \sqrt{3}\frac{V^*}{Vdc} T_{PWM} \sin\alpha \qquad \textit{Eq 2.10}$$

The residual time is reserved for zero vectors V_0 and V_7. The condition is that $T_0 + T_1 + T_2 = T_{PWM}$. From Eq 2.11, Eq 2.12 and Eq 2.13, the duty cycles in sector 1 can be calculated.

$$D_a = \frac{T_1 + T_2 + \frac{T_0}{2}}{T_{PWM}} \qquad \textit{Eq 2.11}$$

$$D_b = \frac{T_2 + \frac{T_0}{2}}{T_{PWM}} \qquad \textit{Eq 2.12}$$

$$D_c = \frac{\frac{T_0}{2}}{T_{PWM}} \qquad \textit{Eq 2.13}$$

2.4. Permanent Magnet Synchronous Motor

PM machine is a synchronous machine which is excited by permanent magnets. The main advantage is that the excitation system is replaced by permanent magnets, which are located in the rotor (9). In this case having the magnets on the rotor the electrical losses of the machine are reduced.

In sPMSM, the magnets are mounted on the surface of the rotor. The magnets can be regarded as air because the permeability of the magnets is close to unity and the saliency is really small as a consequence of the same width of the magnets. From this is resulting that the inductances expressed in the quadrature coordinates are approximately equal ($L_d \approx L_q$).

The set of the equations in motoring mode, used to develop the model of the machine in *dq*-frame, is presented below (10). Where the flux, established by the permanent magnets in the stator, is sinusoidal, therefore the back-EMF is also sinusoidal. Fig. 2.4 shows the equivalent circuit of the machine in rotational frame.

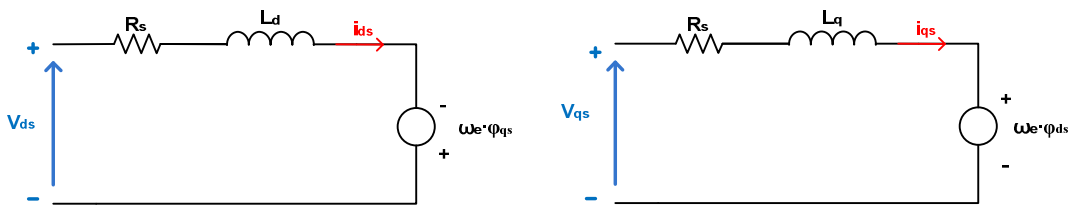

Fig. 2.4 Equivalent circuit of the generator in dq-frame

Voltage equations in *dq*-frame are:

$$V_{ds} = R_s \cdot i_{ds} + \frac{d}{dt}(\varphi_{ds}) - \omega_e \cdot \varphi_{qs} \qquad \textit{Eq 2.14}$$

$$V_{qs} = R_s \cdot i_{qs} + \frac{d}{dt}(\varphi_{qs}) + \omega_e \cdot \varphi_{ds} \qquad \textit{Eq 2.15}$$

Where V_{ds} and V_{qs} are the *dq-axis* stator voltages, i_{ds} and i_{qs}, the *dq-axis* stator currents, R_s represents the stator resistance and φ_{ds} and φ_{qs}, the *dq-axis* stator flux linkages.

Flux equations in *dq-frame* are:

$$\varphi_{qs} = L_q \cdot i_{qs} \qquad \textit{Eq 2.16}$$

$$\varphi_{ds} = L_d \cdot i_{ds} + \varphi_m \qquad \textit{Eq 2.17}$$

Where φ_m is the magnet mutual flux linkage and L_d and L_q are the inductances in *dq-axis*.

The electrical torque is:

$$T_e = \frac{3}{2} npp\left[\varphi_m i_{qs} + \left(L_d - L_q\right) i_{ds} i_{qs}\right] = \frac{3}{2} npp\left[\varphi_{ds} i_{qs} - \varphi_{qs} i_{ds}\right] \qquad \textit{Eq 2.18}$$

$$\frac{d}{dt}(\omega_r) = \frac{T_e - B\omega_r - T_l}{J} \qquad \textit{Eq 2.19}$$

$$\frac{d}{dt}(\theta_r) = \omega_r \qquad \textit{Eq 2.20}$$

Where ω_r is the rotor speed, θ_r, the rotor angle, B, the viscous friction, J, the moment of inertia and T_l, the load torque. The relation between the rotor speed and the electrical speed is expressed.

$$\omega_e = npp \cdot \omega_r \qquad \textit{Eq 2.21}$$

3. Control strategy

A description of the control design is presented for close loop and open loop. An overview of the conventional sensorless control schemes for PMSM is introduced. A detailed analysis of the chosen sensorless control strategy is presented.

3.1. Close loop Field oriented control

3.1.1. Field oriented control

The PMSM control methods can be divided into *scalar* and *vector control*. In scalar control, which is based on a relation valid for steady states, only the magnitude and frequency of voltage, currents and flux linkage space vectors are controlled. Contrary, in vector control, which is based on relation valid for dynamics states, not only magnitude and frequency, but also instantaneous position of voltage, current and flux space vectors are controlled. Thus, the control system achieves the position of the space vectors and guarantees their correct orientation for both steady states and transients.

One of the most popular vector control methods is FOC, which gives the PMSM high performance. In this method, the motor equations are transformed to a coordinate system that rotates in synchronism with PM flux. It allows, separately and indirectly, control of the flux and torque quantities by using current control loop with PI controllers, due to the stator current vector is split into two current components, i_{ds} and i_{qs}, which are flux and torque production currents respectively (11). Also a PI controller for commanding the speed is needed in the outer loop; the speed control can be achieved closing the loop by a feedback outside the inner torque control loop. The speed feedback can be derived from the same rotor angular position sensor, which is used to obtain the rotor position feedback (12). In Fig. 3.1, a general scheme of the FOC is presented.

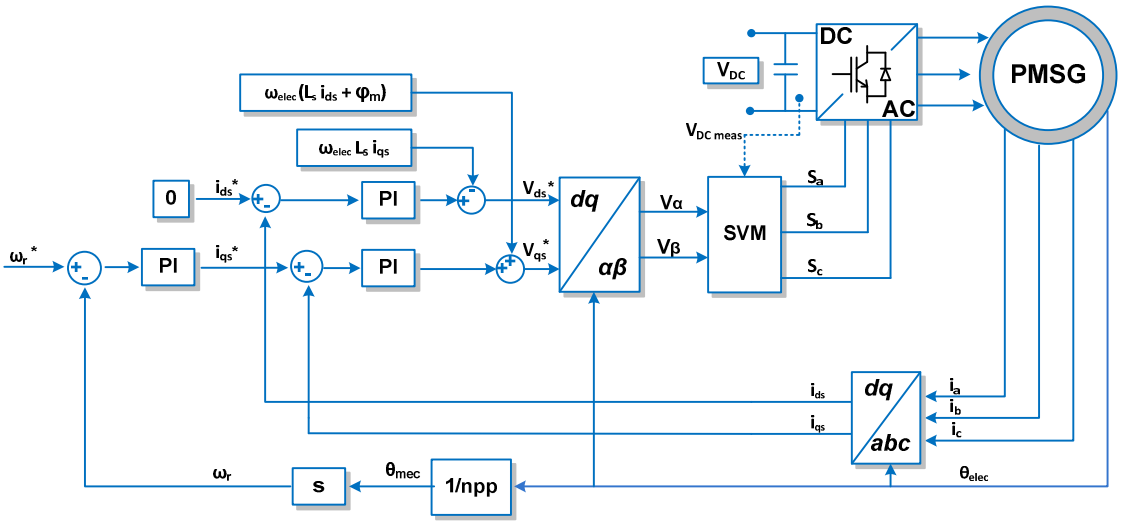

Fig. 3.1 General scheme of FOC

In Eq 2.18 can be noticed that a stator current feedback is required, due to the torque of the PMSM is related to the stator currents. The three phase measured stator currents are converted to *dq*-frame. This conversion provides the feedback currents i_{ds} and i_{qs}, which is possible because the shaft speed is determined by a sensor. Also a sensing of the DC-link voltage is required in order to feed the space vector algorithm.

There are many torque control strategies and the goal for all of them is to maintain a linear control over the torque. One of the easiest strategies and most widely used in the industry is Constant Torque Angle (CTA). The torque angle is defined as the angle between the *q-axis* current i_{qs} and the rotor permanent flux φ_m. This angle is maintained at $\pi/2$ in this control strategy. Whereas the *d-axis* current is maintained at zero, so the torque depends only on the amplitude of *q-axis* current (i_{qs}). The main advantage of this control strategy is that it simplifies the torque control mechanism by linearizing the relationship between torque and current. This means that a linear current controller results in linear control over torque as well (8). The implementation of this strategy can be noticed in Fig. 3.1, where the *d-axis* current reference is kept at zero.

The Eq 2.18 of the PMSM shows that there is a cross-coupling between the torque produced by the stator currents and the flux. In order to control i_{ds} when v_{ds} is changed the i_{ds} is changed as desired, but this causes to change the v_{qs}, and therefore the i_{qs}, which is not desirable. This degrades the control performance of the current control. To obtain better performance in current control the i_{ds} and the i_{qs} should be able to control independently. This can be achieved by a decoupling the cross-coupling in *dq*-frame. In Fig. 3.2 it can be seen the structure of the PI controllers with this decoupling control (12).

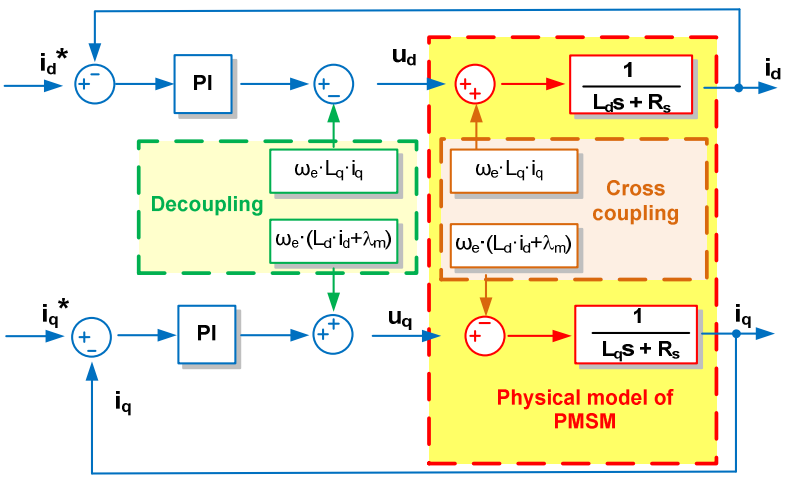

Fig. 3.2 Decoupling control

The transfer functions of the plants in *s-domain* are as follows:

$$\frac{I_d(s)}{U_d(s)} = \frac{1}{R_s + L_d s} \qquad \textit{Eq 3.1}$$

$$\frac{I_q(s)}{U_q(s)} = \frac{1}{R_s + L_q s} \qquad \textit{Eq 3.2}$$

3.1.2. Control design

In *q-axis,* there are two controllers, outer for the control of speed and inner for the control of the i_{qs} current. The structure of cascade loop can be observed in the general scheme Fig. 3.1.

The design of the controllers is limited to the selection of the regulator type (in this case PI) and the definition of optimal setting. Its parameters are selected according to the criterion adopted. The Optimal Modulus Criterion (OMC) and Optimal Symmetry Criterion (OSC) are commonly used in power electronics and drive control practice (8). The first one is used for tuning the inner loop and the second one for the outer one.

Firstly, the parameters of the i_{qs} current controller are determined, and then, the speed controller.

q-axis current controller

In Fig. 3.3, the structure of the *q-axis* current controller is presented, which is the inner loop.

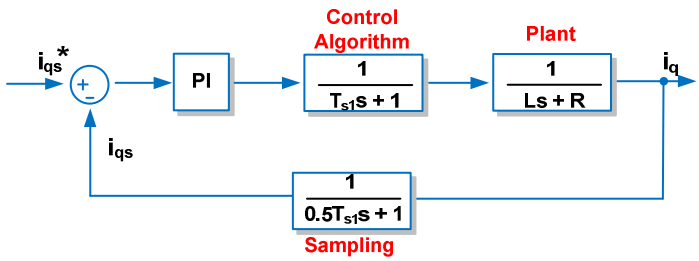

Fig. 3.3 q-axis inner loop

In order to work with a unitary feedback, the transfer function placed in the feedback can be moved. Fig. 3.4 shows the result of this displacement.

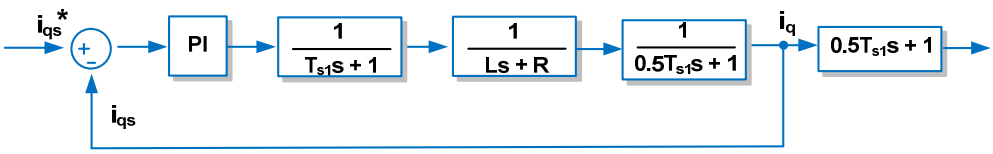

Fig. 3.4 q-axis current controller

The PI block offers a zero error in steady state and the transfer function of the controller is the ratio between the output signal and the error signal as shown Eq 3.3

$$G_{PI}(s) = \frac{U(s)}{E(s)} = k_{pi} + \frac{k_{ii}}{s} = k_{pi}\frac{1 + T_{ii}s}{T_{ii}s} \qquad \textit{Eq 3.3}$$

Where k_{pi} is the proportional gain, k_{ii} is the integral gain and T_{ii} is the integrator time, defined as the ratio between k_{pi} and k_{ii}.

$$T_{ii} = \frac{k_{pi}}{k_{ii}} \qquad \textit{Eq 3.4}$$

The control algorithm block is a delay introduced due to the digital calculation. The time constant T_{s1} is defined as $T_{s1} = \frac{1}{f_s} = \frac{1}{5k} = 0.2\ ms$ where f_s is the sampling frequency. The transfer function is shown in Eq 3.5.

$$G_{CA}(s) = \frac{1}{T_{s1}s + 1} \qquad \textit{Eq 3.5}$$

The plant transfer function is determined from the *dq* voltage equations after the decoupling is removed.

$$G_P(s) = \frac{i_q(s)}{u_q(s)} = \frac{1}{R_s + sL_s} = \frac{1}{R_s}\frac{1}{1 + s\frac{L_s}{R_s}} = \frac{k}{1 + sT_q} \qquad \textit{Eq 3.6}$$

Where T_q is the time constant of the motor and k is the inverse of the stator resistance.

$$k = \frac{1}{R_s} \qquad \textit{Eq 3.7}$$

$$T_q = \frac{L_s}{R_s} \qquad \textit{Eq 3.8}$$

The sampling block represents the delay introduced by the digital to analog conversion. Eq 3.9 shown the transfer function of the block.

$$G_S(s) = \frac{1}{0.5T_{s1}s + 1} \qquad \textit{Eq 3.9}$$

The open loop transfer function is defined as:

$$G_{OL} = G_{PI}(s) \cdot G_{CA}(s) \cdot G_P(s) \cdot G_S(s) \qquad \textit{Eq 3.10}$$

$$G_{OL} = k_{pi}\frac{1 + T_{ii}s}{T_{ii}s} \cdot \frac{1}{T_{s1}s + 1} \cdot \frac{k}{1 + sT_q} \cdot \frac{1}{0.5T_{s1}s + 1} \qquad \textit{Eq 3.11}$$

In order to simplify the transfer function a time constant is introduced, that represent all the delay because their values are really small compared with the electrical motor time constant, resulting that their dynamics are smaller. The transfer function of the delay will be replaced by a unique transfer function, and the time constant equal to the sum of all the constants of the system.

$$T_{si} = 1.5T_{s1} \qquad \textit{Eq 3.12}$$

With this assumption the open loop transfer function can be rewritten as:

$$G_{OL} = \frac{k_{pi}}{T_{ii}s} k \frac{1}{T_{si}s + 1} \qquad \textit{Eq 3.13}$$

To determine the proportional gain and the integral time of the controller OMC is used, and they are defined as:

$$k_{pi} = \frac{T_{ii}R_s}{2T_{si}} \qquad \textit{Eq 3.14}$$

$$T_{ii} = \frac{L_s}{R_s} \qquad \textit{Eq 3.15}$$

Considering the equations presented before the proportional and integral gains are defined as $k_{pi} = 3.66$ and $k_{ii} = 300$.

The analysis of the performance of the PI controller was carried out by using SISOtool. The Bode diagram in open and close loop and the root locus for the *q-axis* controller is shown in Fig. 3.5. The Gain Margin (GM) is 19.1 dB and the Phase Margin (PM) is 63.6 deg. Hence, the system for closed loop is stable. From the root locus, the value of the damping (ξ) can be known, that is the standard value of 0.707. The step response is presented in Fig. 3.6, where can be appreciated that the overshoot is 4.56% and the settling time is 2.29 ms.

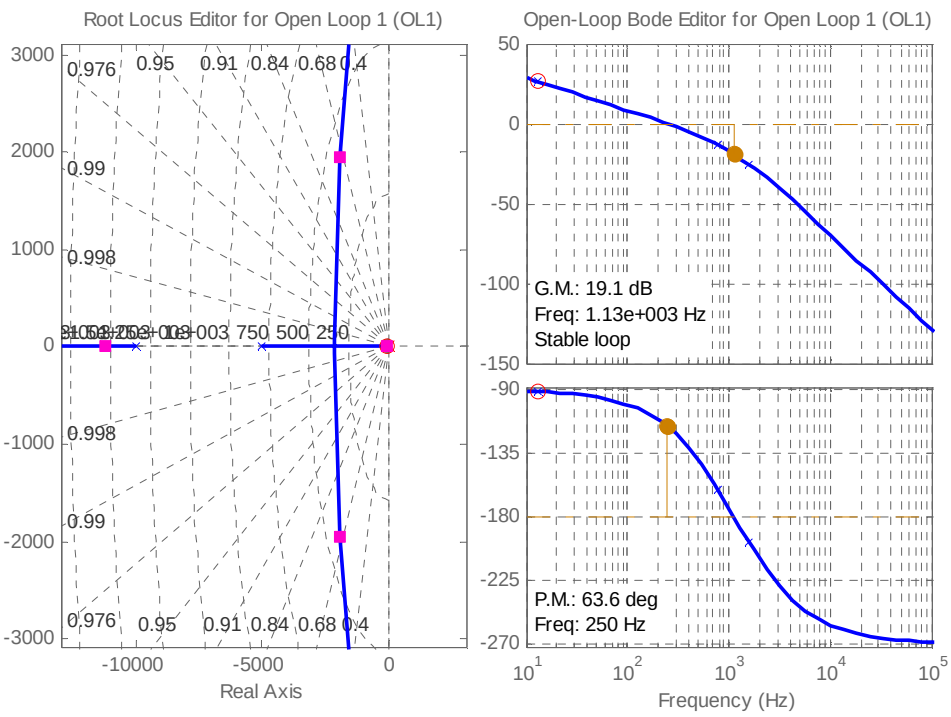

Fig. 3.5 Open and close loop Bode diagram and root locus for q-axis current controller

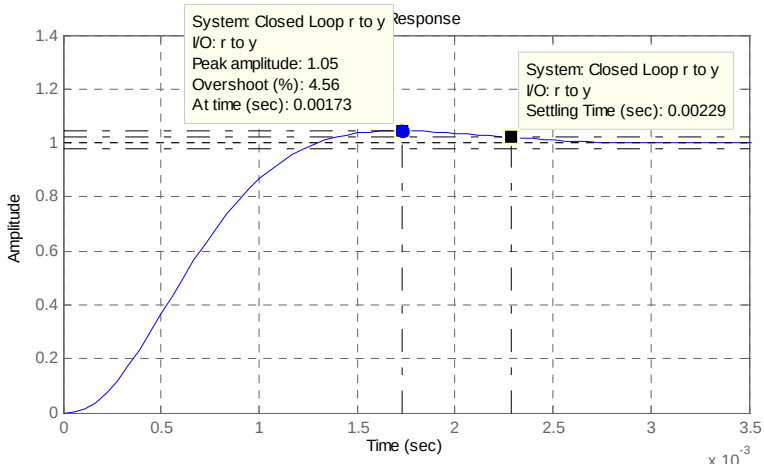

Fig. 3.6 Step response for q-axis current controller

The inner loop has to be very stable and robust regarding with a small change in the outer loop implies a big change in the inner one. Consequently the overshoot in the current controller should be minimized at least until a value of 2%. The new values for the proportional and integral gains are $k_{pi} = 3.1298$ and $k_{ii} = 256.08$. The performance of the new tuning is showed in Fig. 3.7 and Fig. 3.8. From the Bode diagram it can be seen that the GM is 20.5 dB and the PM is 67 deg. Hence, the system in close loop is more stable for the new parameters. From the root locus, the value of the damping (ξ) it has been increased until a value of 0.776 and the natural frequency of the system is ω_n= 403 Hz.

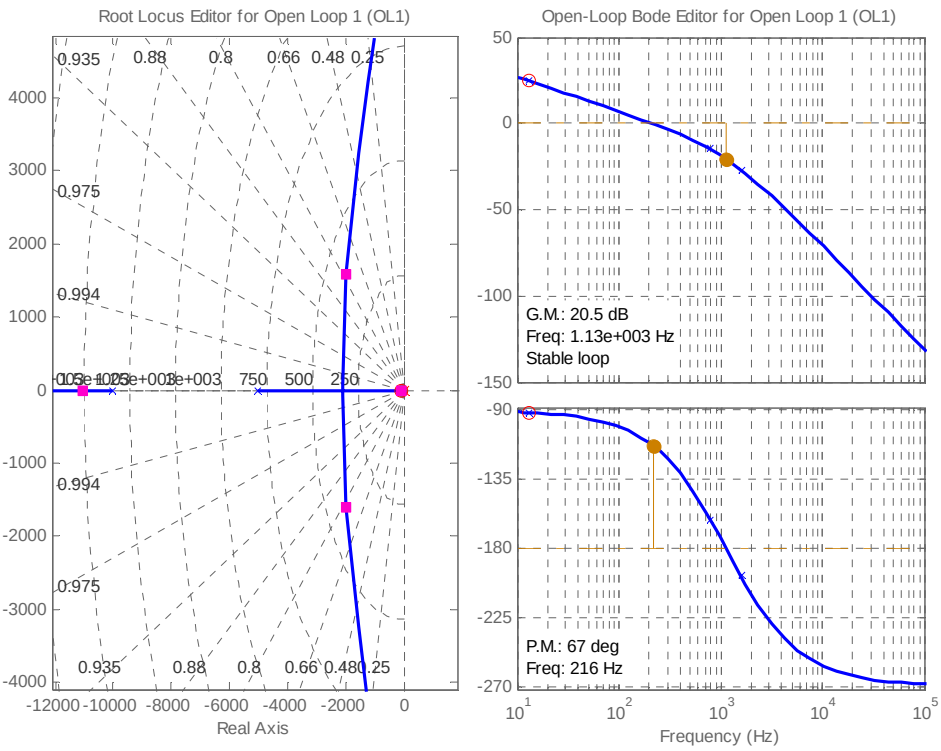

Fig. 3.7 Open and close loop Bode diagram and root locus for q-axis current controller

In Fig. 3.8 the step response for the new PI parameters is presented. From the figure it can be noticed a 2.01% of the overshoot and a settling time of 2.11 ms.

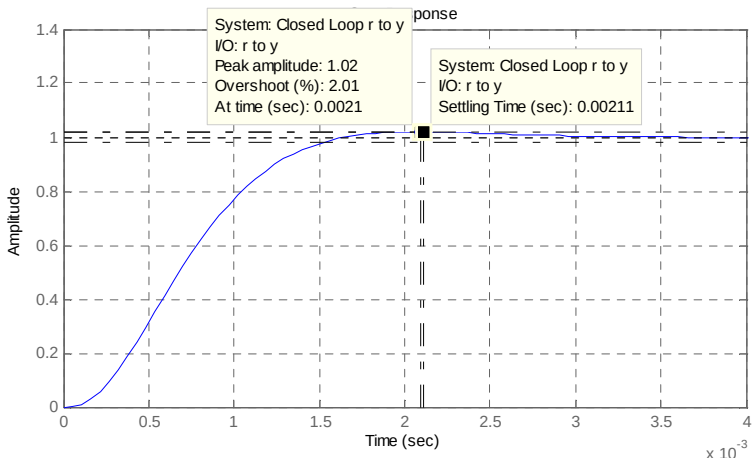

Fig. 3.8 Step response for q-axis current controller

q-axis speed controller

Once the inner controller is tuned with the desired performance, the outer controller can be also tuned. The speed loop is represented in Fig. 3.9.

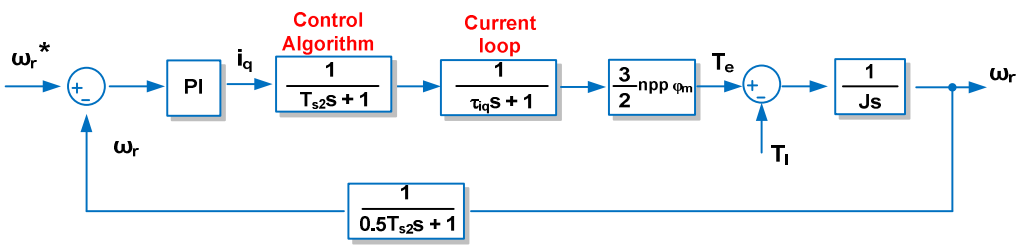

Fig. 3.9 q-axis speed controller structure

The transfer function of the speed control is determined by Eq 3.16.

$$G_{PI}(s) = k_{p\omega} + \frac{k_{i\omega}}{s} = k_{p\omega}\frac{1 + T_{i\omega}s}{T_{i\omega}s} \qquad \textit{Eq 3.16}$$

The effect of the inner loop has to be taken into account for a properly tuning. This effect can be modelled as a first order system.

$$G_{iqs}(s) = \frac{1}{\tau_{iq}\, s\, +\, 1} \qquad \textit{Eq 3.17}$$

Where $\tau_{iq} = \frac{T_{ii}}{K_{pi}\, k}$. The mechanical speed of the motor ω_r is determined from the mechanical equation $T_e - T_l = J\, s\, \omega_r + B\, \omega_r$, where $T_e = \frac{3}{2}\, npp\, \varphi_m i_{qs}$. The viscous friction can be negligible. The speed can be assumed as $\omega_r = \frac{1}{Js}\,(T_e - T_l)$.

In order to work with a unitary feedback, the transfer function placed in the feedback can be moved. Fig. 3.10 shows the result of this displacement.

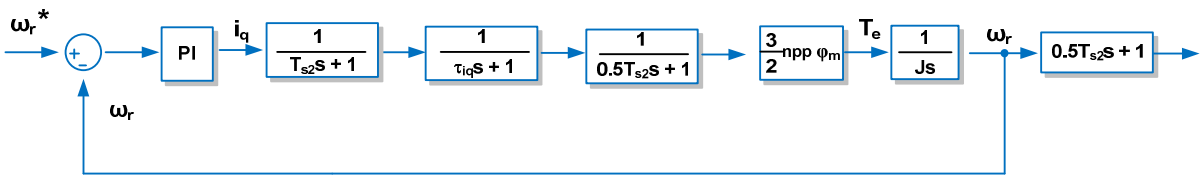

Fig. 3.10 q-axis speed controller structure with unity feedback

The open loop of the system above is:

$$G_\omega(s) = k_{p\omega}\frac{1+T_\omega s}{T_\omega s}\frac{1}{0.5\,T_{s2}+1}\frac{1}{\tau_{iq}\,s\,+\,1}\frac{1}{T_{s2}+1}\frac{3}{2}\,npp\,\varphi_m\frac{1}{Js} \qquad \textit{Eq 3.18}$$

For achieving higher simplification in the open loop transfer function, an equivalent time constant is assumed as:

$$T_{s\omega} = 1.5\,T_{s2} + \tau_{iq} \qquad \textit{Eq 3.19}$$

If $K_T = \frac{3}{2}\,npp\,\varphi_m$ the open loop transfer function yields:

$$G_\omega(s) = \frac{(1+T_{i\omega}s)K_T\,k_{p\omega}}{J\,T_{i\omega}\,s^2(T_{s\omega}s+1)} \qquad \textit{Eq 3.20}$$

The torque load is a disturbance in the system. For getting the appropriate response, a disturbance is introduced into the system. The tuning of the controller is carry out by the OSM (13). The general form of the OSM for open loop transfer function is:

$$G_{OSM}(s) = \frac{K_1K_pT_Is + K_1K_P}{s^2(T_1T_Is + T_I)} \qquad \textit{Eq 3.21}$$

The open loop transfer function for the speed controller has been modelled as

$$G_\omega(s) = \frac{\frac{K_T\,k_{p\omega}}{J}T_{i\omega}s + \frac{K_T\,k_{p\omega}}{J}}{s^2(T_{i\omega}T_{s\omega}s + T_{i\omega})} \qquad \textit{Eq 3.22}$$

From Eq 3.23 and Eq 3.24 the proportional and integral time constants can be obtained

$$k_{p\omega} = \frac{1}{2K_1T_1} = \frac{1}{2\frac{K_T}{J}T_{s\omega}} \qquad \textit{Eq 3.23}$$

$$T_{i\omega} = 4T_1 = 4\,T_{s\omega} \qquad \textit{Eq 3.24}$$

k_{pi} =3.2426 and T_{ii} = 0.004.

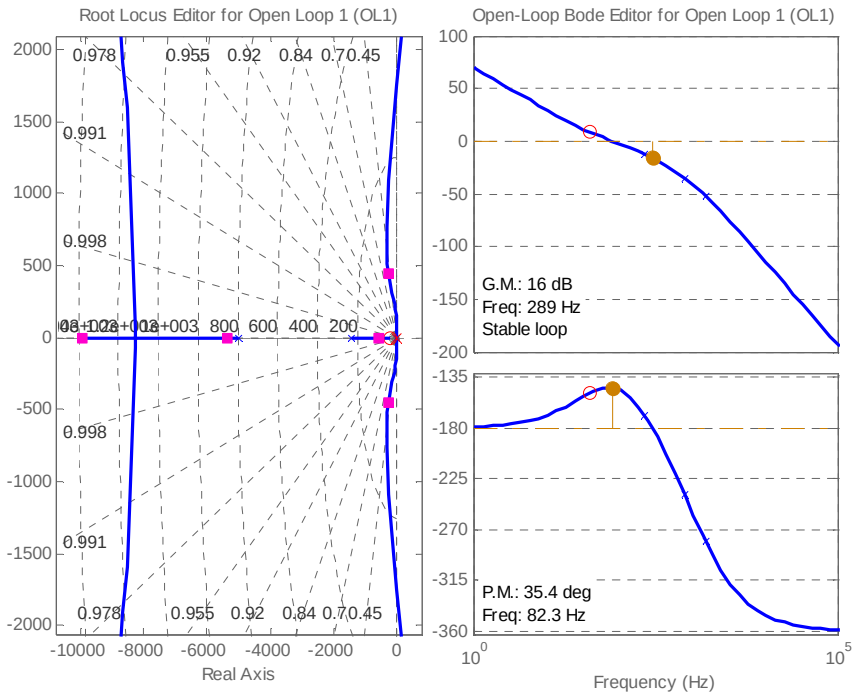

Fig. 3.11 Open and close loop Bode diagram and root locus for q-axis speed controller

The Bode diagram in open and close loop and the root locus for the *q-axis* speed controller is shown in Fig. 3.11. It can be observed that the PM value is 35.4 deg and the GM is 16 dB. Both positive, which means the loop is stable, and the value for the damping coefficient (ξ) is not the standard value of 0.707. The small value of the phase margin gives a step response with big overshoot as can be noticed in Fig. 3.12, where the value of the overshoot is 46 % and the value of the setting time is 15.7 ms.

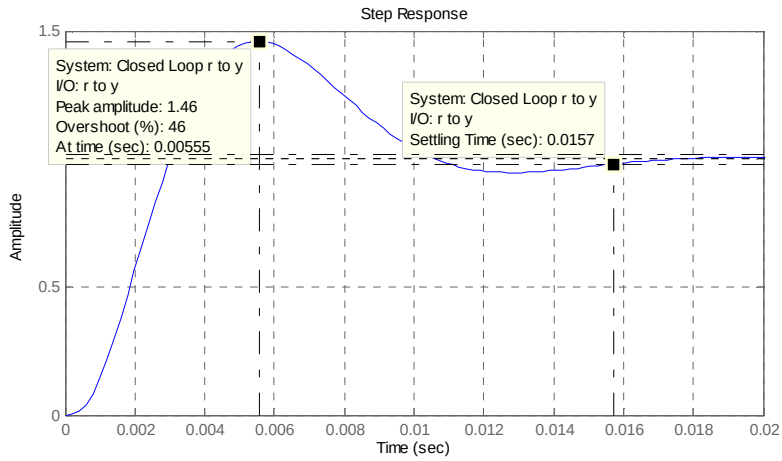

Fig. 3.12 Step response for q-axis speed controller

A new adjustment is required in order to reduce the value of the overshoot. Using the values from OSC as initial point, the new values for the speed controller were found by trial

and error, until obtain the desired performance. The new values for the adjusted PI are $k_{pi} = 1.9488$ and $k_{ii} = 199.9468$.

Fig. 3.13 and Fig. 3.14 the Bode diagram and the root locus are presented, in the first one, and the step response in the second one. From the Bode diagram it can be seen that the GM is 16 dB and the PM is 35.4 deg. Hence, the system is more stable with the new parameters. From the root locus can be determined the natural frequency of the system in ω_n=35.4 Hz. This is about 12 times less than the bandwidth of the current controller.

In Fig. 3.14 the step response of the speed for the new PI parameters is presented. From the figure it can be noticed that the overshoot is has been reduced until a value of 23.6 % and the settling time is 26.4 ms.

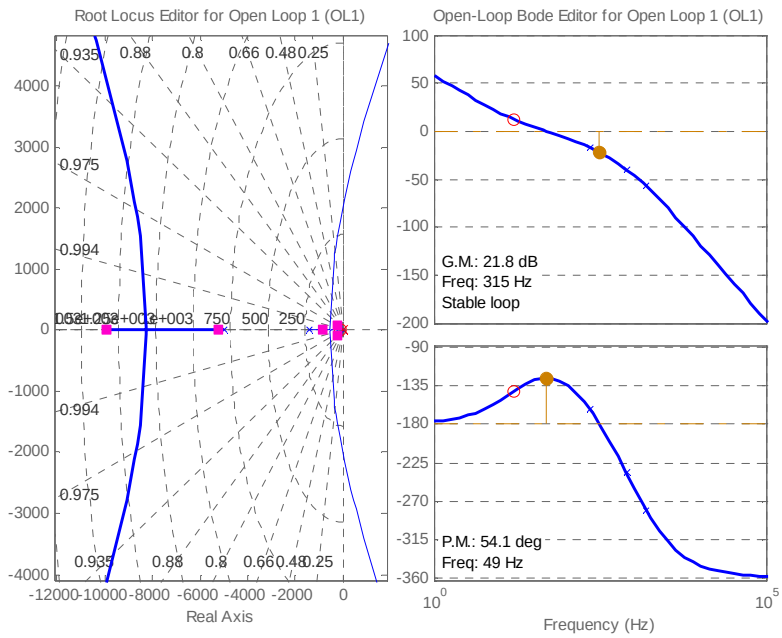

Fig. 3.13 Bode diagram of the speed controller

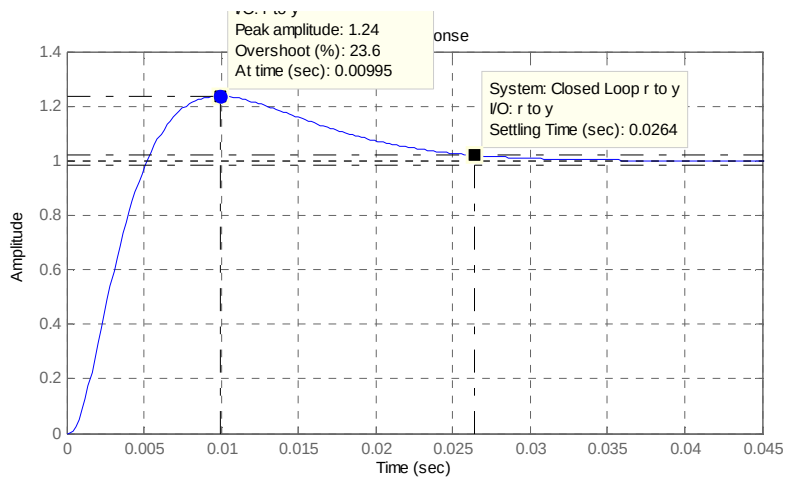

Fig. 3.14 Step response of the speed controller

d-axis current controller

The *d-axis* control loop has only one PI, which controls the i_{ds}. The structure of this PI is the same as the structure of i_{qs} current controller and the values are $k_{pi} = 3.33$ and $k_{ii} = 300$.

The analysis of the performance of the PI controller was carried out using SISOtool. The Bode diagram in open and close loop and the root locus for the *q-axis* controller is shown in Fig. 3.15. The GM is 19.1 dB and the PM is 63.6 deg. Hence, the system for closed loop is stable. From the root locus, the value of the damping (ξ) can be known, that is the standard value of 0.707. The step response is presented in Fig. 3.16, where can be appreciated that the overshoot is 4.56 % and the settling time is 2.29 ms.

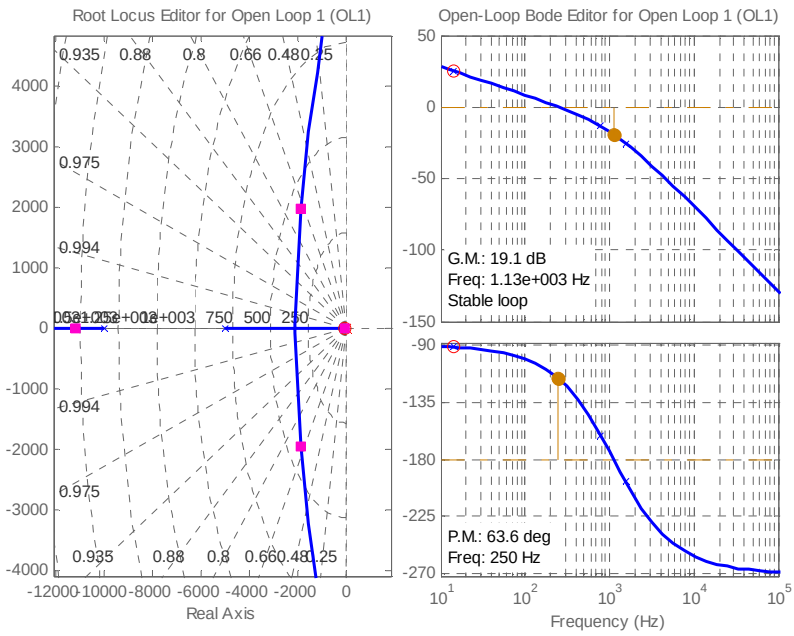

Fig. 3.15 Open and close loop Bode diagram and root locus for d-axis current controller

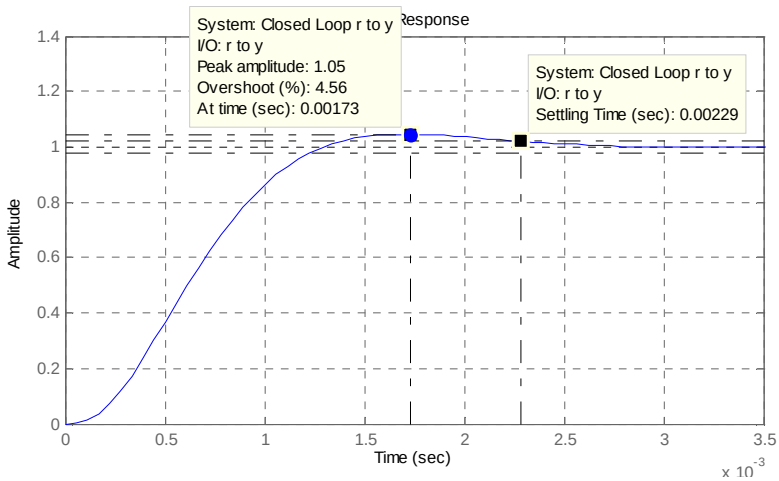

Fig. 3.16 Step response for d-axis current controller

In the same way as the *q* current controller, the *d* axis current controller has to be re-tuned in order to get a smaller overshoot. The new parameters for the PI are $k_{pi} = 2.8359$ and $k_{ii} = 255.231$. The performance of the new tuning is showed in Fig. 3.17 and Fig. 3.18. From the Bode diagram it can be seen that the GM is 20.5 dB and the PM is 67.1 deg. Hence, the system for closed loop is more stable with the new parameters. From the root locus, the value of the damping (ξ) it has been increased until a value of 0.776 and the natural frequency of the system in ω_n=402 Hz.

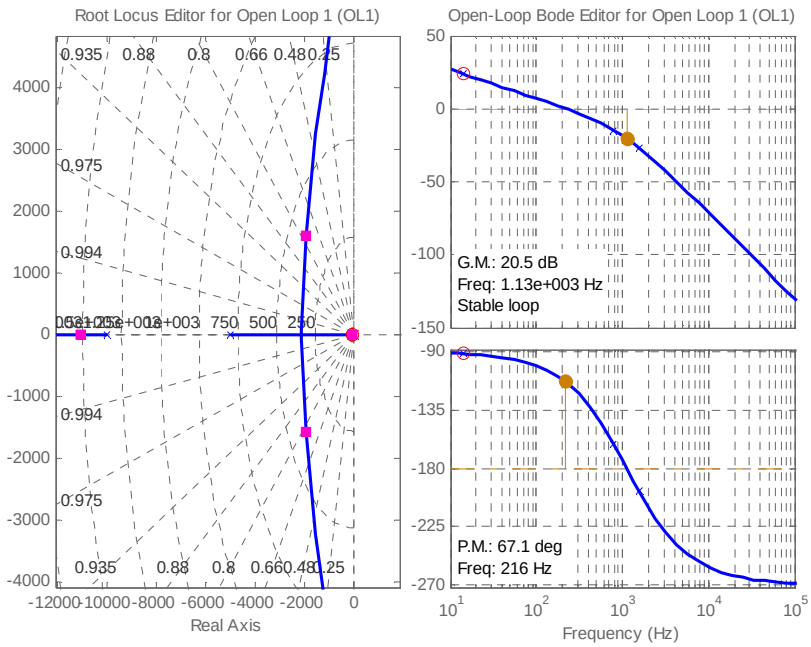

Fig. 3.17 Open and close loop Bode diagram and root locus for d-axis current controller

In Fig. 3.18 the step response for the new PI parameters is presented. From the figure it can be noticed a 1.97% of the overshoot and a settling time of 2.1 ms.

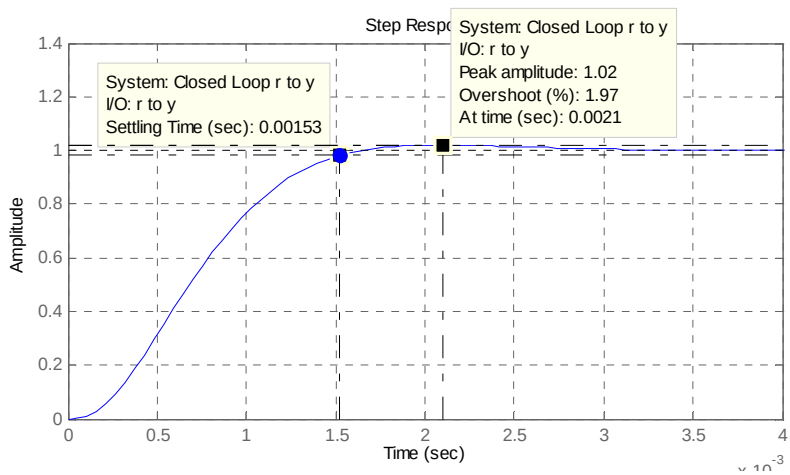

Fig. 3.18 Step response for d-axis current controller

3.1.3. Anti-windup

In any control system the output of the actuator can be saturate because the dynamic range of all real actuators is limited. Whenever actuator saturation happens, the control signal of the process stops changing and the feedback path is effectively opened. If the error signal continues to be applied to the integral input under these conditions, the integrator stored value will grow (wind up) until the sign of the error changes and the integrator turns around.

The result can be a very large overshoot because the output must grow to produce the necessary unwinding error and the result is a poor transient response. In effect, the integrator is an unstable element in open loop and must be stabilized when saturation occurs. The solution to this problem is an integrator anti-windup circuit, which "turns off" the integral action when the actuator saturates (14). In Fig. 3.19 an anti-windup scheme is for a PI controller shown.

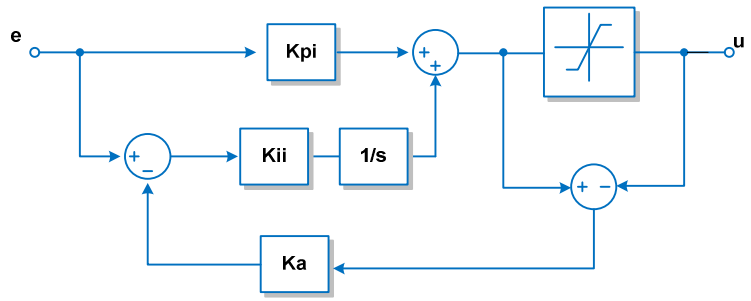

Fig. 3.19 Scheme for controller with antiwindup and saturation block

In this scheme, as soon as the actuator saturates, the feedback loop around the integrator becomes active and acts to keep the input to the integrator a small value. During this time the integrator essentially becomes a fast first order lag.

The anti-windup gain, k_a, should be chosen to be large enough that the anti-windup circuit keeps the input to the integrator small under all error conditions. The effect of the anti-windup is to reduce both the overshoot and the control effort in the feedback system.

The effect of anti-windup in the controller strategy is show in Fig. 3.20. In order to saturate the speed controller a large step of 300 rpm was commanded and the speed response is measured with and without anti-windup in the PI controller. In the Fig. 3.20 it may be noticed that without anti-windup circuit the response has a big overshoot and poor transient response as is showed in the zoomed part.

The values are determined by the comparison of anti-windup signal after the gain k_a and the error which feeds the integral action. The values of the gain of anti-windup are, for speed controller $k_a = 2.7$, and for current controllers is the same $k_a = 0.63$.

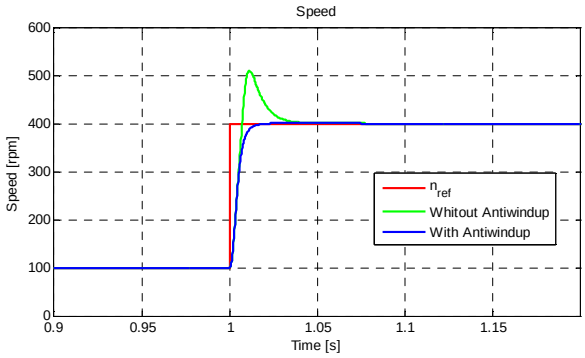

Fig. 3.20 Effect of the response of the system with and without antiwindup scheme for a step in the speed reference of 300 rpm

3.2. Sensorless Field Oriented Control

3.2.1. Sensorless control

The control of AC machines requires the knowledge of the rotor position and speed information. For this reason, position sensors as an encoder are required for determine the rotor position.

In some applications the presence of these sensors presents some disadvantages as reliability, machine size, noise interferences and cost. Therefore, there has been much research on eliminating the rotor position sensor mounted on the rotor of the PM machine and obtain the rotor position information indirectly.

A sensorless control is composed of the control system and the estimator algorithm which calculates the mechanical feedback information. Speed and position estimators can be allocated to three main categories (15).

- Model based estimators: These methods use the model of the machine and the measured electrical quantities to determine the rotor position and speed. The measured electrical quantity is usually the stator current of the AC machine. Model based methods are divided into the next categories:

  -State Observers

  -Back-EMF methods

  -Flux linkage methods

- Signal injection estimators: An additional signal (voltage or current) is injected into the motor and the position angle and speed are determined by processing the resulting currents or voltages. Injection methods can be divided in two groups.

  -*High frequency*: These estimators exploit the magnet saliency of the machine. The injection signal is between hundred of Hz to kHz, that means that the resistance in the motor can be neglected and the current will depend only on

the inductance. Problems that will arise at zero and low speed are low signal to noise ratio on the resulting currents making the measurements sensitive to for example noise and non-linearity in the converter (16).

-*Low frequency:* These estimators are based on the mechanical vibration of the rotor. The method uses frequencies between few Hz to few hundred Hz.

- Soft computing estimators: Use neural networks, fuzzy logic or genetic algorithms to estimate the speed and position. Neural networks learn the properties of the particular machine using predetermined training data.

One of the most mature methods is the back-EMF estimator, it has good performance in medium and high speed range. Due the magnitude of the back-EMF voltage is proportional to the speed , when the rotor rotates at low speed the magnitude of the voltage is very small or zero. (3). In order to overcome this drawback extensive research has been carried out to develop estimators where the problems at low speed can be avoided. These methods also suitable at zero speed are called injection methods.

In salient machines voltage test signals can be injected and the resulting currents processed to obtain the rotor position estimation, independent to the back-EMF. The test signal can be continuous high frequency voltage, discrete voltage pulses or modified Pulse Width Modulation (PWM) pulses (17). Nevertheless, sensorless control at zero speed is still a challenge, especially for sPMSM, where the magnet saliency is really small.

PMSM said to be salient if the stator inductance measured in the direction of the flux L_d is different to the inductance measured in the direction of the torque producing axis L_q. PMSM is generally considered to have symmetrical rotor, but a small amount of geometrical asymmetry is normally present due to the semi-insertion of the magnets into the rotor iron. In a sPMSM with semi inserted magnets, as shown Fig. 3.21, the extra iron in the quadrature magnetic path *q* and the stator's teeth saturation in the flux direction *d* results in small saliency in the effective air gap length. As a result, the inductance in the flux axis L_d is smaller than the inductance in the quadrature axis L_q producing the stator inductance to be function of the rotor position (18).

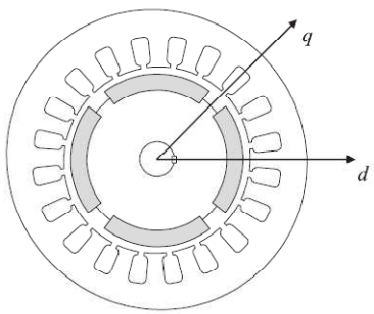

Fig. 3.21 Surface permanent magnet machine with semi-inserted magnets

3.2.2. High frequency signal injection methods

These techniques are specially used in interior Permanent Magnet Synchronous Motor (iPMSM) due the high saliency ratio, however this might be used with sPMSM exploiting the small saliency produced by the saturation effect of the stator core, due to the permanent magnet flux (19) saturate the stator iron in *d-axis,* increasing the effective air gap and decreasing the inductance in that direction. If L_d and L_q are not the same the stator voltage length changes and the direction of the resulting current vector is not the same.

In this method a high frequency signal, higher than the nominal angular speed, is injected into the motor and the position angle and speed are determined by processing the resulting currents or voltages. The injection can be continuous when a sinusoidal signal is added with superposition on top of the fundamental voltage reference and the SVM is not interrupted. In discontinuous injection the normal modulation is stopped at regular intervals and test pulses are injected into the motor, modifying the fundamental PWM pattern to contain a voltage pulse the rotor position can be tracked (16).

The types of high frequency injection estimators are briefly discussed in the following sections (15).

- <u>Periodic injection signal created by the modified PWM</u>

  It is known as INFORM method (INdirect Flux evaluation by Online Reactance Measurement) and is consider as a quite mature method. The basic idea is that the signal injection is performed by modifying the PWM operation. At constant intervals the PWM is stopped and a test voltage vector is injected into the motor. The change of the phase currents during the test voltage injection is measured. Voltage and current information is used to determine the reactance in a complex plane, this INFORM reactance contains the information of the rotor position.

- <u>Continuous signal superimposed on the fundamental frequency excitation signals</u>

  Continuous injection methods do not need any modification of the PWM. A high frequency voltage or current signal is superimposed on the fundamental frequency excitation signals. The waveform of the injected signal is usually sinusoidal and the frequency may vary from few hundred Hz to kHz. The amplitude of the resulting high frequency currents are modulated by the machine anisotropies. The position into is extracted from the measured stator current or the stator voltage waveform. Continuous inject estimator can be divided into two subcategories by the reference frame in which the signal is injected.

  -<u>*αβ-Stationary reference frame*</u>: A high frequency voltage vector with constant amplitude is added to the fundamental frequency voltage reference vector in stationary *αβ* reference frame. The injected voltage vector has constant angular speed and amplitude if is observed from the motor terminals. The resulting current vector has constant angular speed but the amplitude is modulated by the motor saliency.

Current components with injection frequency are extracted from the measured currents using filters. Phase locked loop type tracking algorithm or simple arctan function is used to estimate the speed and position. The principal is to detect the maximum and minimum values of the high frequency current vector and comparing it to the angle of the carrier voltage vector. The rotor position can be solved because the amplitude of the extract current vector is a trigonometric function of the angle difference.

The voltage injection is recommended because the current control does not interfere with the high frequency signal added to the output of the current controllers. If the carrier signal is added to the current references the bandwidth of the current control limits the performance of the estimator. Another approach is to measure the stator voltages instead of currents and prove the zero voltage term. But usually voltages are not measured in industrial applications.

-*dq-Rotating reference frame:* A constant amplitude sinusoidal high frequency voltage signal is added to the voltage reference vector in the estimated reference frame. The method is also called pulsating injection because the injected voltage has both positive and negative sequence components. The signal processing method used to extract position and speed information is similar to *αβ* injection method. The carrier is usually injected to the estimated *d-axis* direction because if only the *d-axis* flux linkage oscillates the acoustic noise is minimised because no torque is produced. If the injected frequency is in the kHz region, the stator resistance is negligible.

3.2.3. High frequency signal injection method injecting in rotating reference frame

When the rotor rotates at low speed the magnitude of the back-EMF voltage is very small or zero and it cannot be used for estimate the rotor position, for this reason a scheme based on the saliency phenomena is used. A high frequency fluctuating voltage signal is injected into the machine in order to detect the saliency phenomena by superimposing to the fundamental excitation signals.

This sensorless control scheme is not based on the saturation from the fundamental excitation but is based on the magnetic saliency due to the saturation from the PM flux by injection high frequency voltage signal in order to detect the magnetic saliency (3).

3.2.3.1. Simplified high frequency model of the PMSM

The voltage equations in the actual reference frame presented in 2.4 can be rewritten as Eq 3.25 were *p* is the differential operator.

$$\begin{bmatrix} v_{ds}^r \\ v_{qs}^r \end{bmatrix} = \begin{bmatrix} R_s + L_s p & -\omega_r L_s \\ \omega_r L_s & R_s + L_s p \end{bmatrix} \begin{bmatrix} i_{ds}^r \\ i_{qs}^r \end{bmatrix} + \begin{bmatrix} 0 \\ \omega_r \varphi_m \end{bmatrix} \qquad \textit{Eq 3.25}$$

If the high frequency components are only produced by the high frequency signal injection the second term on the right hand side can be neglected due it does not have any

high frequency component. The cross-coupling terms can be neglected in steady state if the frequency of the injected signal is sufficiently high compared to the rotor speed because time derivative terms of the current are proportional to the high frequency. Considering these simplifications the voltage equations of the high frequency components can be expressed as Eq 3.26.

$$\begin{bmatrix} v_{dsh}^r \\ v_{qsh}^r \end{bmatrix} = \begin{bmatrix} r_{dh}^r + L_{dh}^r p & 0 \\ 0 & r_{qh}^r + L_{qh}^r p \end{bmatrix} \begin{bmatrix} i_{dsh}^r \\ i_{qsh}^r \end{bmatrix} \qquad \textit{Eq 3.26}$$

Where v_{dsh}^r, v_{qsh}^r and i_{dsh}^r, i_{qsh}^r are the high frequency components of *dq-axis* voltages and currents in the actual rotor reference frame. r_{dh}^r, r_{qh}^r and L_{dh}^r, L_{qh}^r are *dq-axis* resistances and inductances at high frequency in the actual rotor reference frame.

Using the frequency of the injected high frequency voltage signal the Eq 3.26 can be expressed as Eq 3.27 in steady state.

$$\begin{bmatrix} v_{dsh}^r \\ v_{qsh}^r \end{bmatrix} = \begin{bmatrix} r_{dh}^r + j\omega_h L_{dh}^r & 0 \\ 0 & r_{qh}^r + j\omega_h L_{qh}^r \end{bmatrix} \begin{bmatrix} i_{dsh}^r \\ i_{qsh}^r \end{bmatrix} \equiv \begin{bmatrix} z_{dh}^r & 0 \\ 0 & z_{qh}^r \end{bmatrix} \begin{bmatrix} i_{dsh}^r \\ i_{qsh}^r \end{bmatrix} \qquad \textit{Eq 3.27}$$

Where z_{dh}^r and z_{qh}^r are the *dq-axis* high frequency impedances in the actual rotor reference frame. In sensorless operation the estimated rotor reference frame should be used instated of the actual one because the actual rotor position cannot be known. If the rotor position error is defined as $\tilde{\theta}_r \equiv \theta_r - \hat{\theta}_r$ the high frequency voltage equations in the estimated rotor reference frame can be expressed as Eq 3.28.

$$\begin{bmatrix} v_{dsh}^{\hat{r}} \\ v_{qsh}^{\hat{r}} \end{bmatrix} = R(\tilde{\theta}_r)^{-1} \begin{bmatrix} z_{dh}^r & 0 \\ 0 & z_{qh}^r \end{bmatrix} R(\tilde{\theta}_r) \begin{bmatrix} i_{dsh}^{\hat{r}} \\ i_{qsh}^{\hat{r}} \end{bmatrix} \qquad \textit{Eq 3.28}$$

$$= \begin{bmatrix} z_{avg} + \frac{z_{diff}}{2} cos2\tilde{\theta}_r & \frac{z_{diff}}{2} sin2\tilde{\theta}_r \\ \frac{z_{diff}}{2} sin2\tilde{\theta}_r & z_{avg} - \frac{z_{diff}}{2} cos2\tilde{\theta}_r \end{bmatrix} \begin{bmatrix} i_{dsh}^{\hat{r}} \\ i_{qsh}^{\hat{r}} \end{bmatrix}$$

Where z_{avg} and z_{diff} are the average and the difference of *dq* axis high frequency impedances defined in Eq 3.29 and Eq 3.30

$$z_{avg} \equiv \frac{z_{dh}^r + z_{qh}^r}{2} \qquad \textit{Eq 3.29}$$

$$z_{diff} \equiv z_{dh}^r - z_{qh}^r \qquad \textit{Eq 3.30}$$

$R(\tilde{\theta}_r)$ and $R(\tilde{\theta}_r)^{-1}$ are the rotation matrix and the inverse rotation matrix defined in Fig. 3.22 and Eq 3.31 and Eq 3.32

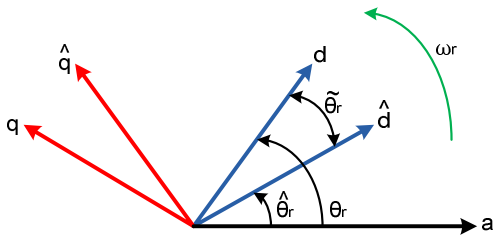

Fig. 3.22 Transformation between actual and estimated dq reference frames

$$f_{dq} = \hat{f}_{dq} \cdot e^{-j\tilde{\theta}_r} \qquad R(\tilde{\theta}_r) = \begin{bmatrix} cos\tilde{\theta}_r & sin\tilde{\theta}_r \\ -sin\tilde{\theta}_r & cos\tilde{\theta}_r \end{bmatrix} \qquad \textit{Eq 3.31}$$

$$f_{dq} = \hat{f}_{dq} \cdot e^{j\tilde{\theta}_r} \qquad R(\tilde{\theta}_r)^{-1} = \begin{bmatrix} cos\tilde{\theta}_r & -sin\tilde{\theta}_r \\ sin\tilde{\theta}_r & cos\tilde{\theta}_r \end{bmatrix} \qquad \textit{Eq 3.32}$$

Eq 3.28 can be reduced to Eq 3.33. It should be noted that the impedance matrix in the estimated rotor reference frame has cross-coupling terms, even though there are no such terms in the impedance matrix in the actual rotor reference frame.

$$\begin{bmatrix} v_{dsh}^{\hat{r}} \\ v_{qsh}^{\hat{r}} \end{bmatrix} = \begin{bmatrix} z_{dh}^{\hat{r}} & z_{ch}^{\hat{r}} \\ z_{ch}^{\hat{r}} & z_{qh}^{\hat{r}} \end{bmatrix} \begin{bmatrix} i_{dsh}^{\hat{r}} \\ i_{qsh}^{\hat{r}} \end{bmatrix} \qquad \textit{Eq 3.33}$$

Where $z_{dh}^{\hat{r}}$, $z_{qh}^{\hat{r}}$ and $z_{ch}^{\hat{r}}$ are *dq* and cross-coupling high frequency impedances in the estimated rotor reference frame. Fig. 3.23 shows the equivalent circuit of the PMSM model at high frequency in the estimated reference frame.

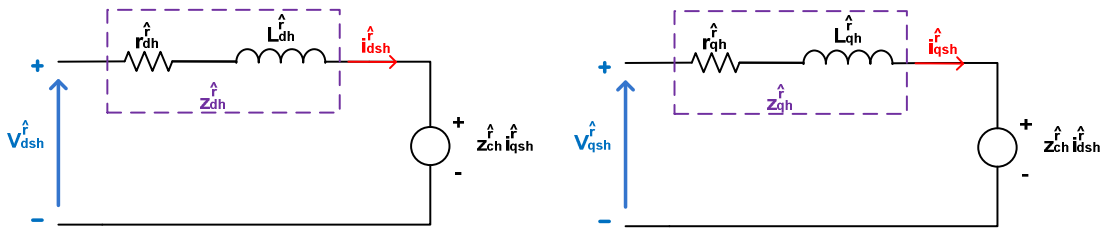

Fig. 3.23 PMSM model at high frequency in the estimated rotor reference frame

The high frequency impedances in the estimated rotor reference frame can be expressed as:

$$z_{dh}^{\hat{r}} \equiv z_{avg} + \frac{1}{2} z_{diff} cos2\tilde{\theta}_r \qquad \textit{Eq 3.34}$$

$$z_{qh}^{\hat{r}} \equiv z_{avg} - \frac{1}{2} z_{diff} cos2\tilde{\theta}_r \qquad \textit{Eq 3.35}$$

$$z_{ch}^{\hat{r}} \equiv \frac{1}{2} z_{diff} sin2\tilde{\theta}_r \qquad \textit{Eq 3.36}$$

The high frequency impedances in the estimated rotor reference frame are functions of the rotor position estimation error. The cross-coupling high frequency impedance ($z_{ch}^{\hat{r}}$) is proportional to the "sine" function of the rotor estimation error ($\tilde{\theta}_r$) if the high frequency impedance difference is not zero. This means that the actual rotor position can be estimated by forcing the cross-coupling high frequency to zero.

3.2.3.2. Sensorless control scheme

As was explained in 3.2.1 the cross-coupling high frequency impedance can be used in order to estimate the rotor position. In order to use the cross-coupling high frequency impedance the high frequency voltage and current information have to be known accurately. The selected method use the high frequency current information due the high frequency voltage information is obtained from the controller and is subject to the error produced for the nonlinear characteristics of the converter, such the dead time and zero-current-clamping phenomena. Also the use of voltage sensors increase the system cost and produce undesirable phase delays due to the filters used for filter the converter harmonics. The high frequency current information can be easily obtained and the current sensors are already part of the drive system. The high frequency currents can be expressed using the voltage equations and the relationship between the high frequency impedances.

$$\begin{bmatrix} i_{dsh}^{\hat{r}} \\ i_{qsh}^{\hat{r}} \end{bmatrix} = \frac{1}{z_{dh}^{\hat{r}} z_{qh}^{\hat{r}} - z_{ch}^{\hat{r}2}} \begin{bmatrix} z_{qh}^{\hat{r}} & -z_{ch}^{\hat{r}} \\ -z_{ch}^{\hat{r}} & z_{dh}^{\hat{r}} \end{bmatrix} \begin{bmatrix} v_{dsh}^{\hat{r}} \\ v_{qsh}^{\hat{r}} \end{bmatrix} = \frac{1}{z_{dh}^{\hat{r}} z_{qh}^{\hat{r}}} \begin{bmatrix} z_{qh}^{\hat{r}} & -z_{ch}^{\hat{r}} \\ -z_{ch}^{\hat{r}} & z_{dh}^{\hat{r}} \end{bmatrix} \begin{bmatrix} v_{dsh}^{\hat{r}} \\ v_{qsh}^{\hat{r}} \end{bmatrix} \qquad \textit{Eq 3.37}$$

Using the current and voltage relationship through the cross-coupling high frequency impedance, there are two possible injection and estimation schemes using the high frequency current. Inject the fluctuating high frequency voltage signal on the *q*-axis estimated rotor reference frame and use the high frequency current on the *d*-axis in the estimated rotor reference frame or inject the fluctuating high frequency voltage signal on the *d-axis* in the estimated rotor reference frame and use the high frequency current in the estimated rotor reference frame. The injection only in *d-axis* is better regard to torque ripples and additional losses from the high frequency currents. High frequency voltage generates high frequency current in the same axis, therefore if the high frequency voltage is injected on the estimated *q-axis*, it generates a big ripple torque.

$$\begin{bmatrix} v_{ds}^{\hat{r}} \\ v_{qs}^{\hat{r}} \end{bmatrix} = \begin{bmatrix} V_{inj} cos\omega_h t \\ 0 \end{bmatrix} \qquad \textit{Eq 3.38}$$

Where $V_{inj}$and ω_h are magnitude and frequency of the injected high frequency signal.

From the previous equation, the *q-axis* high frequency current in the estimated rotor reference frame can be expressed as:

$$i_{qsh}^{\hat{r}} = \frac{-z_{ch}^{\hat{r}}}{z_{dh}^{r} z_{qh}^{r}} V_{inj} cos\omega_h t = -\frac{1}{2} \frac{\left(r_{diff} + j\omega_h L_{diff}\right) V_{inj} sin2\hat{\theta}_r}{\left(r_{dh}^{r} + j\omega_h L_{dh}^{r}\right)\left(r_{qh}^{r} + j\omega_h L_{qh}^{r}\right)} cos\omega_h t \qquad \textit{Eq 3.39}$$

Where r_{diff} and L_{diff} are the difference between *d* and *q* axis high frequency resistances and inductances. If the high frequency impedances from the high frequency

inductances are sufficiently larger than the high frequency impedances from the high frequency resistances, the *q*-axis high frequency current in the estimated rotor reference frame can be expressed as Eq 3.40

$$i_{qsh}^{\hat{r}} \approx \frac{V_{inj}}{2}\left[\frac{r_{diff}\cos\omega_h t}{\omega_h^2 L_{dh}^r L_{qh}^r} - \frac{\omega_h L_{diff}\sin\omega_h t}{\omega_h^2 L_{dh}^r L_{qh}^r}\right] sin2\hat{\theta}_r \qquad \textit{Eq 3.40}$$

The sensorless scheme uses only the second term on the right hand side of the equation because the saturation effect due to the permanent magnet flux is more effective on the inductance than the resistance and the second term in the equation is orthogonal to the injected high frequency voltage signal. Therefore the simplification effect described in the Eq 3.25 to Eq 3.26 is not significant because the high frequency current component from the cross coupling term has negative phase from the injected high frequency voltage, provided that the high frequency inductances are dominant in the high frequency impedance.

The signal processing method used in order to obtain the rotor position estimation error from Eq 3.40 uses a bandpass filter, a multiplication and a low-pass filter as shown Fig. 3.24

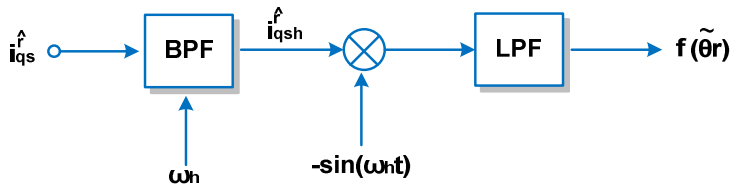

Fig. 3.24 Block diagram of signal processing

- The bandpass filter is used in order to extract the injected frequency component from the *q-axis* current in the estimated rotor reference frame.
- A multiplication is used in order to extract the orthogonal term from the injected high frequency voltage from the high frequency current.
- A low-pass filter is used to eliminate the second order harmonic term in the obtained signal.

The high frequency component of the *q-axis* current in the estimated rotor reference frame is obtained through the bandpass filter. If the signal is multiplied by the high frequency component of the *q*-axis current as shown Eq 3.41, a signal consisting in two components can be obtained. The components are the DC component and the second order harmonic component, so if a low-pass filter is used with the appropriate corner frequency, the signal containing the rotor position estimation error can be obtained.

$$-i_{qsh}^{\hat{r}} sin\omega_h t = \frac{V_{inj} sin2\tilde{\theta}_r}{2\omega_h^2 L_{dh} L_{qh}}\left[\frac{\omega_h L_{diff}}{2} - |z_{diff}| sin(2\omega_h t + \phi)\right] \qquad \textit{Eq 3.41}$$

Where $|z_{diff}| = \sqrt{r_{diff}^2 + (\omega_h L_{diff})^2}$ and $tan\phi = \frac{\omega_h L_{diff}}{r_{diff}}$

$$f(\tilde{\theta}_r) \equiv LPF[-i_{qsh}^{\hat{r}} sin\omega_h t] = \frac{V_{inj} L_{diff}}{2\omega_h L_{dh}^r L_{qh}^r} sin2\tilde{\theta}_r \qquad \textit{Eq 3.42}$$

If the rotor position error is sufficiently small the input signal can be approximated to

$$f(\tilde{\theta}_r) \approx \frac{V_{inj} L_{diff}}{2\omega_h L_{dh}^r L_{qh}^r} \tilde{\theta}_r \equiv K_{err} \tilde{\theta}_r \qquad \text{Eq 3.43}$$

In order to estimate the rotor position and the speed from the rotor position estimation error information a PI controller and an integrator are used as shown Fig. 3.25

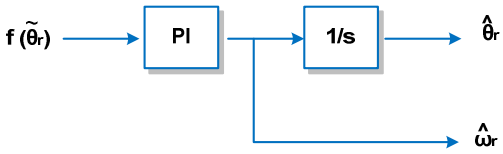

Fig. 3.25 Rotor position and speed estimation

The transfer function from the actual rotor position to the estimated one can be expressed in:

$$\frac{\hat{\theta}_r}{\theta_r} = \frac{K_{P\hat{\omega}} K_{err} s + K_{I\hat{\omega}} K_{err}}{s^2 + K_{P\hat{\omega}} K_{err} s + K_{I\hat{\omega}} K_{err}} \qquad \text{Eq 3.44}$$

Fig. 3.26 shows the block diagram of the control scheme, the currents for the current controllers are obtained through two low-pass filters after the measured currents are transformed to the estimated rotor reference frame.

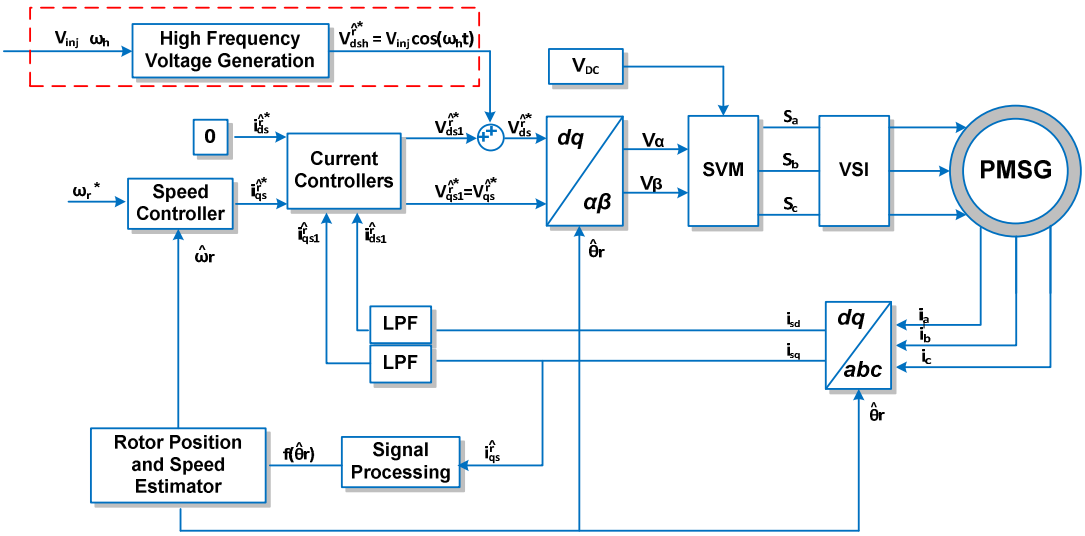

Fig. 3.26 Block diagram of sensorless drive system

3.2.4. Control design

The estimator block cannot be added directly to the FOC scheme. Firstly, the estimator components need to be tuned. The estimator is implemented using a PI controller in order to achieve the rotor position without error in steady state. In order to set the parameters of the

PI controller a close loop using the actual theta for create the error signal is implemented as shown Fig. 3.27.

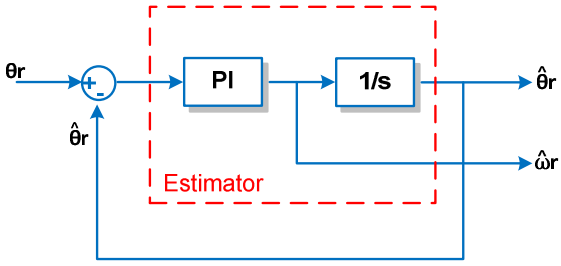

Fig. 3.27 Virtual error

This method permits to set the parameters of the controller observing that the estimated speed follows the actual speed. The estimator cannot follow perfectly the actual speed due to an error delay. This error cannot be avoided but reducing the speed controller parameters the bandwidth is reduced and the response of the controller is improved.

3.2.4.1. Selection of the High Frequency signal

An important point of the selected sensorless scheme is the selection of the high frequency signal, due the method is based on the high frequency impedance difference between *d* and *q* axis. The main idea is to select an injection frequency as high as possible, that makes the estimator faster. It is important because the position error is known after half of the injection signal period. If the frequency is high enough the performance of the current control does not get affected because the components are outside of the bandwidth of the control. There are two factors that restrict the maximum frequency: (15)

-The increment of the injected frequency decreases the measured i_q current with high frequency component, which decreases the accuracy of the system. Also very high frequency requires high voltage which is not acceptable in the practice.

- The frequency is also limited by the modulation frequency, if it is too high, the injection voltage period is realized using only a few active voltage vectors. This increase the number of harmonics in the measured i_q current with high frequency component, and the measure can be distorted due the large voltage transients.

In order to check the performance of the control under various injection conditions some voltages and frequencies have been checked. Due to the magnitude of the injected voltage affects the torque ripple, the injected voltage it is set to 20 V. The selected high frequency has been set in 500 Hz because is 10% of the switching frequency of the converter and clearly outside of the bandwidth of the current control (20). Table 3.1 shows the parameters of the controllers for selected voltage-frequency.

	Speed Controller		**Estimator controller**	
	Kpi	Kii	Kpi	Kii
20V-500Hz	0.18	5	300	5

Table 3.1 Controller parameters

3.2.4.2. Selection of the filters

In the signal processing block i_q is filtered through a bandpass filter in order to obtain the high frequency current component induced by the injected voltage. High order filter introduces a long delay, for this reason a second order filter has been implemented. In order to take only the high frequency signal a bandpass is used between 300 Hz and 800 Hz. Bode diagrams show the magnitude and phase response of the bandpass filter. The filters used in the laboratory are explained in detail in chapter 5.

Fig. 3.28 shows the Bode diagram of the bandpass filters used in the simulations, which transfer function for a f_s of 5 kHz is :

$$\frac{0.2452\, z^2 - 0.2452}{z^2 - 1.223\, z + 0.5095} \qquad \textit{Eq 3.45}$$

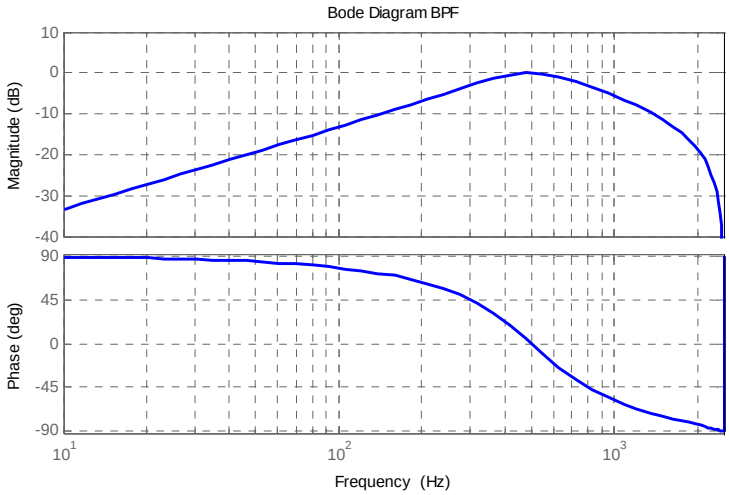

Fig. 3.28 Bandpass filter magnitud and phase response

The filtered signal is demodulated by multiply by the sine of the high frequency injected signal. A low-pass filter is used in order to remove the second harmonic and obtain the signal with the position information. The selected filter is a second order low-pass filter with a cut-off frequency of 40 Hz.

Fig. 3.29 shows the Bode diagram of the low-pass filters used in the experiment, which transfer function for a f_s of 5 kHz is:

$$\frac{0.0006099\, z^2 + 0.00122\, z + 0.0006099}{z^2 - 1.929\, z + 0.9314} \qquad \textit{Eq 3.46}$$

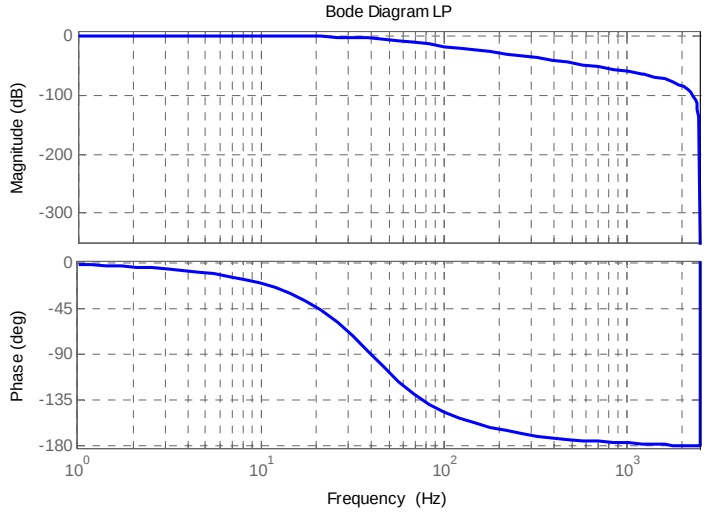

Fig. 3.29 Low-pass filter magnitud and phase response

4. Simulation results

This chapter presents the simulation results for the FOC. The chapter can be divided in two parts. In the first one, the PMSM is controlled in close loop, using the position feedback given by the encoder.

The second part presents the results in open loop control, so without position sensor. In both cases, with and without position sensor, the simulation was carried out in Matlab/Simulink. The parameters of the PMSM are given in appendix D

4.1. Close loop Field Oriented Control

In order to validate the design of the close loop FOC the model has been tested under different conditions. A test without load disturbance was studied in order to check the performance of the control under speed steps. Lastly, the study cases were with load disturbance for zero and low speed.

4.1.1. Case 1: No load and step up-down in the speed

In this study case the load is null. At the beginning, the reference speed is 500 rpm and at 1 s a step-up of 500 rpm is applied to run the machine at 1000 rpm. At 2.5 s, another step is applied until the previous reference.

In Fig. 4.1 can be observed that the speed performance of the machine tracks the reference signal quite fast.

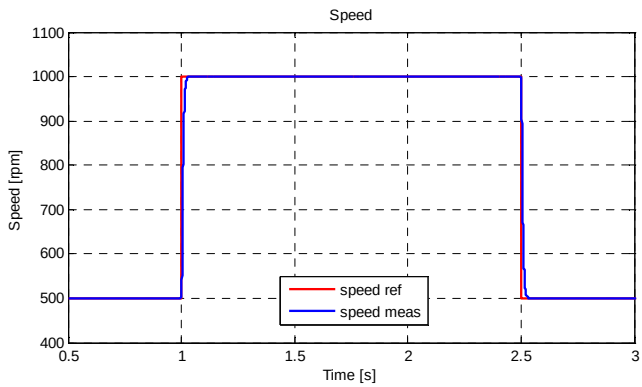

Fig. 4.1 Reference and measured speed under no load

In Fig. 4.2, the torque response is presented. The torque remains in zero due to there is no load applied. The fluctuations in the torque are produced when a step in the speed occurs, which produces a variation in the current i_{qs}.

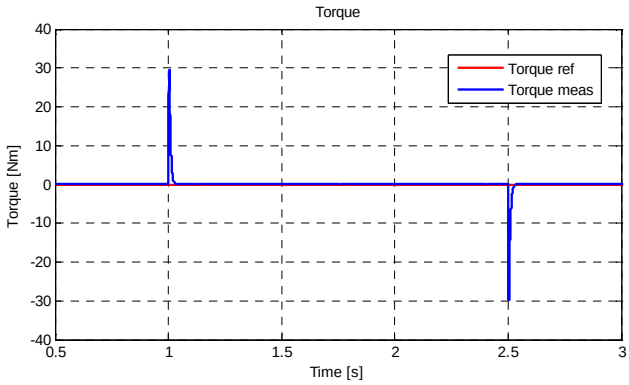

Fig. 4.2 Reference and measured torque under no load

Fig. 4.3 shows stator currents. The transients in the stator currents are produced when there is a step in the speed due to the acceleration of the drive. Before and after the transient the current value is really small due to the machine is running under no load conditions.

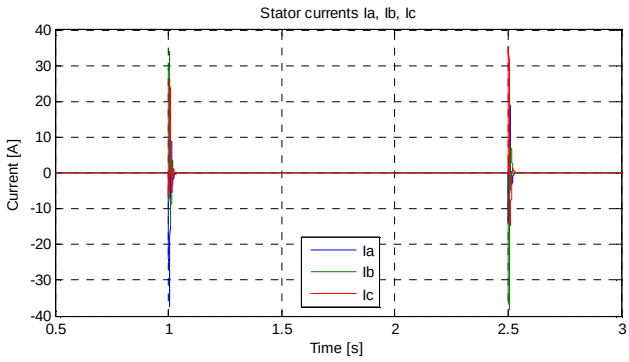

Fig. 4.3 Stator voltages under no load

In Fig. 4.4 and Fig. 4.5 i_{ds} and i_{qs} are showed. i_{ds} response remains in zero following the imposed zero reference for the FOC control strategy, with a disturbance when the step in the speed is applied.

The amplitude of the i_{qs} response is quite reduced when the motor is running at a fixed speed with no load, until a change in the reference speed is produced. This change in the reference produces a transient in the current.

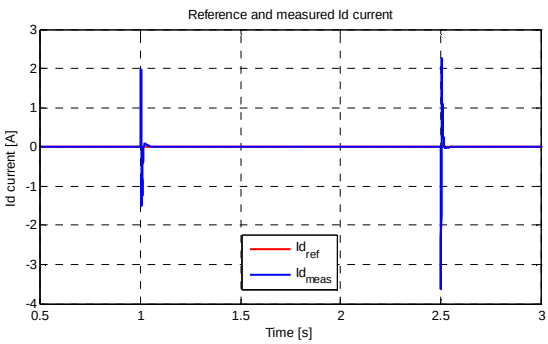

Fig. 4.4 Reference and measured i_d current

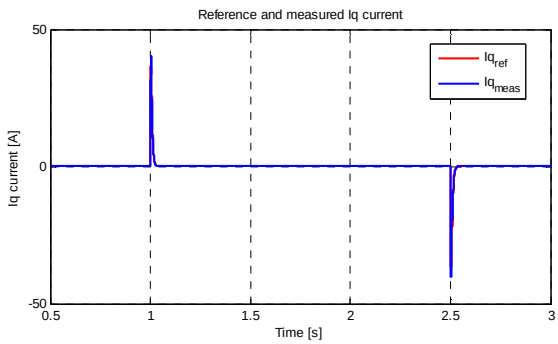

Fig. 4.5 Reference and measured i_q current

The duty cycles amplitude and frequency are bigger when high speed of the machine. In the zoom area the shape of the signals can be appreciated in detail

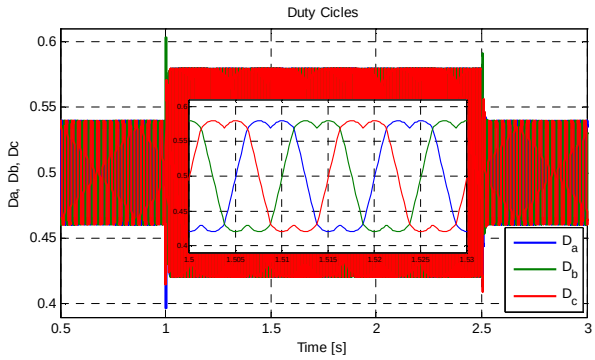

Fig. 4.6 Duty cycles under no load

4.1.2. Case 2: Zero speed with load torque steps

In this study case the speed reference is kept at 0 rpm and at 2 s a step load torque of 5 Nm is applied until 3.5 s. The idea behind is to see how the reference speed remains zero even a load is applied to the drive. Fig. 4.7 shows the performance under desired conditions, from the figure it can be observed the effect when the disturbance is applied to the drive and how the control reject the disturbance with fast dynamic response remaining the speed at the desired reference.

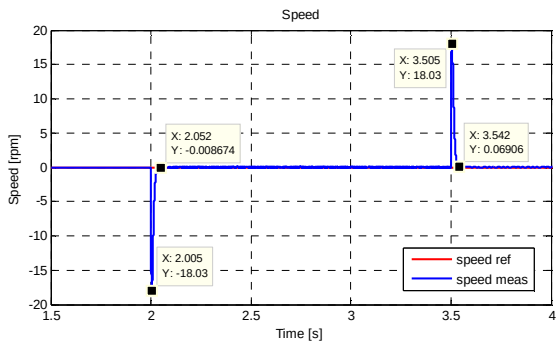

Fig. 4.7 Reference and measured speed at zero speed and load

Fig. 4.8 shows the reference and measured torque, as can be seen at 2 s a step up of 5 Nm is applied and at 3.5 s a step down remove the load.

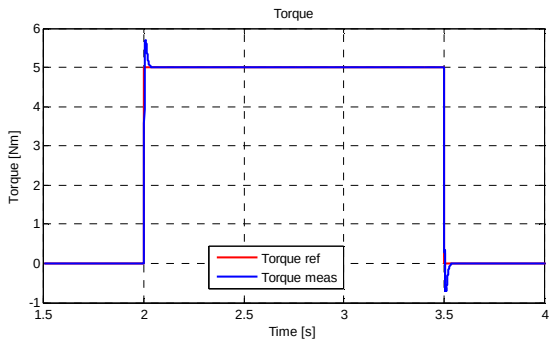

Fig. 4.8 Reference and measured torque at zero speed and load

Fig. 4.9 and Fig. 4.10 show *dq*-axis currents. As is expected both magnitudes are 0 A when no load is applied. During loading only *q*-axis current increase, *d*-axis current remains in 0 A except during the transient periods when the load is applied or removed. In Fig. 4.10 can be observed under load conditions in the shaft i_q will grow in order to generate the necessary torque and it will be reduced under lower torque demands.

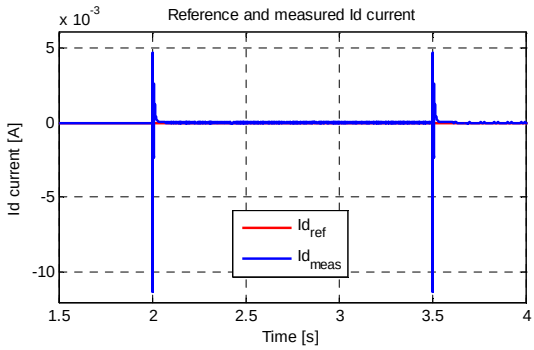

Fig. 4.9 Refernece and measured i_d current

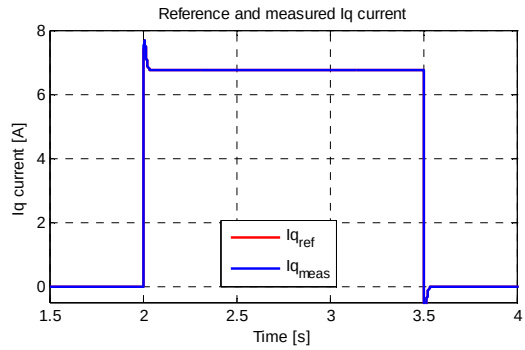

Fig. 4.10 Reference and measured i_q current

4.1.3. Case 3: Steps up in the speed and load torque steps

In this study case the reference speed is set in zero and no load until 1 s when a step up in the speed of 10 rpm is applied. At 2 s a step up in the torque of 3 Nm produce a transient in the speed. At 2.5 s a second step up in the speed is applied and set it in 20 rpm. Finally, at 3.5 s another step up in the torque of 3 Nm is realized. As can be appreciated in Fig. 4.7 the big load disturbance produced is rejected when the system is running at low speed. Fig. 4.7 also shows how the reference speed is keep constant at zero, 10 and 20 rpm during the entire test while the measured speed decreases around 11 rpm when the load torque is applied. In conclusion, the measured speed deviates from the reference speed during the transients but it maintains in its reference in steady state also during loading.

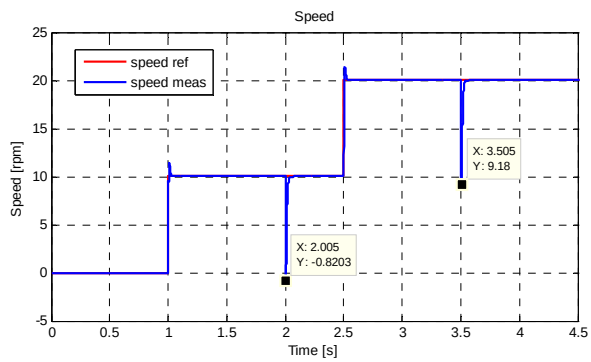

Fig. 4.11 Reference and measured speed at low speed and load

Fig. 4.12 shows the reference and the measured torque, as can be seen at 2 s a step up of 3 Nm is applied and at 3.5 s another step up set the torque in 6 Nm. In that case the disturbance is produced due the speed steps and the value of this is 2.606 Nm

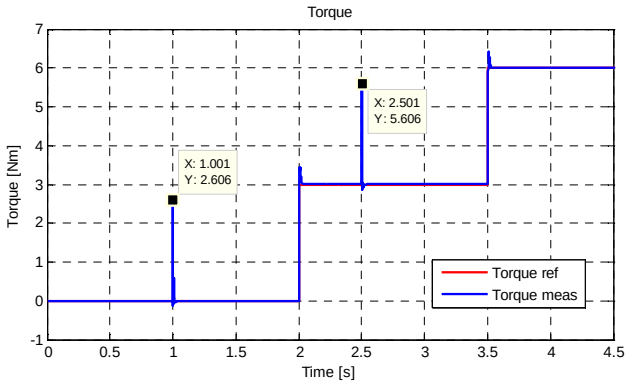

Fig. 4.12 Reference and measured torque at low speed and load

As can be observed in Fig. 4.13 i_d remains in zero for the different steps in speed and torque load. As is expected i_q is 0 A when no load is applied as can be seen in Fig. 4.14, *d*-axis current remains in 0 A except during the transient periods when the load is applied as shows Fig. 4.13. During loading only *q*-axis current increase in order to generate the necessary torque. Transients around 2 A can be observed in the i_q when a step in the speed is applied.

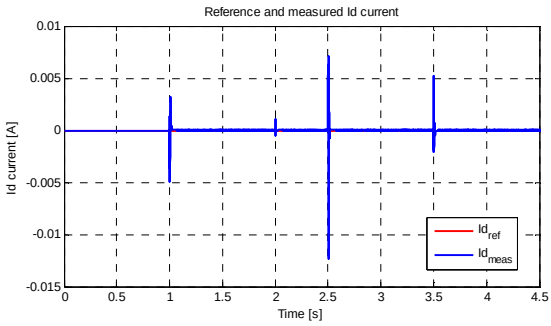

Fig. 4.13 Refernece and measured i_d current

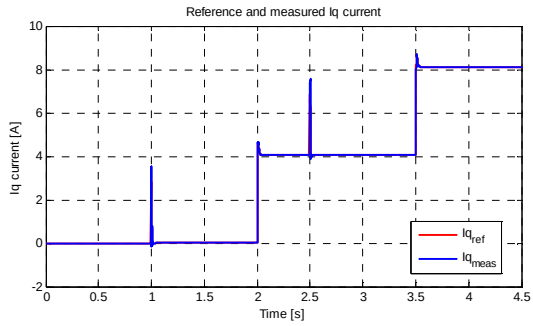

Fig. 4.14 Refernece and measured i_q current

Fig. 4.15 shows the stator currents, until the load torque is applied the currents remain null. Can be observed that with a step in the speed the frequency increase but the amplitude remains constant. The opposite happens when a step in the load torque is applied, the frequency remains constant but the amplitude of the current increase.

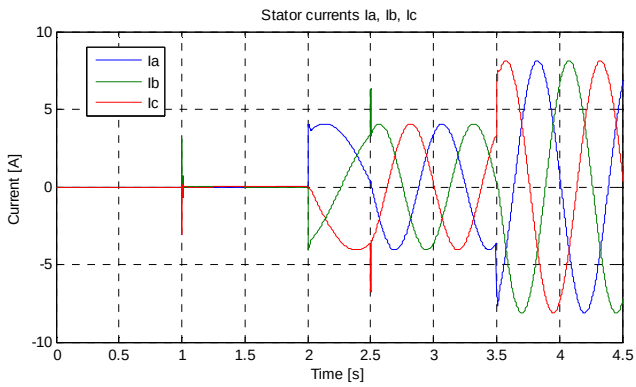

Fig. 4.15 Stator currents

4.2. Sensorless Field Oriented Control

In order to validate the design of the open loop FOC the model has been tested under different conditions. Firstly, load steps were applied when the motor is in zero speed. A test with different load disturbances and speed steps was studied. In order to check the performance of the control a change in the direction of the speed is applied. Lastly, two study cases were at constant speed with and without load disturbance were studied.

4.2.1. Case 1: Zero speed with load torque steps

In this study case the speed reference is kept at 0 rpm and at 2 s a step load torque of 5 Nm is applied until 3.5 s. The idea behind is to see how the reference speed remains zero even a load is applied to the drive. Fig. 4.16 shows the performance under desired conditions, from the figure it can be observed the effect when the disturbance is applied to the drive and how the control reject the disturbance remaining the speed at the desired reference. Comparing with Fig. 4.7 the disturbance in the speed is bigger, close to 9 times more and the dynamic response slower, around 4 times more.

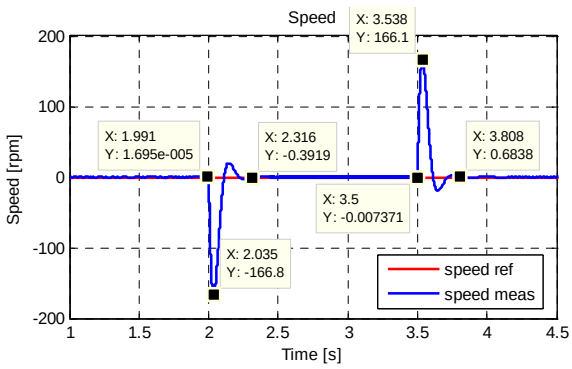

Fig. 4.16Reference and measured speed at zero speed and load

Fig. 4.17 shows the reference and measured torque, as can be seen at 2 s a step up of 5 Nm is applied and at 3.5 s a step down remove the load. Comparing with the close loop control, the overshoot is more or less two times bigger as can be seen in Fig. 4.8.

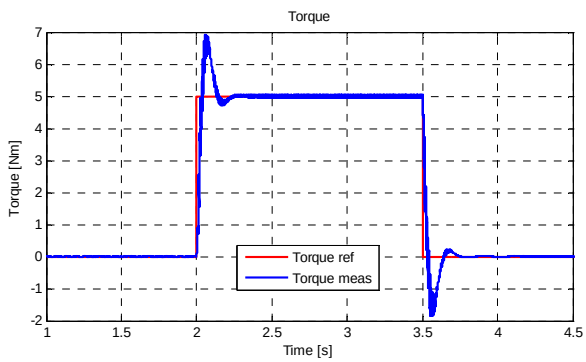

Fig. 4.17 Reference and measured torque at zero speed and load

Fig. 4.18 and Fig. 4.19 show *dq*-axis currents. As is expected both magnitudes are 0 A when no load is applied. During loading only *q*-axis current increase, *d*-axis current remains in 0 A except during the transient periods when the load is applied or removed. In Fig. 4.19 can be observed under load conditions in the shaft i_q will grow in order to generate the necessary torque and it will be reduced under lower torque demands. As was explained before the torque has bigger overshoot than in close loop control, this overshoot is reflected also in the i_q current. As in Fig. 4.9 i_d remains in zero except in the transients, the main difference with the close loop control is a ripple consequence of the signal injection.

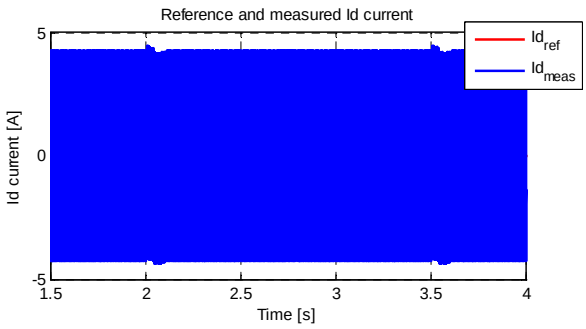

Fig. 4.18 Refernece and measured i_d current

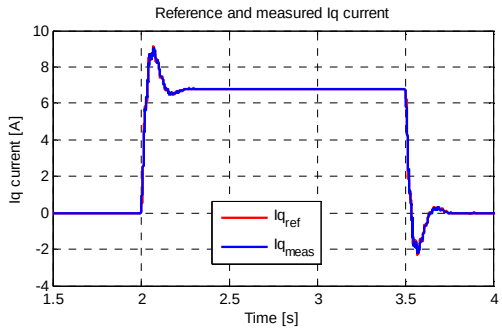

Fig. 4.19 Refernece and measured i_q current

4.2.2. Case 2: Steps up in the speed and load torque steps

In this study case the reference speed is set in zero and no load is applied until 1 s when a step up of 10 rpm is applied. At 2 s a step up in the torque of 3 Nm produce a large transient in the speed. At 2.5 s a second step up in the speed is applied and set it in 20 rpm. Finally, at 3.5 s another step up in the torque of 3 Nm is applied. As can be appreciated in Fig. 4.20 the big load disturbance produced is rejected when the system is running at low speed. Fig. 4.20 also shows how the reference speed is kept constant at zero, 10 and 20 rpm during the entire test while the measured speed decreases when the load torque is applied. In conclusion, the measured speed deviates from the reference speed during the transients but it maintains its reference in steady state also during loading. Comparing with the close loop response of Fig. 4.11 the disturbance is about 10 times bigger and the dynamic response considerably slower.

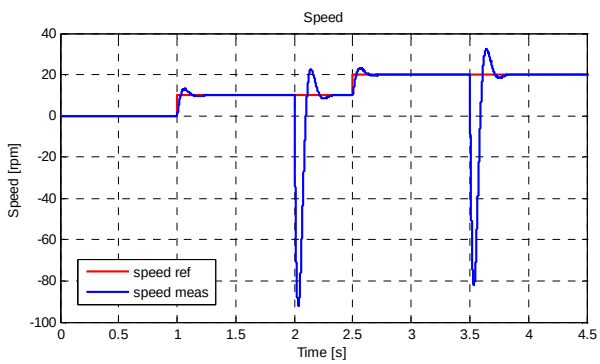

Fig. 4.20 Reference and measured speed at low speed and load

Fig. 4.21 shows the reference and the measured torque, as can be seen at 2 s a step up of 3 Nm is applied and at 3.5 s another step up set the torque in 6 Nm. The ripple is bigger than in Fig. 4.12 where it was quite reduced. The improvement of the open loop control is the reduction of the disturbance when a step in the speed is applied; it got a reduction from 2.6 Nm to 0.33 Nm. Contrary the overshoot when a load step is applied got increased 0.5 Nm and the dynamic is slower.

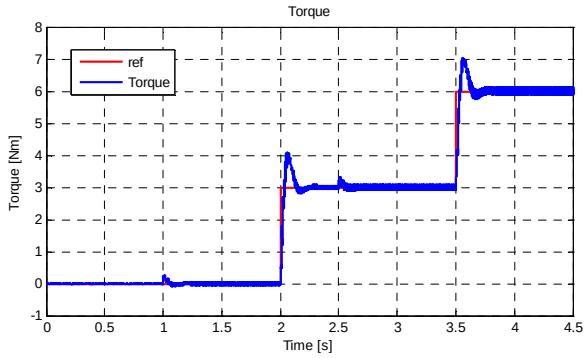

Fig. 4.21 Reference and measured torque at low speed and load

As can be observed in Fig. 4.22 i_d remains constant for the different steps in speed and torque load. Can be appreciated a considerable ripple, this is due the high frequency signal injection which is superimposed to the *d-axis* voltage. As is expected i_q is 0 A when there is no load as can be seen in Fig. 4.22, *d*-axis current remains in 0 A except during the transient periods when the load is applied as shows Fig. 4.22.Fig. 4.23. During loading only *q*-axis current increase in order to generate the necessary torque. Transients around 0.5 A can be observed in the i_q when a step in the speed is applied. In comparison with Fig. 4.12 the transients in i_q are smaller but the overshoot when a step torque is applied is bigger and slower.

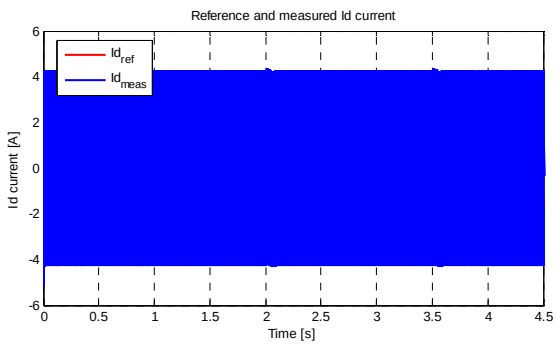

Fig. 4.22 Refernece and measured i_d current

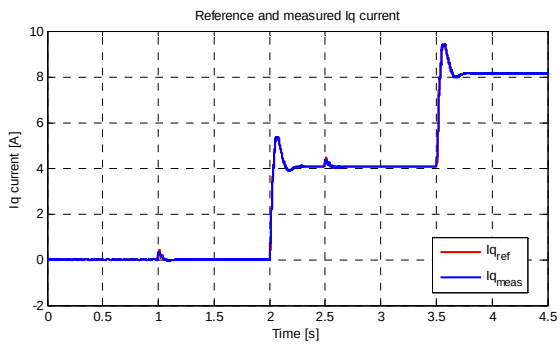

Fig. 4.23 Refernece and measured i_q current

4.2.3. Case 3: No load and reverse speed

In this case, the machine is working with no load. At the beginning, the reference of the speed is 10 rpm and at 2 s, a step down in the reference is applied to run the machine with a reference of -10 rpm. In Fig. 4.24 can be observed that the speed performance of the machine tracks the reference signal. With this test it can be checked that the control allows a change in the direction of the speed, but is important to mention that a bit overshoot is present and the dynamics need 0.25 s to work in steady state again.

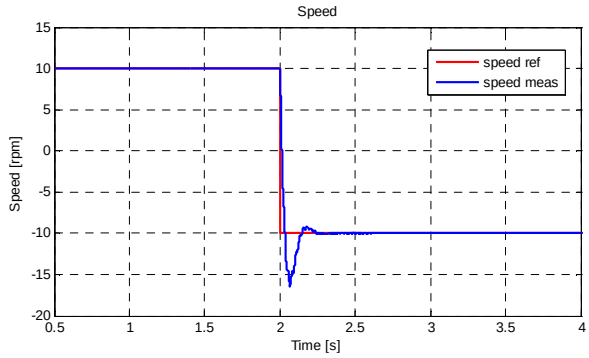

Fig. 4.24 Reference and measured speed with change in the direction of the speed

The torque remains in zero in steady state due to there is no load applied. The fluctuations in the torque are produced when a step in the speed occurs, which produces a variation in the current i_{qs} as the previous case.

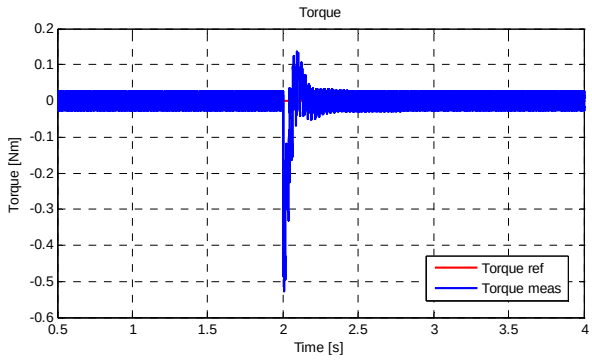

Fig. 4.25Reference and measured torque with change in the direction of the speed

Fig. *4.26* shows i_d current, as explained before it remains in zero for a change in the speed. A big ripple is present in this signal due the high frequency signal injection. i_q is zero due no load is applied as can be observed in Fig. 4.27. A disturbance is present when the step in the speed is settled as is expected after analyse the behaviour of the torque in Fig. 4.25.

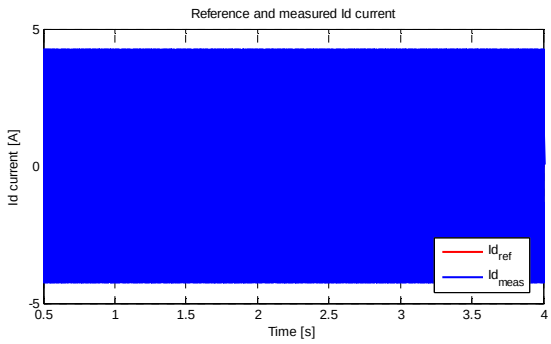

Fig. 4.26 Refernece and measured i_d current

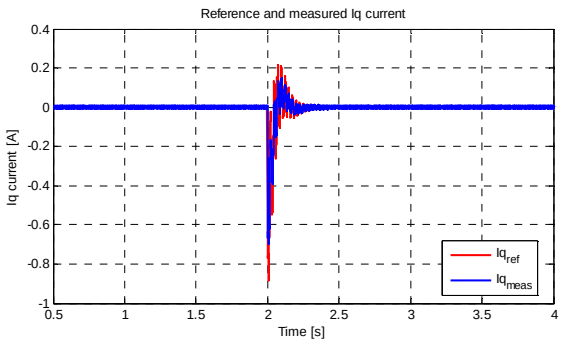

Fig. 4.27 Refernece and measured i_q current

4.2.4. Case 4: Constant speed and no load

In this case constant speed of 10 rpm is settled under no load disturbance. As can be seen in Fig. 4.28 the measured speed follows the

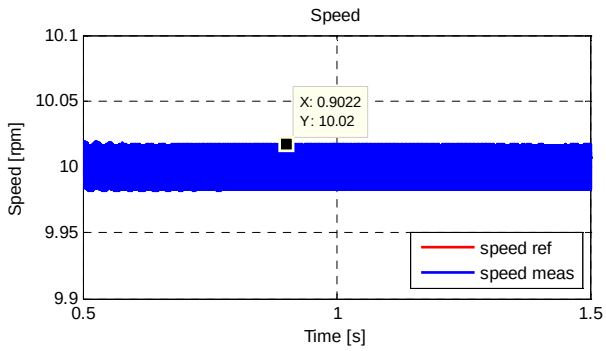

Fig. 4.28Reference and measured speed for a constant speed and no load

Fig. 4.29 shows the load torque, as is expected it is null because no load is applied. As in the speed the ripple of the signal has a frequency of 500 Hz.

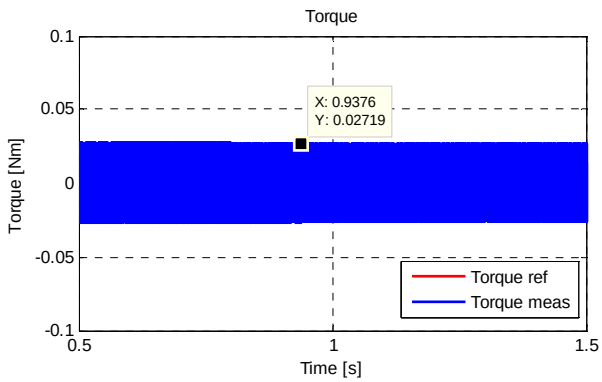

Fig. 4.29 Reference and measured torque for a constant speed and no load

In Fig. 4.30 and Fig. 4.31 i_{ds} and i_{qs} are showed. i_{ds} response remains in zero following the imposed zero reference for the FOC control strategy. It can be observed a ripple around 4A due to the high frequency signal injection. The amplitude of the i_{qs} response is zero when the motor is running at a fixed speed with no load

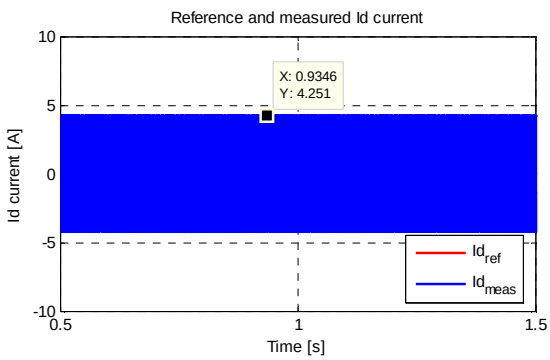

Fig. 4.30 Refernece and measured i_d current

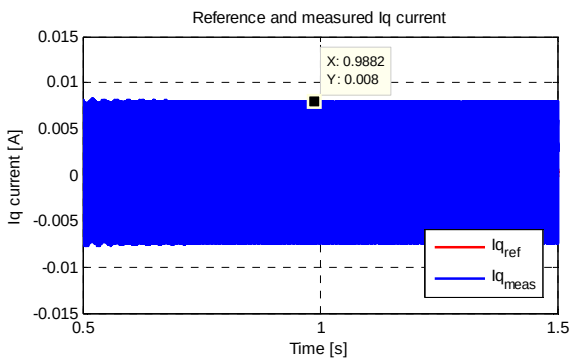

Fig. 4.31 Refernece and measured i_q current

4.2.5. Case 5: Constant speed and load

This study case is quite similar to case 4, but in this case a constant load of 1 Nm is applied. As can be seen in

Fig. 4.32 the measured speed follows the reference of 10 rpm with a small ripple of 0.2%.

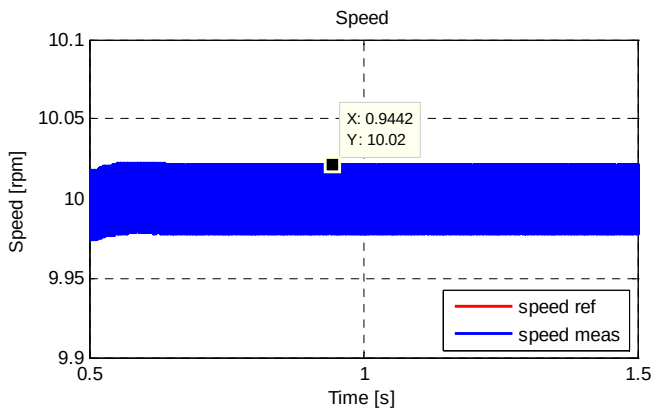

Fig. 4.32 Reference and measured speed for a constant speed and load

Fig. 4.33 presents the torque response. It can be seen that it follows the reference with a small ripple.

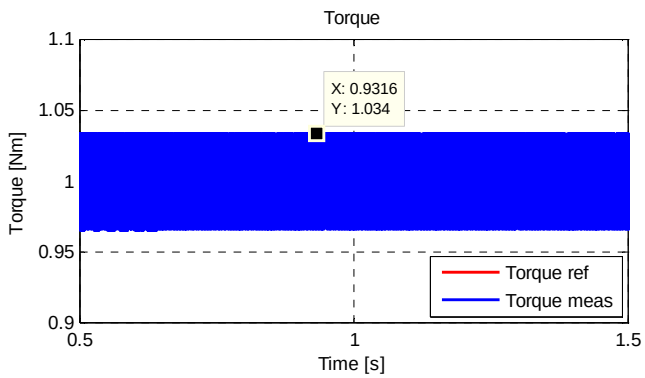

Fig. 4.33 Reference and measured torque for a constant speed and load

In Fig. 4.34 and Fig. 4.35 i_{ds} and i_{qs} are showed. i_{ds} response remains in zero following the imposed zero reference for the FOC control strategy. It can be observed a ripple around 4 A due to the high frequency signal injection.

The amplitude of the i_{qs} response is 1.35 A when the motor is running at a fixed speed with 1 Nm of load. This amount of current in *q-axis* is required in order to generate the demanded torque.

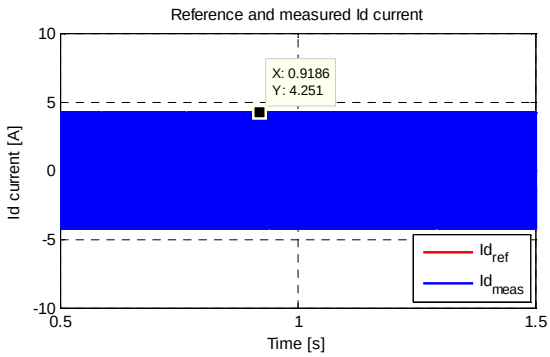

Fig. 4.34 Refernece and measured i_d current

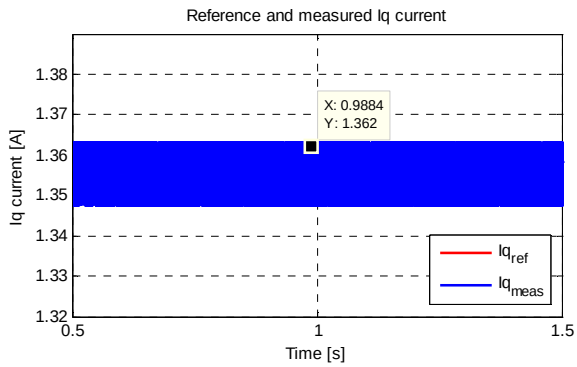

Fig. 4.35 Refernece and measured i_q current

5. Experimental work

This chapter summarizes the laboratory work and results, the experimental parts of the project which were carried out in the dSpace laboratory. The chapter begins with a short explanation about the experimental set up. Also the rotor alignment procedure is presented. Experimental tests for different study cases are presented.

Introduction

The laboratory experiments are done with a 5 kW converter which feeds a PMSM. The parameters of the machine can be found in appendix E. Fig. 5.1 shows the general structure of the experimental set-up.

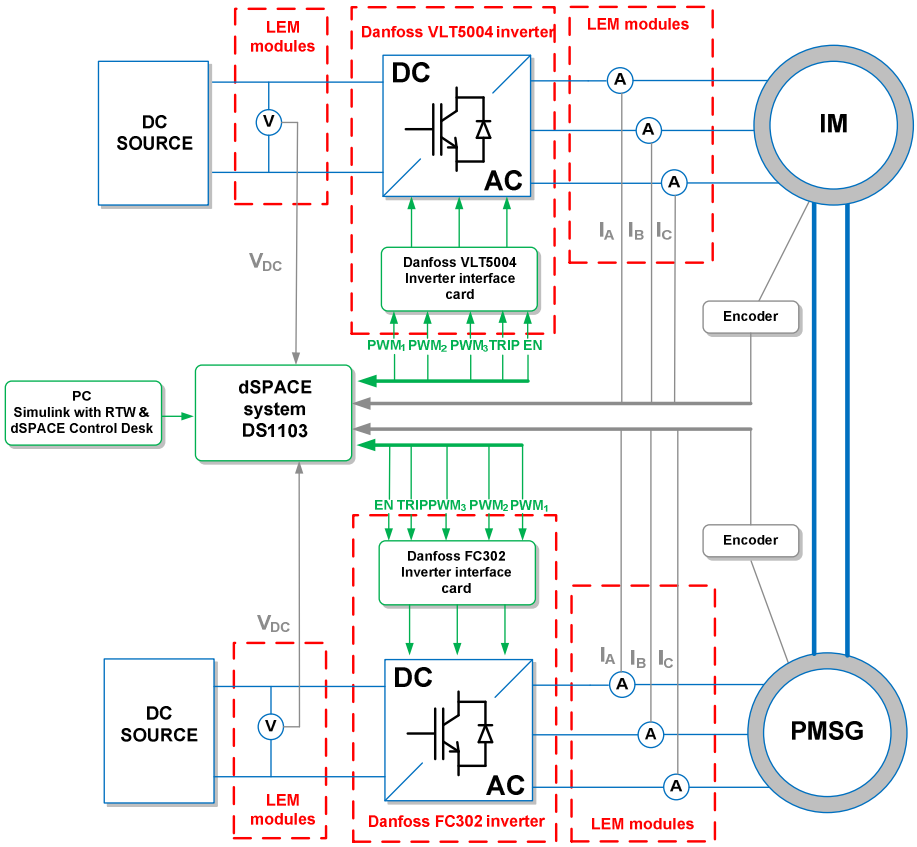

Fig. 5.1Experimental Set-up

The VLT-FC302 converter is controlled using five signals from the dSpace IPC card. Three signals are for the duty cycles and two more for the enable and the trip reset. dSpace 1103 platform is used for implementing the control strategy. The input signals which feed the dSpace system are DC voltage from the DC-link, the output currents from the converter and the output signal from the encoder from the PMSM.

In section C of the appendix, more details of the set-up components can be found.

Rotor alignment

Before the motor starts, the initial position must be determined. The method used is executed once, during the first motor starting. The motor is powered with a static voltage pattern and the rotor aligns to a predefined position. Before the constant current vector is applied to the stator, the rotor position is not known, but after the stabilization period, the rotor flux must be aligned with the stator flux, in order to achieve the maximum torque, as can be seen in Fig. 5.2 . (21)

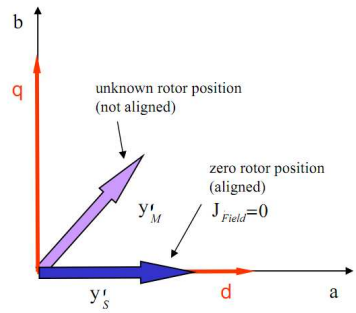

Fig. 5.2Rotor alignment

The DC injection works when the stationary magnetic field in the stator is created. The rotor will align itself with an unpredictable direction, which will be the closer one to be aligned with the magnetic field of the stator, creating a strong braking force. (22) (23)

5.1. Field Oriented Control

FOC strategy, as it was mentioned in section 3.1.1, consists in three control loop, two inner ones for controlling the currents and the outer one for controlling the speed of the drive. The inner loops have to be faster than the outer, so a well tuned current loop is demanded. As a first approach the rotor of the machine is blocked in order to tune the PI with the properly parameters until get the desired performance. The Fig. 5.3 shows the response of the current controller for i_q for references from 1 A to 4 A. Also the response of the i_d is presented which remains zero as was expected.

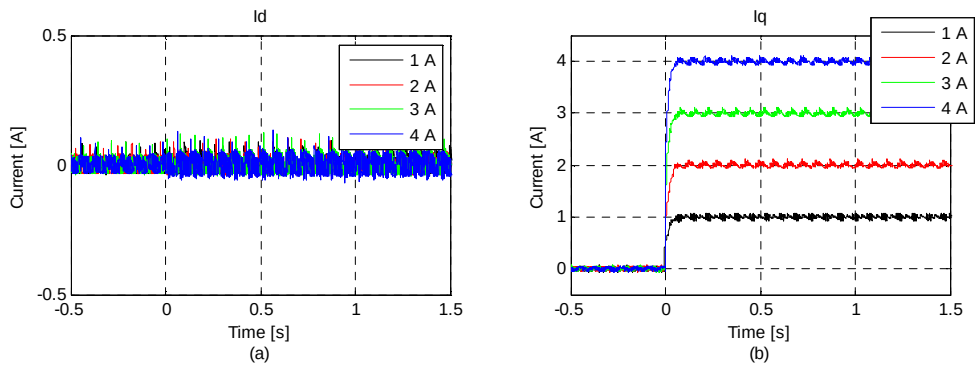

Fig. 5.3 Response of i_d and i_q current

For determining the bandwidth of the controllers it may be assumed that the frequency where 45 deg phase delay occurs is considered as the bandwidth of the regulator (24). The Fig. 5.4 shows the current regulation performance at a standstill. *d-axis* current in the rotor reference frame was regulated with a sine wave reference. The magnitude of the current reference was 1 A. In Fig. 5.4 a) and b), the offset of the currents reference were 0 A and 1 A, respectively. In Fig. 5.4 a) the current was slightly distorted in the zero cross due to the clamping effect. From Fig. 5.4 b) it can be determined that the bandwidth of the current controller is 275 Hz. The bandwidth of i_q is similar due to $L_d \approx L_q$.

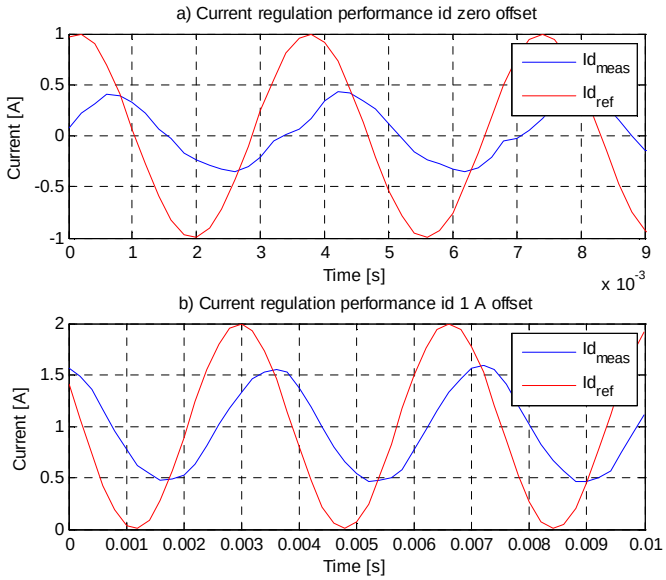

Fig. 5.4 Current regulation performance

The Low-pass filters in the feedback of the measured currents were neglected due to the bandwidth of the current loop is 275 Hz and the injection signal has a frequency of 500 Hz, so the current control is able attenuate the injected signal in the properly way without using a filter in the feedback path.

Fig. 5.5 shows the sine response of the speed controller to show the bandwidth of the speed regulator clearly from which the bandwidth of the outer controller is around 7 Hz. It may be seen that the inner controller is much faster than the outer one.

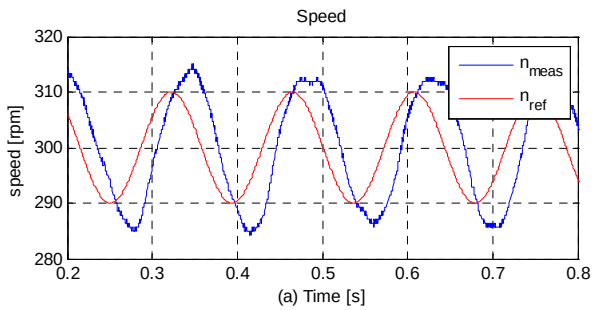

Fig. 5.5 Sine response of the speed controller

5.1.1. Case 1: No load and step up-down in the speed

In the first case the field oriented controller performance was tested under no load conditions. A step, up and down, of 500 rpm was applied in the command speed when the machine was spinning at 500 rpm. In Fig. 5.6, speed, torque and three phase current response are showed under the test conditions explained above.

From the graphs can be observed a small overshoot when a change in the speed reference is demanded, this sudden change will produce a peak in the torque due to the acceleration of the drive which generate a transient in the three phase current. The overshoot for both steps in the measured speed is about 13%.

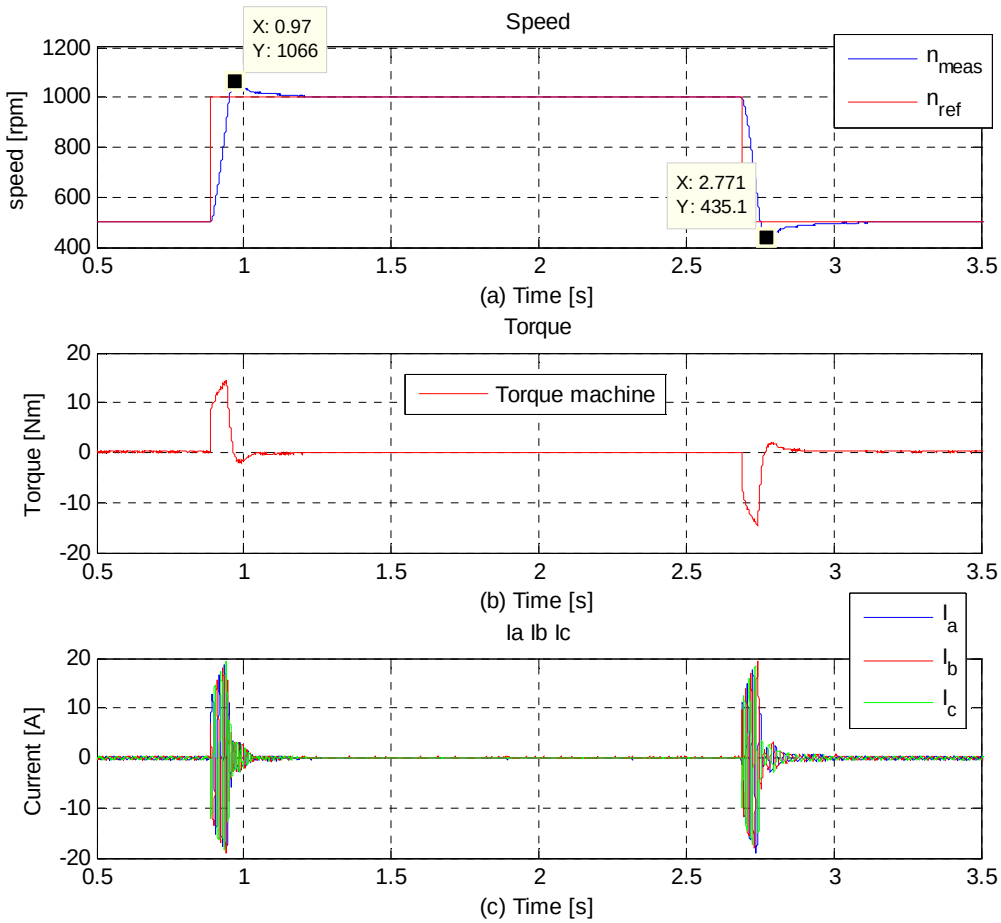

Fig. 5.6 Speed, torque and current under no load and step up-down in the speed

Fig. 5.7, presents the i_d and i_q, performance under the desired test conditions. The effect of the acceleration is reflected in the current, it may be observed that the value of i_d remains zero.

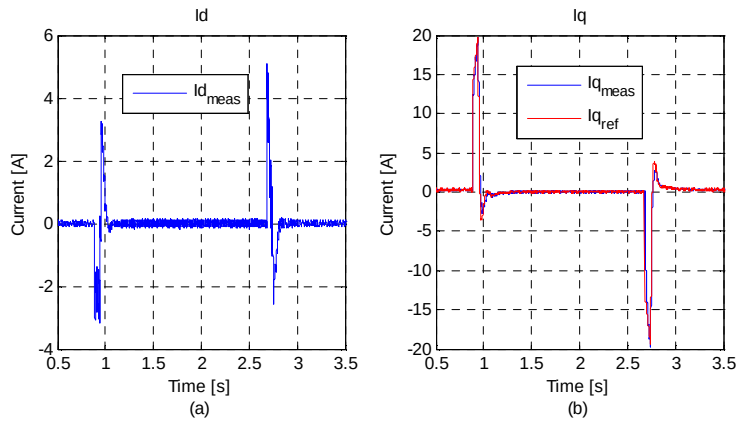

Fig. 5.7 i_d and i_q current under no load and step up-down in the speed

In Fig. 5.8, the space vector modulation is presented. When faster speed is required in the drive, the frequency and amplitude of the modulation are incremented. In the zoom-in areas these effects can be noted clearly.

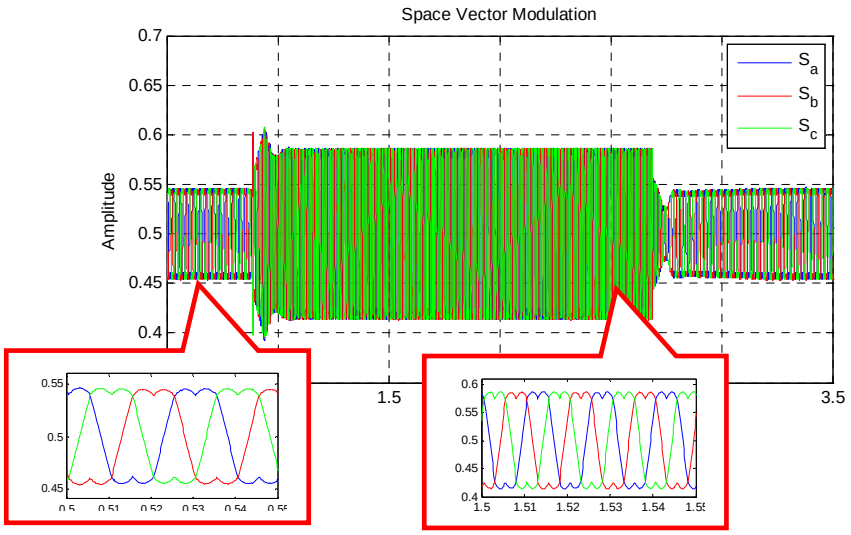

Fig. 5.8 Space vector modulation

5.1.2. Case 2: zero speed with load torque steps

In these test a load of 5 Nm was applied to the drive while any speed was demanded. Fig. 5.9 shows how the dynamic of the control reject the effect of the applied torque keeping the speed at zero with good performance.

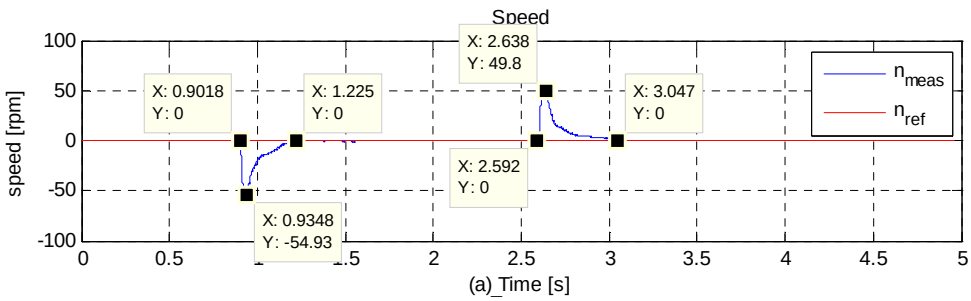

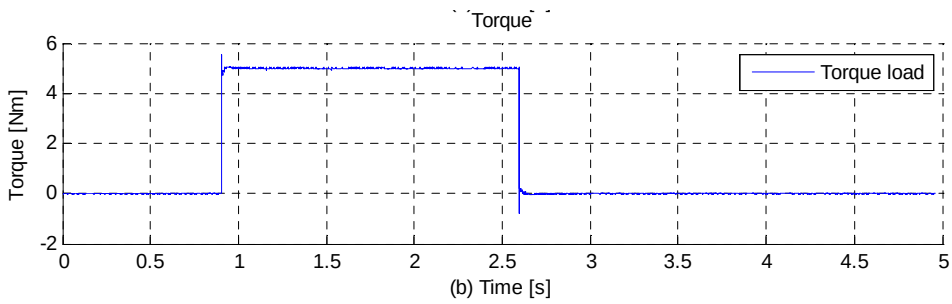

Fig. 5.9 Speed and torque response for zero speed with load torque steps

Fig. 5.10, presents the i_d and i_q, performance under the desired test conditions. The effect of the applied load may be observed in i_q which is the required necessary current for controlling the torque produced by the machine, the value of i_d remains zero.

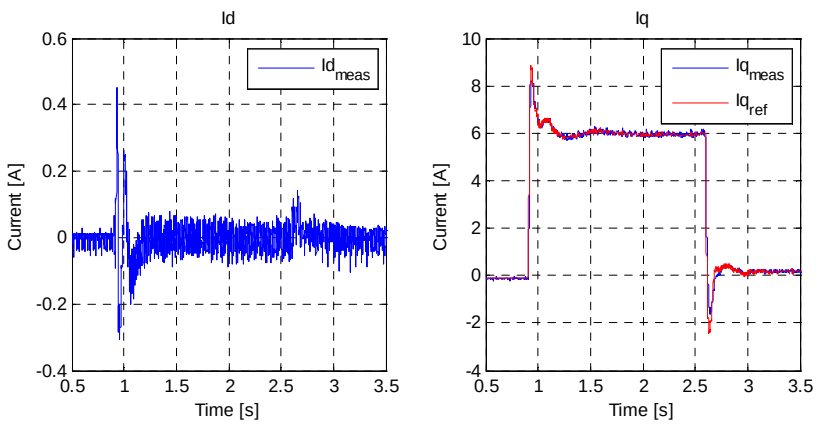

Fig. 5.10 i_d and i_q, response for zero speed with load torque steps

5.1.3. Case 3: Steps up in the speed and load torque steps

In this test is presented the performance of the machine under low speed under load and no load conditions. The machine spun at 10 rpm and 20 rpm, while the values of the demanded load were 0, 3 and 6 Nm. In Fig. 5.11, speed, torque and three phase current response can be checked under the test conditions mentioned above.

From the graphs can be observed how the speed follows the reference and how the control overcomes the applied load. The effect of the load is reflected as a large perturbation in the speed. From the graph of the torque it may be noticed how the electromagnetic torque produced by the machine follows the load torque generated by the load.

The effect of different applied loads and speeds to the drive is reflected in the three phase current by the fact under load conditions the required current for producing the electromagnetic torque is bigger.

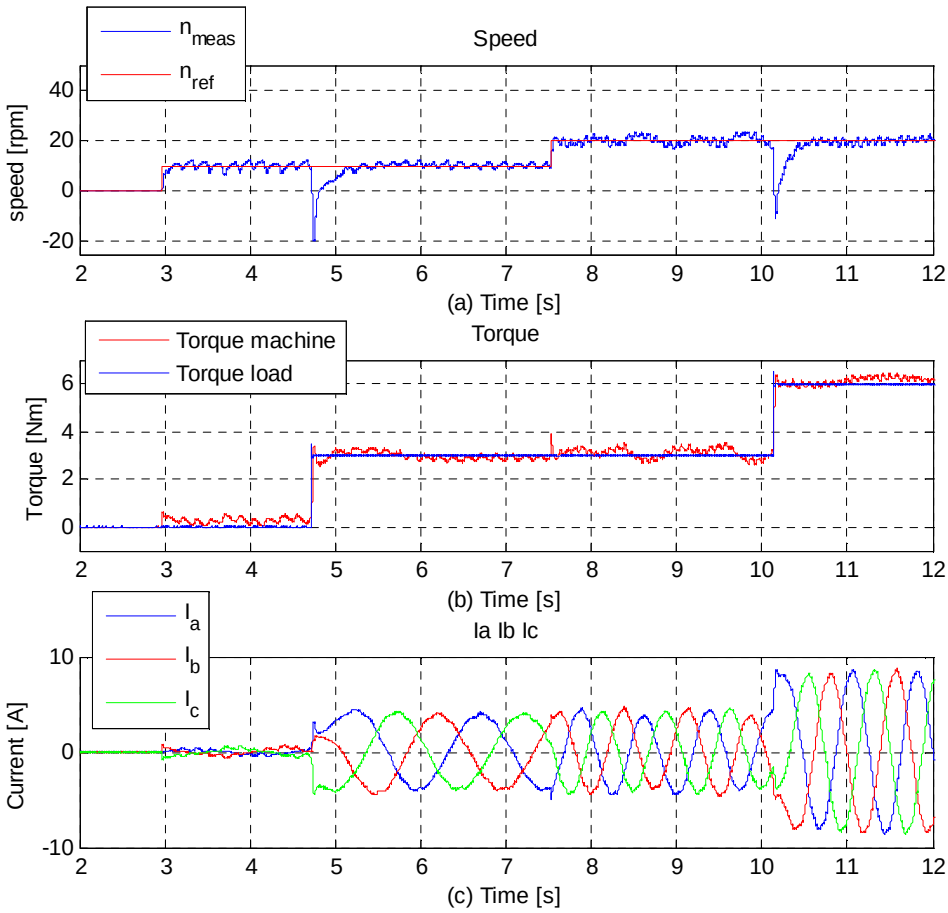

Fig. 5.11 Speed, torque and current response for steps up in the speed and load torque steps

Fig. 5.12, presents the i_d and i_q, performance under the desired test conditions. The effect of the applied load may be observed in i_q which is the required necessary current for controlling the torque produced by the machine, the value of i_d remains zero.

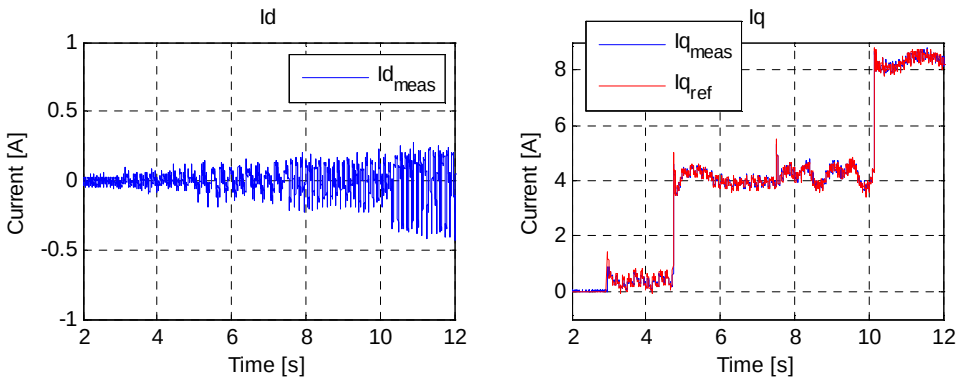

Fig. 5.12 i_d and i_q current for steps up in the speed and load torque steps

5.2. Sensorless Control

Signal processing

The signal processing of the current is a relevant issue in sensorless strategies due to it has to be accurate in order to extract the rotor information precisely.

The FFT analysis of the signal was realize online under close loop operation.

In the setup used for carrying on the experiments was observed the presence of extra harmonics in the neighbourhood of the frequency of the injected signal. The amplitude of this harmonics was pretty high as it may be observed in Fig. 5.13 where a FFT analysis of the signal is presented, in Fig. 5.13 b) a detail of the surrounding area of the injected signal is presented.

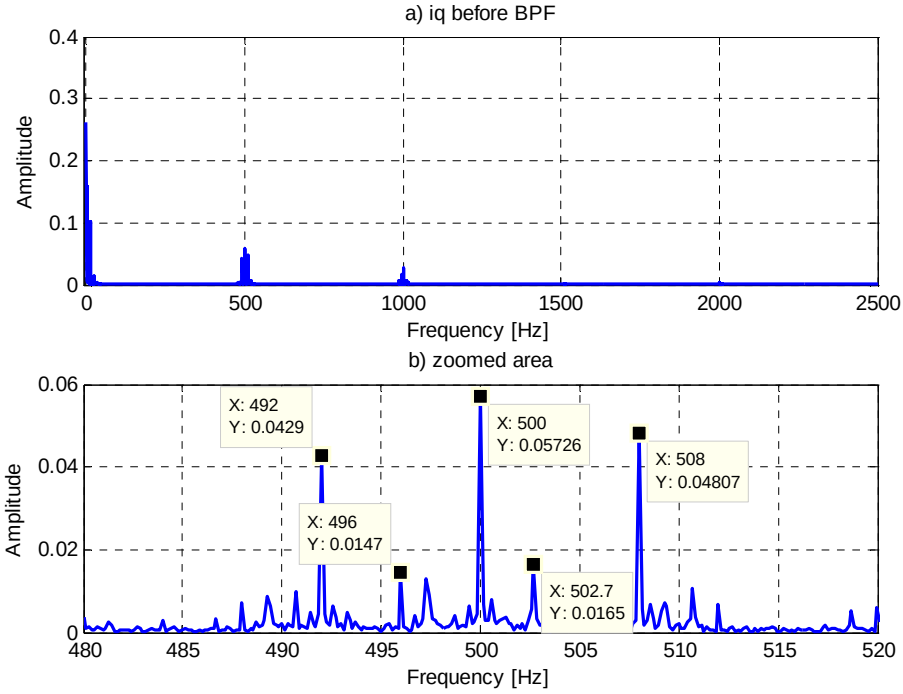

Fig. 5.13 FFT analysis of the dignal before the BPF at 20rpm and no load

It was observed that the frequency and amplitude of these harmonics were depending on the speed and torque applied to the machine. In Fig. 5.13 the machine spun at 20 rpm with no load applied in the shaft.

In Fig. 5.14 the speed was also 20 rpm but 2 Nm applied as a load. In Fig. 5.15 the machine spun at 10 rpm and no load.

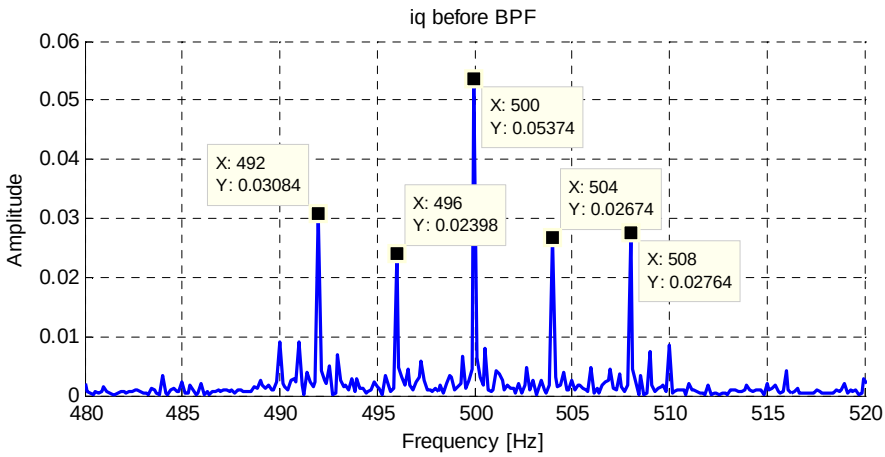

Fig. 5.14 FFT analysis of the signal before BPF at 20 rpm and 2 Nm

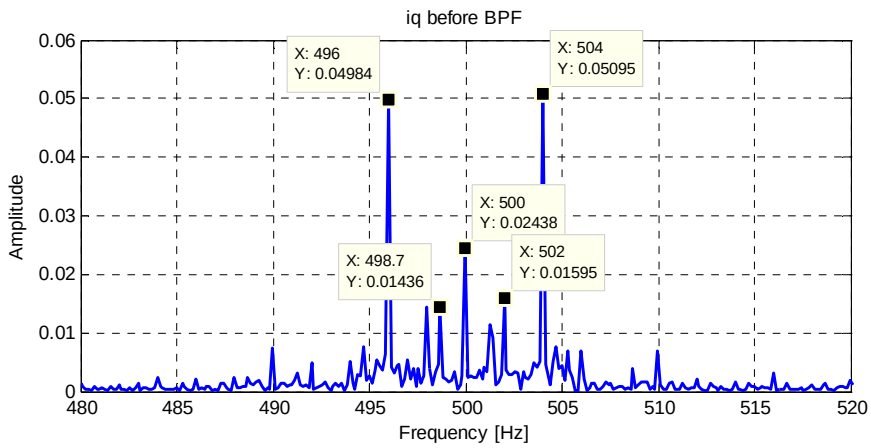

Fig. 5.15 Analysis of the signal before BPF at 10 rpm and no load

From both figures can be noticed that the amplitude and frequency of the harmonics close to the injected frequency has changed.

Due to this performance the bandpass filter used in the algorithm has to be really narrow and high order in order to let pass just the injected signal and attenuate the effect of these harmonics. In the experiment two Butterworth bandpass filter of order 4 were implemented which cut off frequencies were between 499 Hz and 501 Hz. Fig. 5.16 shows bode diagram for magnitude and phase of one of this filters.

Fig. 5.16 shows the bode diagram of one the bandpass filters used in the experiment, which transfer function for a f_s of 5 KHz is

$$\frac{0.001255\, z^2 - 0.001255}{z^2 - 1.616\, z + 0.9975} \qquad \textit{Eq 5.1}$$

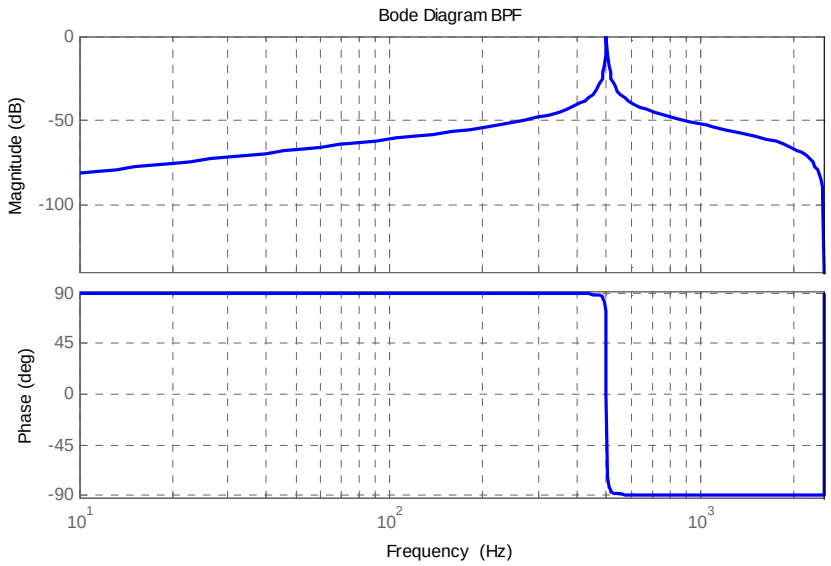

Fig. 5.16 Bode diagram of one the bandpass filters

Input and output of the bandpass filter is presented in Fig. 5.17

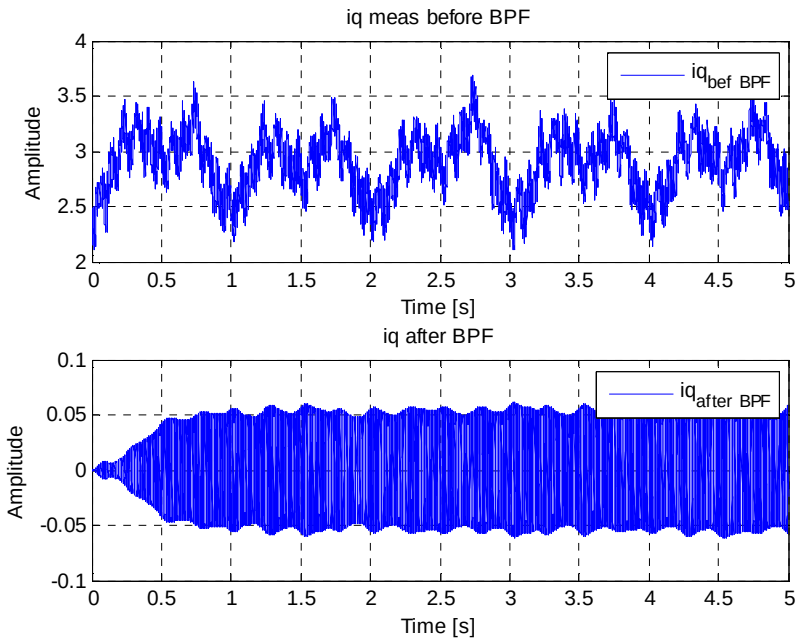

Fig. 5.17 Input and output of the bandpass filter

Fig. 5.18 shows the FFT analysis of the selected output bandpass filters where may be noticed the attenuation of the surrounding harmonics

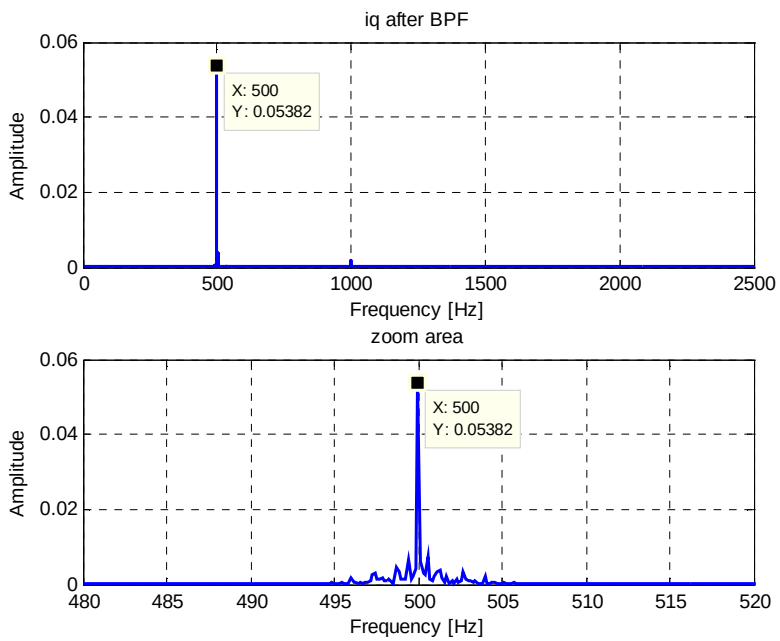

Fig. 5.18 FFT analysis of the selected output bandpass filters

From the reference (3) the output of the bandpass filter is multiplied by $-\sin(\omega_h t)$ in order to extract the orthogonal term to the injected high-frequency voltage from the high frequency current. In the experiment was observed that there was a variable diphase between the output of the bandpass filter and the $-\sin(\omega_h t)$. For getting the synchronization, the diphase between the output of the bandpass filter and ideal $-\sin(\omega_h t)$ was calculated knowing when both signals cross zero, once the diphase was calculated it was added to the signal $-\sin(\omega_h t + \varphi)$, which was used by the multiplication. Fig. 5.19 shows the structure of the Simulink block diagram for achieving the synchronization.

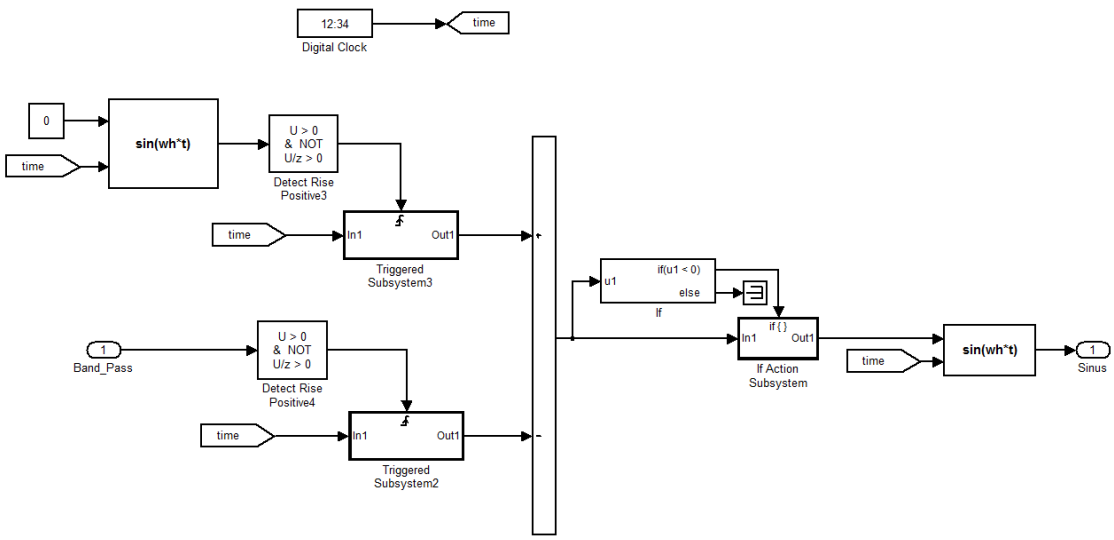

Fig. 5.19 Simulink block diagram for achieving the synchronization

In Fig. 5.20 presents the result of the synchronization between the output of the bandpass filter and $-\sin(\omega_h t)$, it can be noticed both signals are in phase.

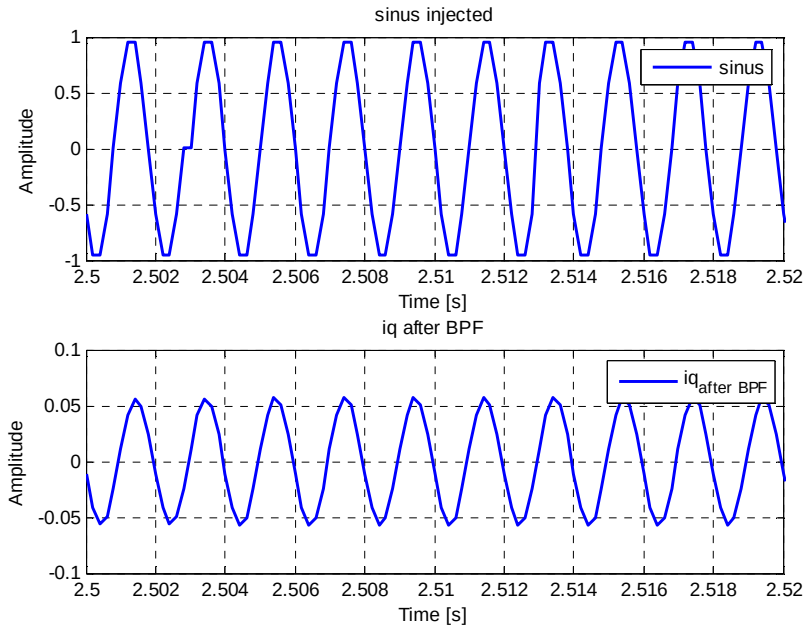

Fig. 5.20 Synchronization between the output of the bandpass filter and $-sin(\omega_h t)$,

According with (3) when both signals are in phase the resultant signal has to components which are the dc component and a second order harmonic component. Through the FFT analysis in Fig. 5.21 can be observed.

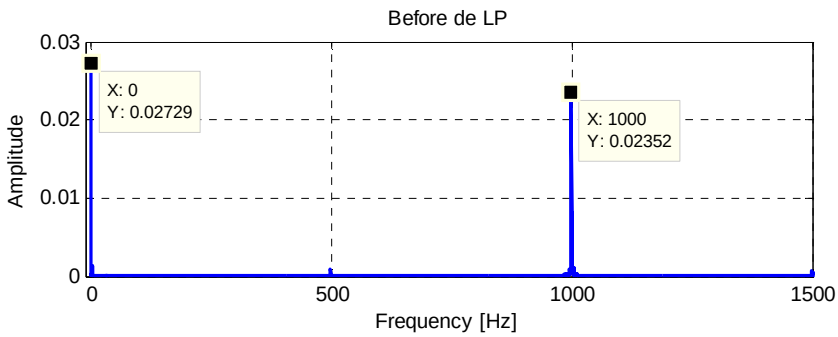

Fig. 5.21 FFT analysis before Low-pass filter

For getting rid of the second order harmonic term a Butterworth low-pass filter of first order was used with a cut-off frequency settled at 100 Hz. Fig. 5.22 shows the bode diagram and Eq 5.2 the transfer function of the filter for a switching frequency of 5 kHz is presented.

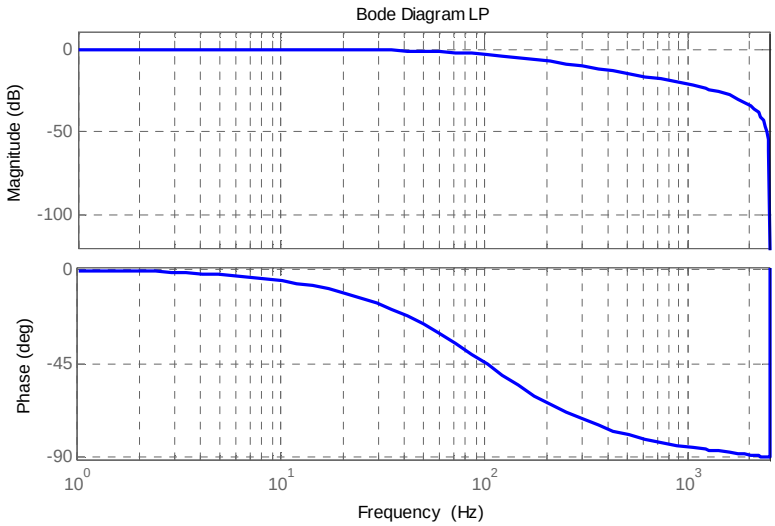

Fig. 5.22 Bode diagram of the Low-pass filter

$$\frac{0.05919\, z^2 + 0.05919\, z}{z^2 - 0.8816\, z} \qquad \textit{Eq 5.2}$$

The FFT analysis of the output signal in Fig. 5.23 confirms just the DC component is obtained at the output and the rest of the frequencies are neglected.

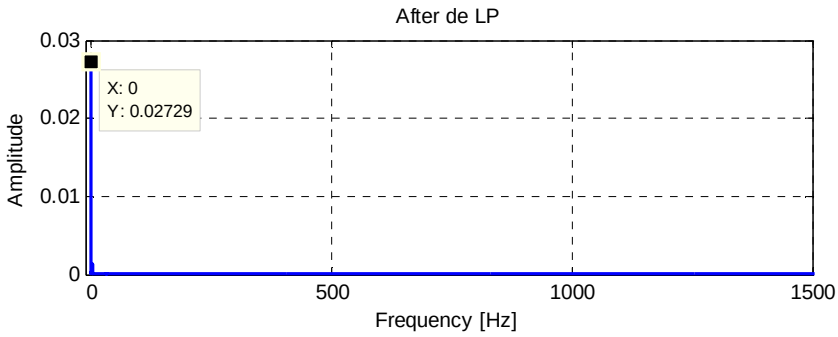

Fig. 5.23 FFT analysis after Low-pass filter

Fig. 5.24 the performance of the filter where the Fig. 5.24 a) shows the input of the low-pass filter signal which contains the DC component and the second harmonic. Fig. 5.24 b) shows the output of the low-pass filter which contains just the DC component of the signal.

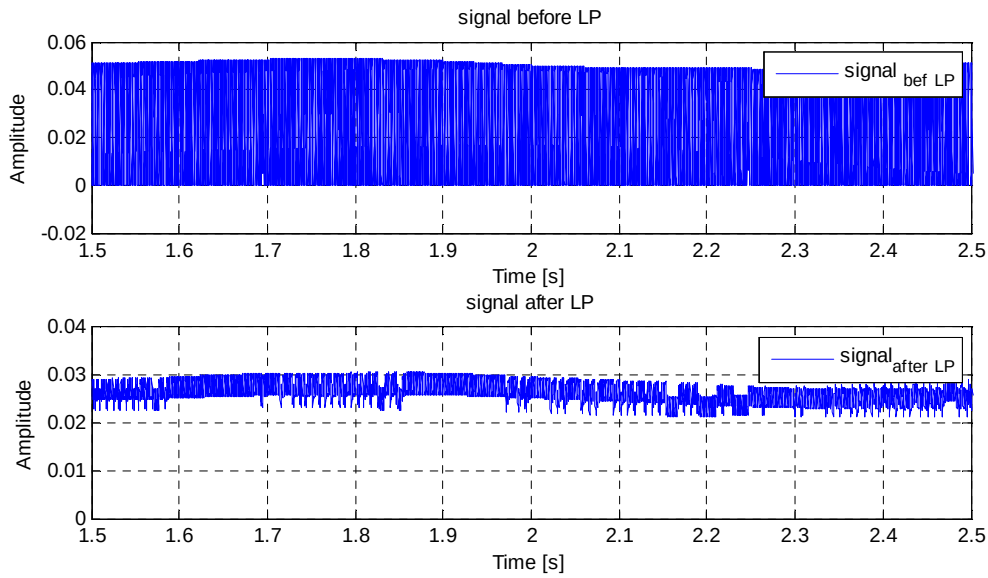

Fig. 5.24 i_q before and after the Low-pass filter

Look up table

Due to the relation between the speed and the rotor position estimation error information (f(θ)) is not lineal and adaptive controller made with a look up table is used instead of use a conventional PI controller. The different values used to build the look up table are obtained experimentally. The inputs of the table are the speed and rotor position estimation error information. The output of the look up table must be multiplied by the rotor position estimation error in order to obtain the desired angular speed.

speed / f(θ)	-20	-10	0	10	20
-0.06	139.59	69.7972	0	0	0
-0.05	167.52	83.76	0	0	0
-0.04	209.4	104.7	0	0	0
-0.03	279.1972	139.59	0	0	0
-0.02	418.8	209.4	0	0	0
-0.01	837.6	418.8	0	0	0
0	558.4642	279.2321	0	349.0401	620.5158
0.01	0	0	0	418.8	837.6
0.02	0	0	0	209.4	418.8
0.03	0	0	0	139.59	279.1972
0.04	0	0	0	104.7	209.4
0.05	0	0	0	83.76	167.52
0.06	0	0	0	69.7972	139.59

Table 5.1 Look up table

5.2.1. Case 1: Constant speed and load

This study case is done under 1 Nm of load when the machine was spinning at 10 rpm. Fig. 5.25 shows the response of the speed, it can be seen the estimated speed follows the reference but the real speed of the machine has many fluctuations. Electromagnetic torque has higher value than reference due to the value of the i_q is bigger than expected.

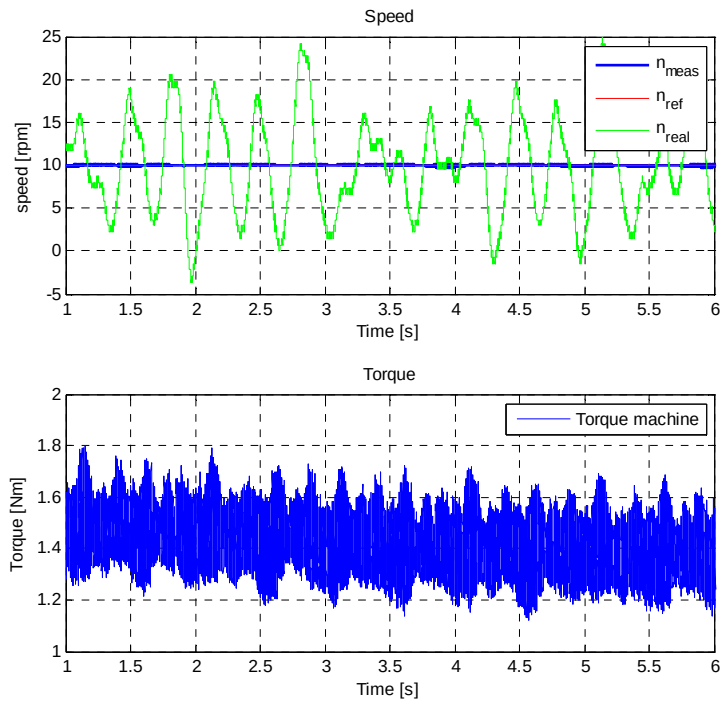

Fig. 5.25 Speed and torque response under 10 rpm and 1 Nm of load

In Fig. 5.26 the three phase currents are presented the high ripple in them is caused by the signal injection which superimposed to i_d is non zero due to the signal injection is applied in the *d*-axis, i_{qref} has oscillation between 2.1 and 1.9 A, this is reflected in the torque.

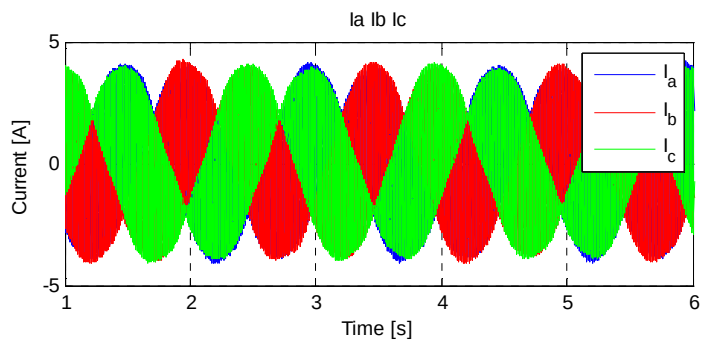

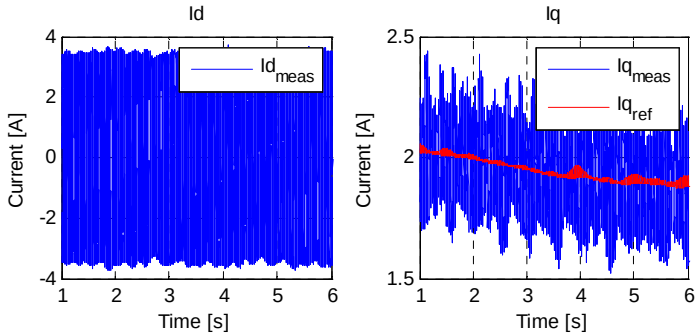

Fig. 5.26 Three phase and dq current responses under 10 rpm and 1 Nm of load

In Fig. 5.27 the estimated angle is presented. The labels show that the error is not constant due to the oscillations in the real speed.

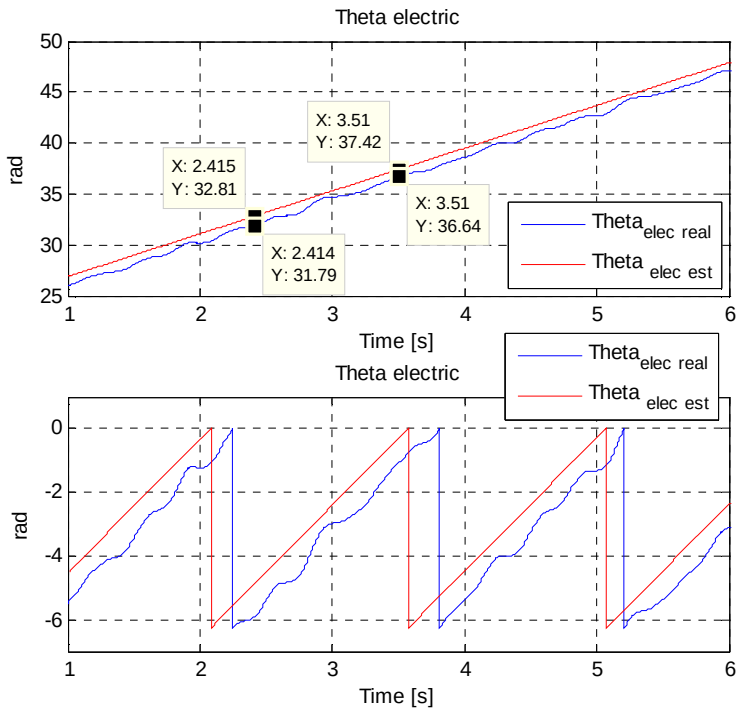

Fig. 5.27 Angle response under 10 rpm and 1 Nm of load

5.2.2. Case 2: Constant speed and no load

This study case is done running at 10 rpm and no load conditions. Fig. 5.28 shows the response of the speed and the angle. If a comparison is made with the previous case it can be observed that the error angle is bigger when there is not load applied to the shaft the machine.

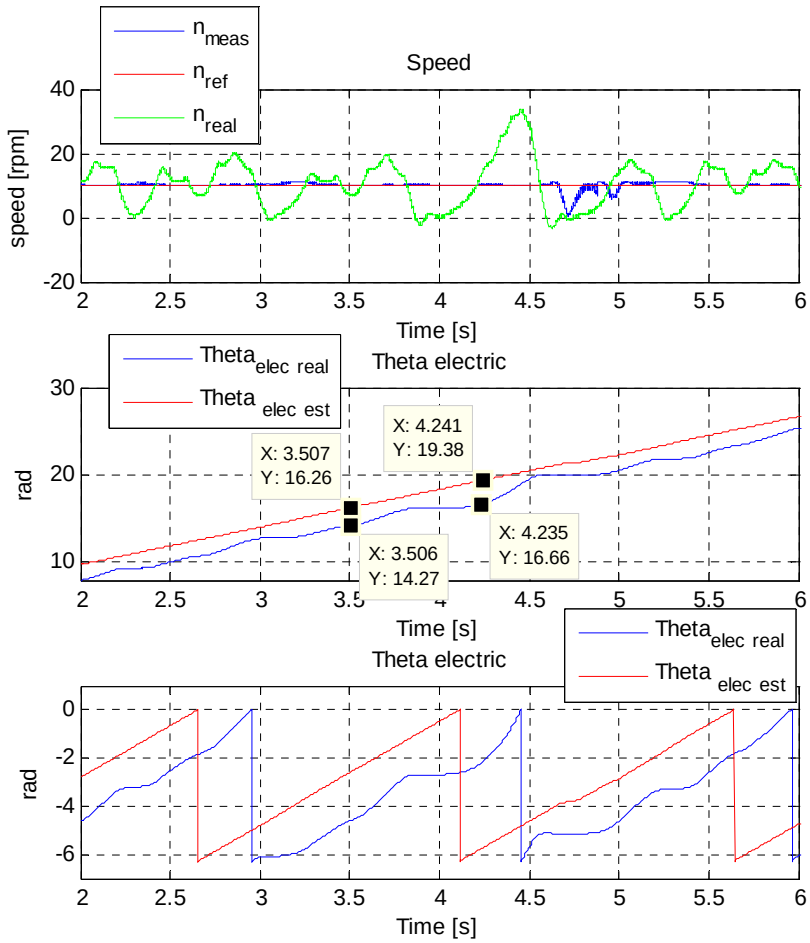

Fig. 5.28 Speed and angle response running at 10 rpm and no load conditions

5.2.3. Case 3: No load and reverse speed

A reverse speed applied to the drive under no load conditions. As in the previous cases the error angle is pretty big but even though the estimated speed tracks the reference.

The experiment shows the performance of the sensorless control when the mechanical speed command is varying from 10 rpm to -10 rpm under no load conditions.

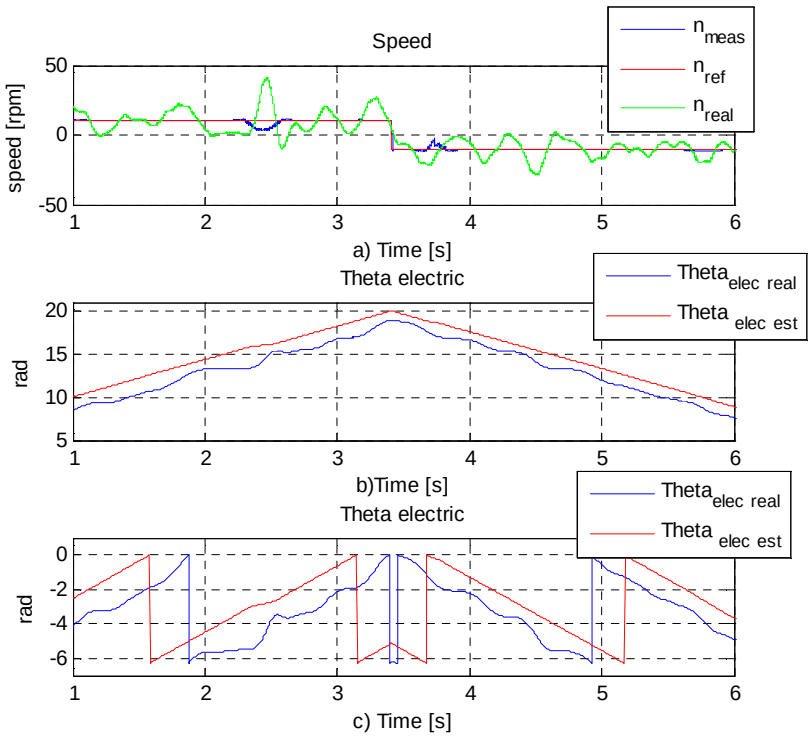

Fig. 5.29 Speed and angle response for a change to reverse speed

Fig. 5.30 and Fig. 5.31 show how the synchronization is realized when there is a reverse speed applied to the drive, in the first figure shows how the signal looks after the bandpass filter which has to be synchronized whit the injected sinus. The second figure shows how synchronization is applied when the machine has to spun in the opposite direction; diphase of 180 degrees is needed in order to get a negative DC component. When the high frequency signal is multiplied by the synchronization signal the result is a DC signal and the second harmonic.

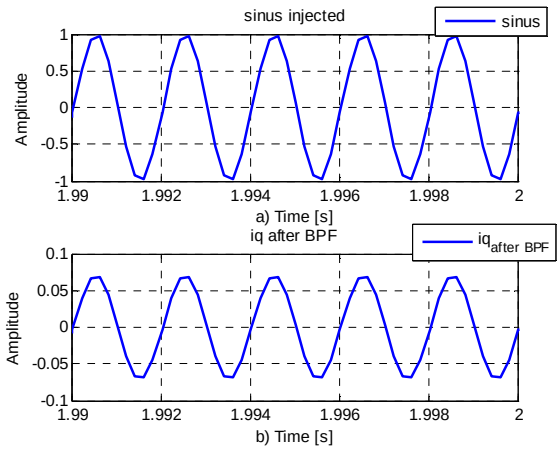

Fig. 5.30 Synchronization between the signal after the bandpass filter and the injected sinus

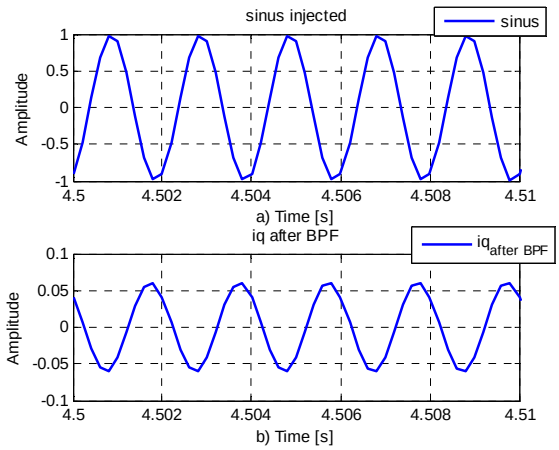

Fig. 5.31 Diphase of 180 degrees between the signal after the bandpass filter and the injected sinus when the machine has to spun in the opposite direction

As it was mentioned before and as can be notice from Fig. 5.32 a), the resultant signal has two components, the DC component which is negative when the speed changes direction, and the other one is the second harmonic which frequency is the double of the injected signal, that is presented in Fig. 5.33. Fig. 5.32 b) is the output of the low-pass filter.

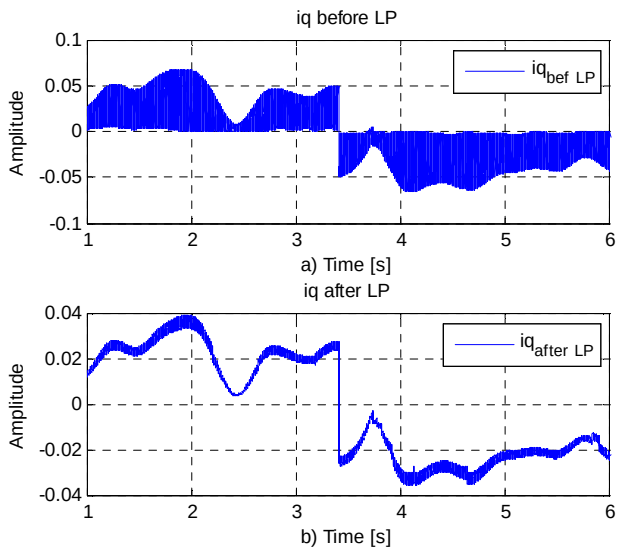

Fig. 5.32 Signal before and after the low-pass filter

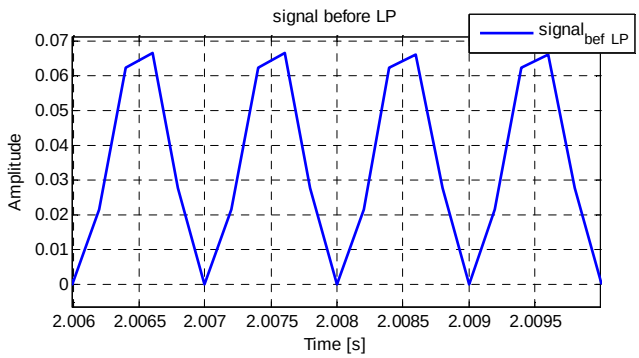

Fig. 5.33 Zoom of the signal before the low-pass filter

Performance of the system under unstable conditions

In order to validate the performance of the system in different working points, that means, bigger load torques and higher speed reference, many cases were tried in the lab with unsuccessful results. First assumption was a problem with the high harmonics in the surrounding area of the injected signal, due to the variation of these depending on the speed and load applied to the drive as it was presented in chapter 5.2. From the FFT analysis of the signal before and after the bandpass filter was determined that the harmonics were removed in the properly way by the propose filter. The Fig. 5.34 and Fig. 5.35 show the FFT analysis for increment in the load torque form 1 to 2 Nm at 10 rpm and step in the speed from 10 to 20 rpm with no load, respectively.

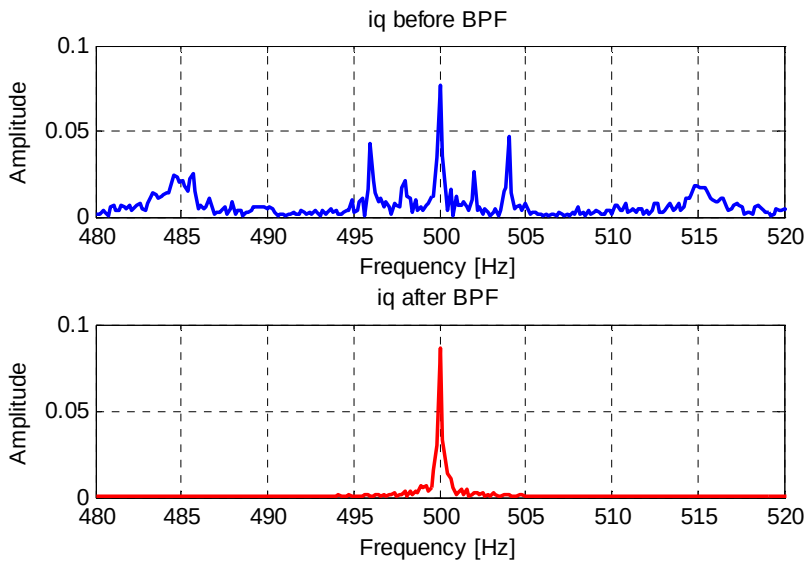

Fig. 5.34 FFT analysis of the signal before and after the bandpass filter at 10 rpm and a step in the load of 1Nm to 2 Nm

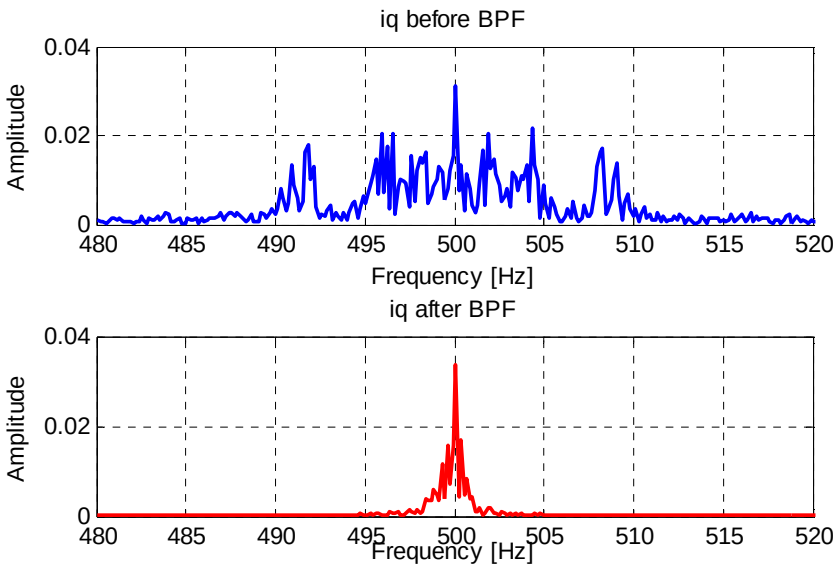

Fig. 5.35 FFT analysis of the signal before and after the bandpass filter for a step in the speed from 10 to 20 rpm with no load

After testing the bandpass filter the synchronization was studied in order to assess the properly performance. The cases mentioned before were also used in this point. In the figures Fig. 5.36 and Fig. 5.37 the left blue colour corresponds to the stable performance and the red right one is when the system becomes unstable. In both cases the synchronization is achieved all time even the system becomes unstable.

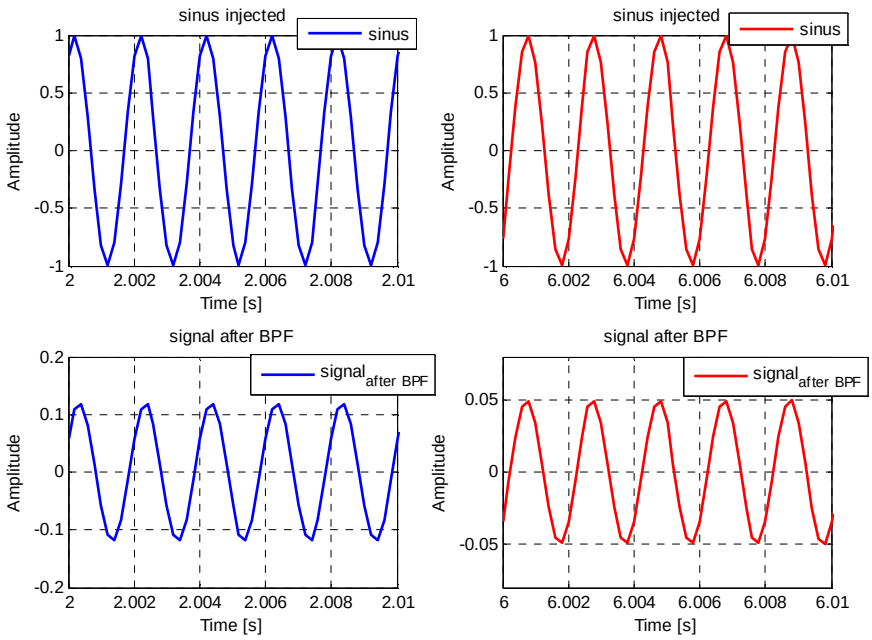

Fig. 5.36 Synchronization between the signal after the bandpass filter and the injected sinus at 10 rpm and a step in the load of 1Nm to 2 Nm

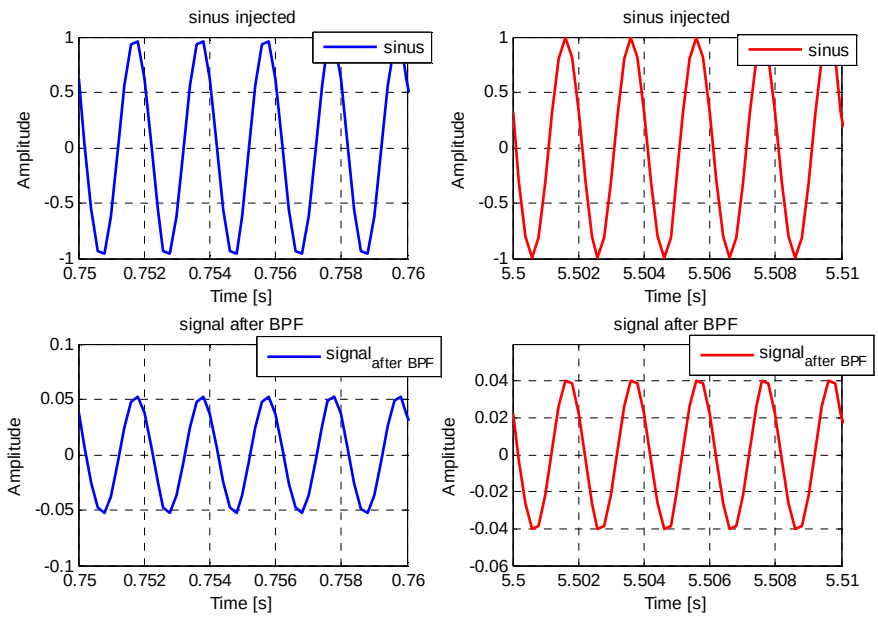

Fig. 5.37 Synchronization between the signal after the bandpass filter and the injected sinus for a step in the speed from 10 to 20 rpm with no load

Initial error

One of the main problems observed for all experiments in the lab was the large initial error between the estimated angle and real angle. When the load in the drive is applied the

error is smaller. Fig. 5.38 shows the case for 10 rpm and no load conditions and Fig. 5.39 shows the performance for the same speed and 1 Nm applied as a load.

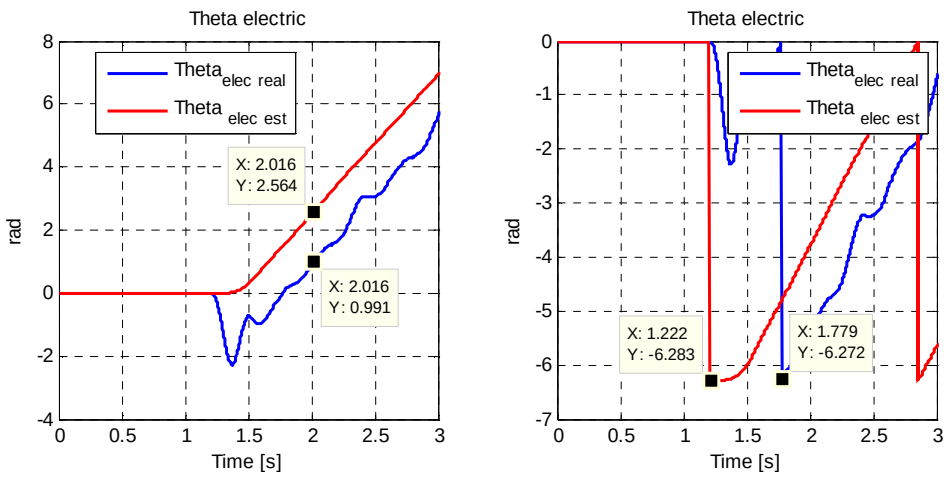

Fig. 5.38 Initial error between the estimated angle and real angle for 10rpm and no load conditions

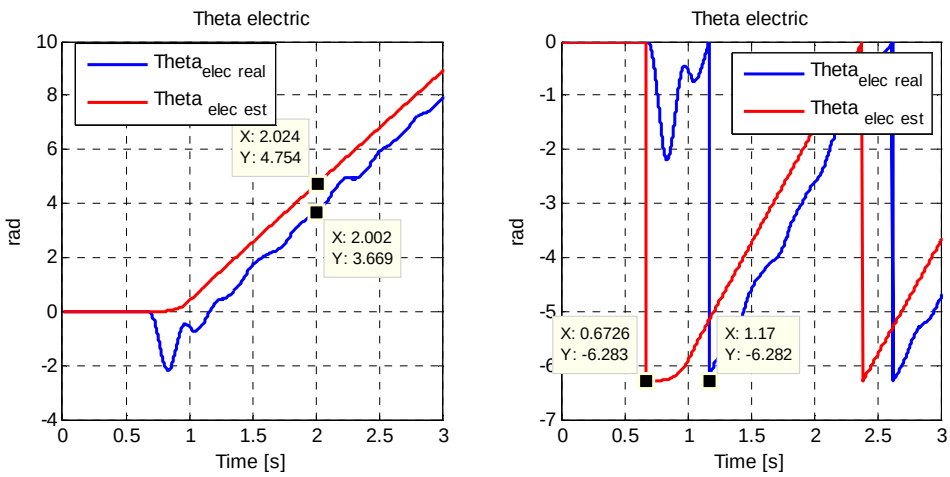

Fig. 5.39 Initial error between the estimated angle and real angle for 10rpm and 1Nm of load

In order to avoid the initial error different order of filters were implemented with unsuccessful results.

6. Conclusions

This project has the main scope to eliminate the encoder mounted on the shaft of a PMSM by implementing an algorithm from where the position and speed will be determinated.

Before implementing the algorithm in the laboratory is necessary to test the theoretical performance by using the simulations. Firstly, close loop FOC strategy with the sensor was implemented. In order to achieve a stable system and a properly tunning of the the PI . Finally the model was tested in Matlab/Simulink under different test Different sensorless methods were studied. The method chosen in this case is based on High frequency injection signal .

FOC with the sensor was implemented in dSpace laboratory. The results from the laboratory work shows good performance when the machine is running with and without load disturbance. Sensorless control was tested also in laboratory. During the laboratory test some drawbacks were presented, these are summarized below.

- Audible noise due to 500 Hz injection
- Oscillations in the mechanical speed especially when the machine is no loaded due to the speed estimator error
- High frequency harmonics in the surroundings of the injected frequency where present before the signal processing. For this reason, really narrow and high order bandpass filter is used.
- Firstly, an inconstant diphase between the output of the bandpass filter and the injected sinus did not allow the synchronization between both signals in the properly way. In order to avoid this drawback the zero cross detection for both signals was used in order to know the diphase between them each time that the signals cross zero. This diphase was added to the signal used to extract the orthogonal term of the output of the bandpass filter with satisfactory result.
- When the system becomes unstable under higher speed reference and more that 1 Nm of load torque some considerations were taking in account in order to validate the properly performance of the signal processing. That conclude, the unstable issue it does not come from this part of the algorithm.
- One of the main drawbacks in the achieved performance was a large starting error in the angle estimation which could not be neglected.

Future Work

- Improvement of the reliability of the sensorless algorithm applied.-
- Study how the parameters of the machine affect the reliability of the self sensing algorithm. Such as, effect of the stator resistance and polarity of the magnets.
- Implementation the algorithm for higher injected frequency.
- Study the effect of the non-linearity of the converter in the proposed algorithm.

References

1. **Zedong ZHENG, Yongdong LI, Xi XIAO and Maurice FADEL.** *Mechanical Sensorless Control of SPMSM Based on HF Signal Injection and Kalman Filter.* China : IEEE, 2008.

2. **Dong CHEN, Heng NIAN, Yikang HE and Lei HUANG.** *Sensorless Operation of PMSM by High Frequency Signal Injection Using the Field-Circuit Coupled Solution.* Seoul, Korea : IEEE, 2007.

3. **Ji-Hoon Jang, Jung-Ik Ha, Motomichi Ohto, Kozo Ide and Seung-Ki Sul.** *Analysis of Permanent-Magnet Machine for Sensorless Control Based on High-Frequency Signal Injection.* Seoul, Korea : IEEE, 2004.

4. **Trzynadlowski, Andrzej M.** *Control of Induction Motors.* Reno, Nevada : Academic Press, 2001. 0-12-701510-8.

5. **Zambada, Jorge.** *Sensorless Field Oriented Control of PMSM Motor.* s.l. : Microchip Technology Inc., 2007.

6. **Technologies, AG Infineon.** *Sensorless FOC for PMSM Motors.* Munchen : s.n., 2007.

7. **Neacsu, Dorin O.** *SPACE VECTOR MODULATION.* Cambridge : IEEE, 2001.

8. **Kazmeirkowski, Marian.** Marian Kazmeirkowski,R.Krishnan,Control in Power Electronics Selected Problems. [ed.] ISBN 0-12-402772-5. USA : Academic Press, 2002.

9. **Akmatov, V.** *Analysis of Dynamic Behavior of Electric Power Systems with Large Amount of Wind Power.* Lyngby : PHD Thesis, Technical University of Denmark, 2003.

10. **Pillay, P.** *Modeling of Permanent Magnet Motor Drivest.* s.l. : IEEE transaction of industrial electronics, vol 35, nº 4, 1998.

11. **Swierczynski, Dariusz.** *Direct Torque Control with Space Vector Modulation (DTC-SVM) of Inverter-Fed Permanent Magnet Synchronous Motor Drive.* s.l. : PHD Thesis, Warsaw University of Technology, 2005.

12. **Perera, Chandana.** *Sensorless Control of Permanent Magnet Synchronous Motor Drives.* s.l. : PhD Thesis, Aalborg University, 2002.

13. **Mizera, Roman.** *Modification of Symmetric Optimum Method.* Ostrava : Seminar, Instruments and Control, 2005.

14. **F.Franklin, Gene.** *Feedback control of dynamic systems.* USA : Prentice Hall, 2002. 0-13-0323934.

15. **Eskola, Matti.** *Speed and Position Sensorless Control of Permanent Magnet Synchronous Machine in Matrix Converter and Voltage Source Converter aplication.* Tampere : Tampere University, 2006.

16. **Rasmus ANDERSSON, Andreas GILLSTRÖM.** *Sensorless Control of a Permanent Magnet Syncronous Machine using Signal Injection.* Göteborg, Sweden : CHALMERS University of Technology, 2008.

17. **César Silva, Greg M. Asher and Mark Sumner.** *Hybrid Rotor Position Observer for Wide Speed-Range Sensorless PM Motor Drives Including Zero Speed.* Nottingham, U.K. : IEEE, 2006.

18. **David SALTIVERI, Antoni ARIAS, Greg ASHER, Mark Sumner, Pat WHEELER, Lee EMPRINGHAM and Cesar SILVA.** *Sensorless Control of Surface Permanent Magnet Synchronous Motor using Matrix Converters.* Nottinham, U.K. : Electrical Power Quality and Utilisation, 2006.

19. **Ji-Hoon Jang, Seung-Ki Sul, Jung-Ik Ha, Kozo Ide, and Mitsujiro Sawamura.** *Sensorless Drive of SMPM motor by High Frequency Signal Injection.* Seoul, Korea : IEEE, 2002.

20. **Mats Leksell, Lennart Harnefors, Hans-Peter Nee.** *Machine Design Considerations for Sensorless Control of PM Motors.* STOCKHOLM, SWEDEN : Electrical Machines and Drives KTH / Royal Institute of Technology, 1998.

21. **Semiconductor, Freescale.** *BLDC Sensorless Reference Design using MC56F8006.* 2009.

22. **Ltd, Dold Industries.** *Motor Brake Relays.*

23. **Canteli, Mario Mañana, et al.** *Three-Phase Adaptive Frequency Measurement Based on Clarke's Transformation.* s.l. : IEEE TRANSACTIONS ON POWER DELIVERY, VOL. 21, NO. 3, 2006.

24. **Young-doo Yoon, Seung-ki Sul, Shinya Morimoto and Kozo Ide.** *High Bandwidth Sensorless Algorithm for AC Machines Based on Square-wave Type Voltage Injection.* Seoul, Korea : IEEE.

25. **Universitet, Aalborg.** *Getting started with the dSpscr System.* Aalborg : Aalborg University, 2009.

Appendix A

Clark and Park transformations

The aim of this section is to introduce the essential concepts of reference frame theory (23). The three-phase voltages, currents and fluxes of AC-motors may be expressed in terms of complex space vectors (transformations are the same for all of them).

The *dq* transformation is done from the three phase stationary coordinate system to rotating dq coordinate system. This transformation can be split in two steps:

- *abc* to *αβ* (the Clarke transformation) which outputs a two co-ordinate time-variant system.
- *αβ* to *dq* (The Park transformation) which results in a two co-ordinate time invariant system.

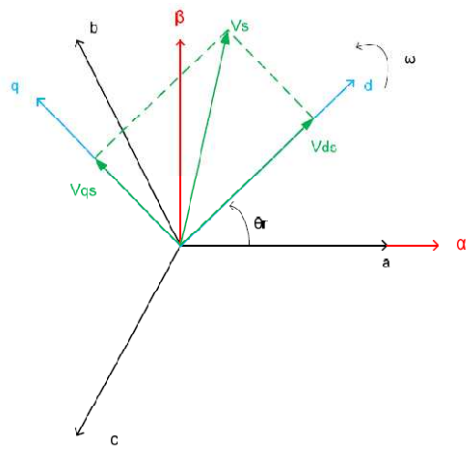

Fig. A.1Vectorial representation of abc, dq and αβ reference frames

- <u>*Clark transformation: The abc to αβ projection*</u>

With Clark Transformation is possible to separate the machine complex space vectors into real and imaginary part, and refer them to a stationary reference system. (5)

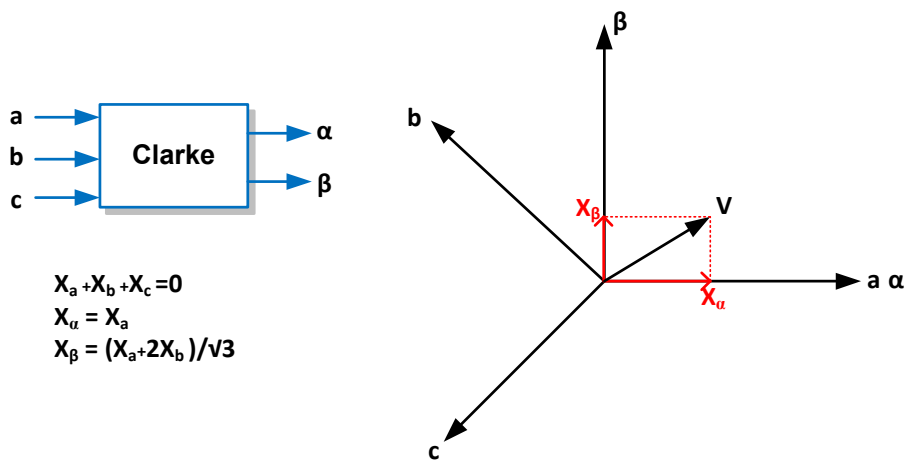

Fig. A.2 Clarke transformation

$$\begin{pmatrix} X_a \\ X_b \\ X_c \end{pmatrix} = \begin{pmatrix} 1 & 0 \\ -\frac{1}{2} & \frac{\sqrt{3}}{2} \\ -\frac{1}{2} & -\frac{\sqrt{3}}{2} \end{pmatrix} \begin{pmatrix} X_\alpha \\ X_\beta \end{pmatrix} \qquad \textit{Eq. A.1}$$

To transform from the stationary two axis frame to the stationary three axis frame of the stator the Inverse Clark transformation is used

$$\begin{pmatrix} X_\alpha \\ X_\beta \end{pmatrix} = \frac{2}{3} \begin{pmatrix} 1 & -\frac{1}{2} & -\frac{1}{2} \\ 0 & \frac{\sqrt{3}}{2} & -\frac{\sqrt{3}}{2} \end{pmatrix} \begin{pmatrix} X_a \\ X_b \\ X_c \end{pmatrix} \qquad \textit{Eq. A.2}$$

- *Park transformation: The αβ to dq projection*

This transformation modifies a two phase orthogonal system *αβ* in the *dq* rotating reference frame, that is rotating with the rotor flux. This two axis rotating coordinate system iscalled the d-q axis and represents the rotor angle.

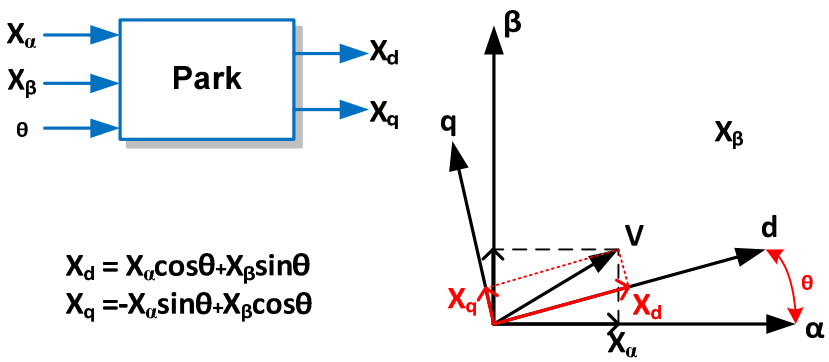

Fig. A.3 Park transformation

$$\begin{pmatrix} X_\alpha \\ X_\beta \end{pmatrix} = \begin{pmatrix} \cos(\theta) & -\sin(\theta) \\ \sin(\theta) & \cos(\theta) \end{pmatrix} \begin{pmatrix} X_d \\ X_q \end{pmatrix} \qquad \textit{Eq. A.3}$$

To transform from the two axis rotating d-q frame to the two axis stationary frame Inverse Park transformation is used

$$\begin{pmatrix} X_d \\ X_q \end{pmatrix} = \begin{pmatrix} \cos(\theta) & \sin(\theta) \\ -\sin(\theta) & \cos(\theta) \end{pmatrix} \begin{pmatrix} X_\alpha \\ X_\beta \end{pmatrix} \qquad \textit{Eq. A.4}$$

- *abc to dq and dq to abc projection*

abc → dq

$$\begin{pmatrix} X_d \\ X_q \end{pmatrix} = \frac{2}{3} \begin{pmatrix} \cos(\theta) & \cos\left(\theta - \frac{2\pi}{3}\right) & \cos\left(\theta + \frac{2\pi}{3}\right) \\ -\sin(\theta) & -\sin\left(\theta - \frac{2\pi}{3}\right) & -\sin\left(\theta + \frac{2\pi}{3}\right) \end{pmatrix} \begin{pmatrix} X_a \\ X_b \\ X_c \end{pmatrix} \qquad \textit{Eq. A.5}$$

dq → abc

$$\begin{pmatrix} X_a \\ X_b \\ X_c \end{pmatrix} = \begin{pmatrix} \cos(\theta) & \sin(\theta) \\ \cos\left(\theta - \frac{2\pi}{3}\right) & -\sin\left(\theta - \frac{2\pi}{3}\right) \\ \cos\left(\theta + \frac{2\pi}{3}\right) & -\sin\left(\theta + \frac{2\pi}{3}\right) \end{pmatrix} \begin{pmatrix} X_d \\ X_q \end{pmatrix} \qquad \textit{Eq. A.6}$$

Appendix B

Modula code

Mo_duty.c

The code was provided by Aalborg University and adapted for this project.

```
#include <math.h>
#include <stdlib.h>

#define SQRT3 1.73205

struct duty{
    float Da;
    float Db;
    float Dc;
};

double sign(double x)
{   if (x > 0.0)
        return 1.0;
    else
        return -1.0;
}


struct duty mo_duty(double valfa, double vbeta, double Vdc)
{
    double weight,dlimit,qlimit,t1,t2,temp;
    struct duty D;

    weight=(double) (Vdc/(SQRT3*sqrt(valfa*valfa+vbeta*vbeta)));
    dlimit=fabs(valfa*weight);
    qlimit=fabs(vbeta*weight);

    if (fabs(valfa)>dlimit)
    {
        valfa=(3*sign(valfa)*dlimit)/(2*Vdc);
    }
    else
    {
        valfa=(3*valfa)/(2*Vdc);
    }

    if(fabs(vbeta)>qlimit)
    {
        vbeta=(3*sign(vbeta)*qlimit)/(2*Vdc);
    }
    else
```

```
    {
        vbeta=(3*vbeta)/(2*Vdc);
    }
/*-------------------------- Modulation ---------------------------*/
if ((valfa>=0) && (vbeta>=0))
{
     if (vbeta < SQRT3*valfa)           /*Sector 0 */
     {
            t1=0.5*(valfa-(vbeta/SQRT3));
            t2=vbeta/SQRT3;
            temp=0.5-t1-t2;
            D.Da=1-temp;            /*Duty cycle A*/
            D.Db=1-(temp+2*t1);
            D.Dc=temp;
            return D;
      }
      else
      {                                 /*Sector 1 */
            t1=0.5*((vbeta/SQRT3)-valfa);
            t2=0.5*((vbeta/SQRT3)+valfa);
            temp=0.5-t1-t2;
            D.Db=1-temp;            /*Duty cycle*/
            D.Da=1-(temp+2*t1);
            D.Dc=temp;
            return D;
       }
}

if ((valfa<0) && (vbeta>0))
{
   if (vbeta < (SQRT3*fabs(valfa)))         /*sector 2*/
      {
            t1=(vbeta/SQRT3);
            t2=0.5*(fabs(valfa)-(vbeta/SQRT3));
            temp=0.5-t1-t2;
            D.Db=1-temp;              /*Duty cycle*/
            D.Dc=1-(temp+2*t1);
            D.Da=temp;
            return D;
      }
  else                                  /*sector 1*/
      {
        t1=0.5*((vbeta/SQRT3)-valfa);
        t2=0.5*((vbeta/SQRT3)+valfa);
        temp=0.5-t1-t2;
        D.Db=1-temp;            /*Duty cycle A*/
        D.Da=1-(temp+2*t1);
        D.Dc=temp;
        return D;
       }
}

if ((valfa<0) && (vbeta<=0))
```

```
{
   if (fabs(vbeta) <= SQRT3*fabs(valfa)) /*sector 3*/
       {
            t1=(fabs(vbeta)/SQRT3);
            t2=0.5*(fabs(valfa)-(fabs(vbeta)/SQRT3));
            temp=0.5-t1-t2;
            D.Dc=1-temp;             /*Duty cycle A*/
            D.Db=1-(temp+2*t1);
            D.Da=temp;
            return D;
       }
   else                                /*sector 4*/
       {
            t1=0.5*((fabs(vbeta)/SQRT3)-valfa);
            t2=0.5*((fabs(vbeta)/SQRT3)+valfa);
            temp=0.5-t1-t2;
            D.Dc=1-temp;             /*Duty cycle A*/
            D.Da=1-(temp+2*t1);
            D.Db=temp;
            return D;
       }
}

if ((valfa>=0) && (vbeta<0))
{
   if(fabs(vbeta)<=valfa*SQRT3)         /*sector 5*/
      {
            t1=0.5*(valfa-(fabs(vbeta)/SQRT3));
            t2=(fabs(vbeta)/SQRT3);
            temp=0.5-t1-t2;
            D.Da=1-temp;                 /*Duty cycle A*/
            D.Dc=1-(temp+2*t1);
            D.Db=temp;
            return D;
      }
   else /*sector 4*/
      {
            t1=0.5*((fabs(vbeta)/SQRT3)-valfa);
            t2=0.5*((fabs(vbeta)/SQRT3)+valfa);
            temp=0.5-t1-t2;
            D.Dc=1-temp;             /*Duty cycle A*/
            D.Da=1-(temp+2*t1);
            D.Db=temp;
            return D;
      }
}
}
```

Code in s-funton builder

Libraries tag

```
#include <math.h>
#include <stdlib.h>
#include "mo_duty.c"
struct duty A;
```

Output tag

```
A = mo_duty(valfa[0],vbeta[0],vdc[0]);

D[0]=A.Da;
D[1]=A.Db;
D[2]=A.Dc;
```

Appendix C

Experimental set-up

The equipment which has been used for the implementation of the generator side control strategy is shown in Fig. C.1. The experimental set-up follows the scheme introduced in Fig. 5.1 . (25)

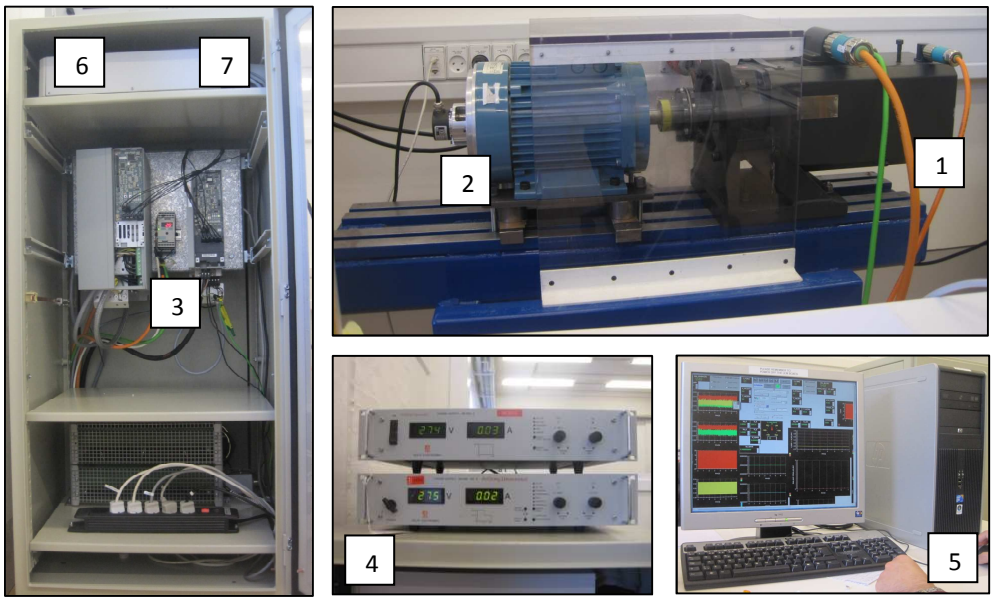

Fig. C.1: Physical layout of one FLEXIBLE DRIVE SYSTEM in dSpace Laboratory

1. PMSM
2. IM
3. Danfoss FC300 converter
4. DC sources
5. Control desk display
6. DS1103 PPC digital controller
7. Current/voltage measurement LEM-BOX

Specifications of the components

<u>Siemens PMSM type ROTEC 1FT6084-8SH7:</u>

- rated power: 9.4 kW
- rated torque = 20 Nm
- rated current = 24.5 A
- rated frequency = 300 Hz
- rated speed = 4500 rpm.

Danfoss FC300VLT (FC 302) frequency converter:

- rated voltage: input =3 phase AC 380 V, output = 3 phase AC 380 V
- rated output frequency = 0 .. 1000 Hz
- rated current: input = 5.3 A , ouput=5.6 A
- rated power = 4.3 kVA
- switching frequency = 3 .. 5 kHz

DS1103 PPC

- Motorola PowerPC 604e running at 333 MHz
- Slave DSP TI's TMS320F240 Subsystem
- 16 channels (4 x 4ch) ADC, 16 bit , 4 µs, ±10 V
- 4 channels ADC, 12 bit , 800 ns, ± 10V
- 8 channels (2 x 4ch) DAC, 14 bit , ±10 V,6 µs
- Incremental Encoder Interface -7 channels
- 32 digital I/O lines, programmable in 8-bit groups
- Software development tools (Matlab/Simulink, RTI, RTW, TDE, Control Desk)

The DS1103 PPC card is pluged in one of the ISA slot of the motherboard of a host computer of the type PII/400MHz, 128 MBRAM, 6GB HDD, Windows NT 4.0. All the connection are made through six flat cables (50 wires each) available at the backside of the desktop computer.

The dSPACE DS1103 PPC is a mixed RISC/DSP digital controller providing a very powerful processor for floating point calculations as well as comprehensive I/O capabilities.

The IM is fed by a frequency converter (Danfoss VLT5004 converter with a IPC2 board) controlled directly by the DS1103 so a great deal of loading-torque characteristics can be achieved.

Appendix D

List of parameters

Parameter	Value	Unit
Rated phase voltage	164	V
Rated speed	4500	rpm
Rated current	20	A
Rated Power	9.42	kW
Rated torque	20	Nm
Stator phase resistance	0.19	Ω
Synchronous inductances	2	mH
Number of pole pairs	4	-
Permanent magnet flux linkage	0.123	Wb
Rotor moment of inertia	0.0048	Kg·m^2

Table D.1 sPMSM parameters

Appendix E

Simulink models

Field Oriented Control

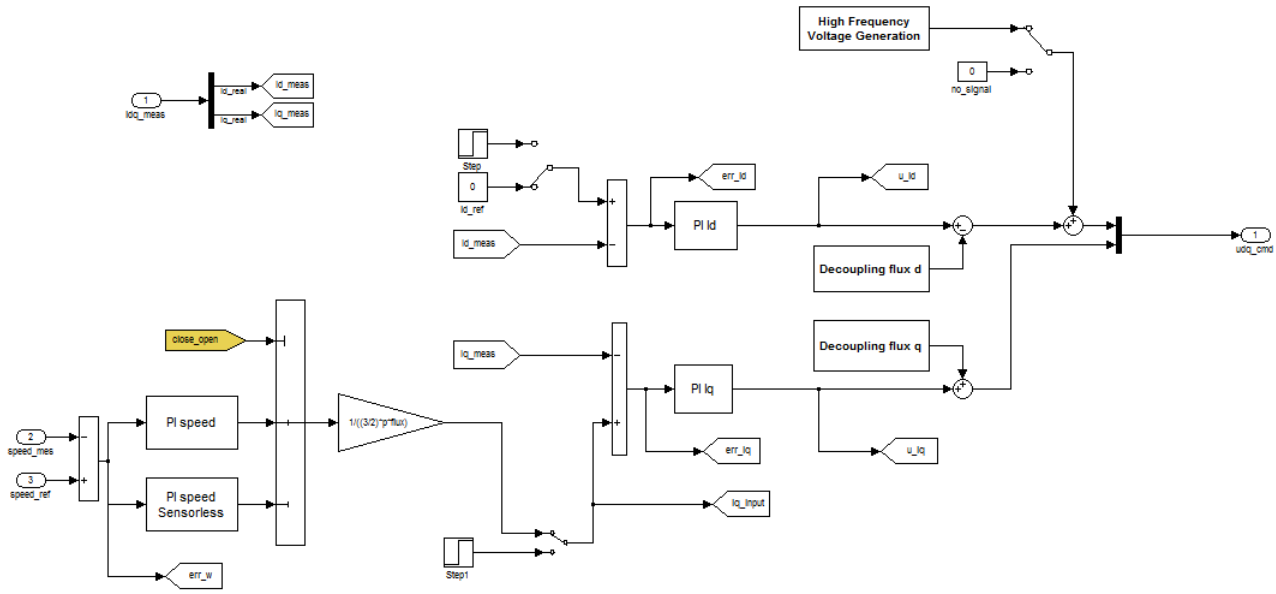

PMSM *dq* model

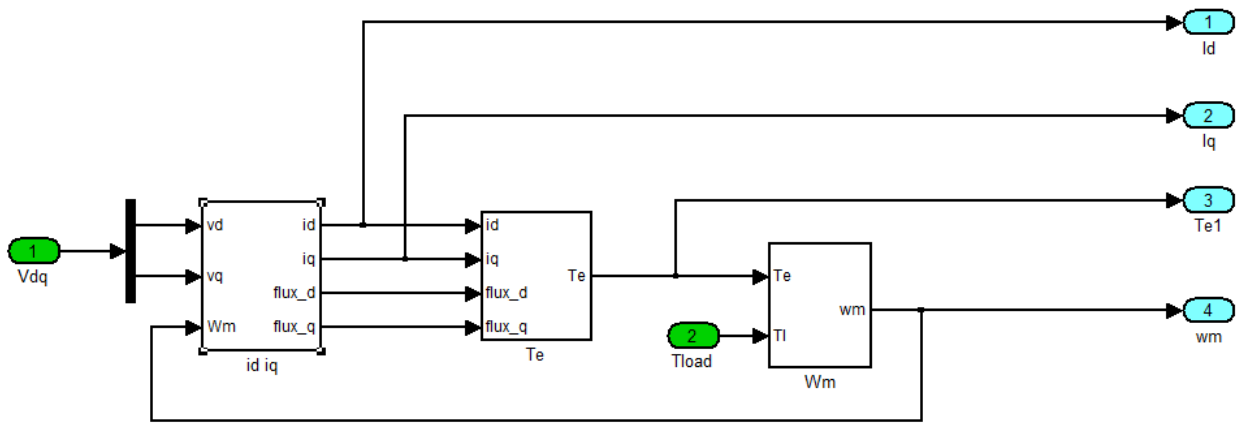

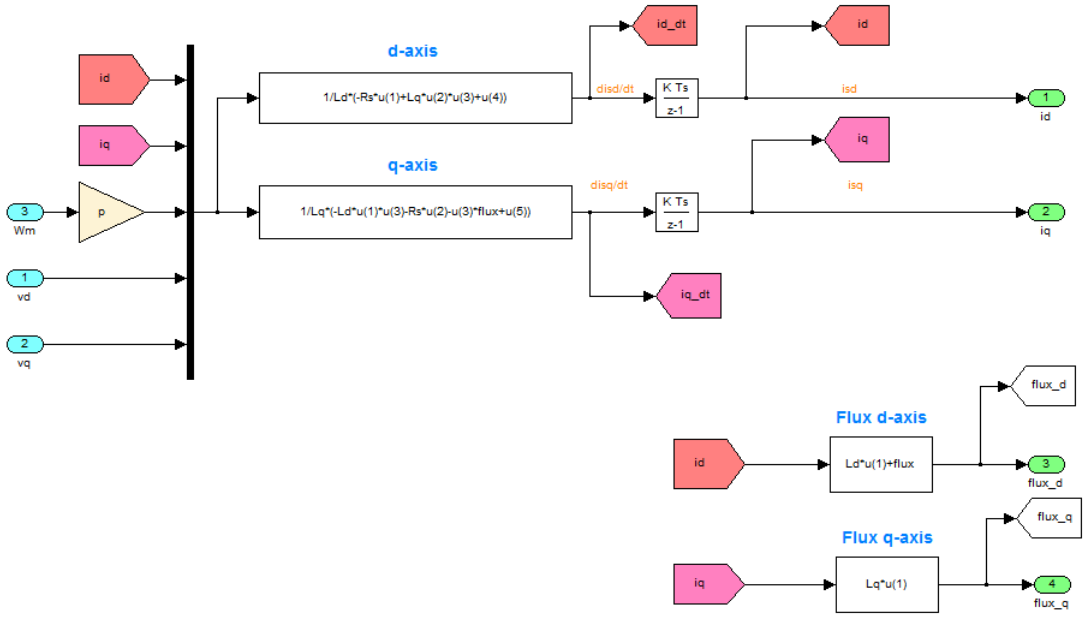

Space Vector Modulation

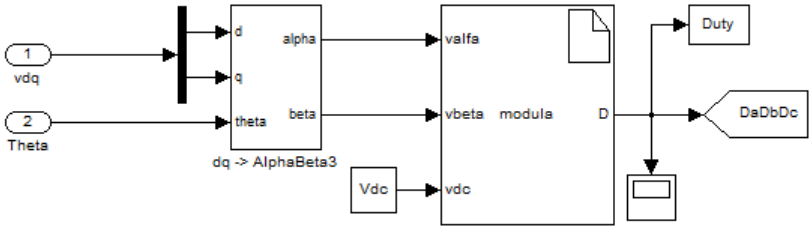

Converter

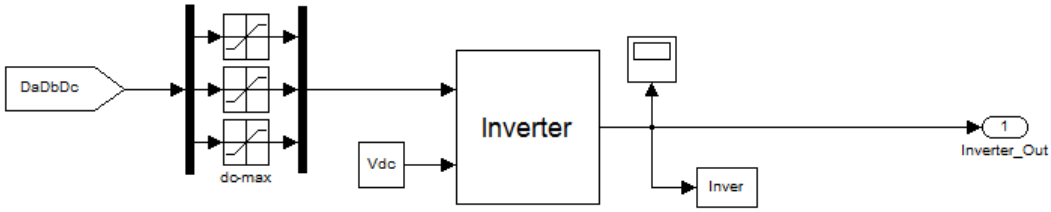

Current filters

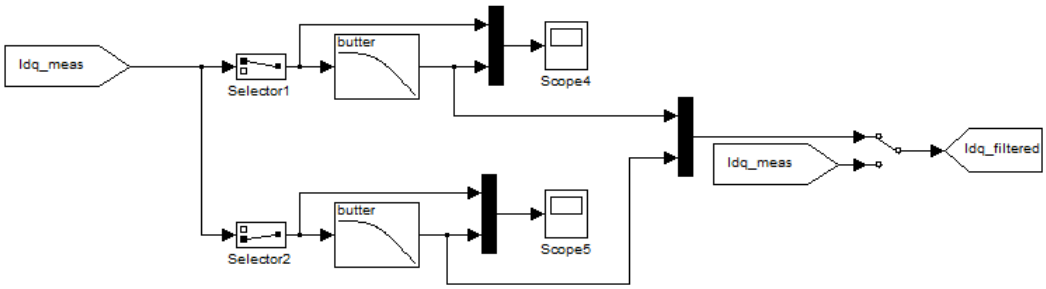

Signal processing

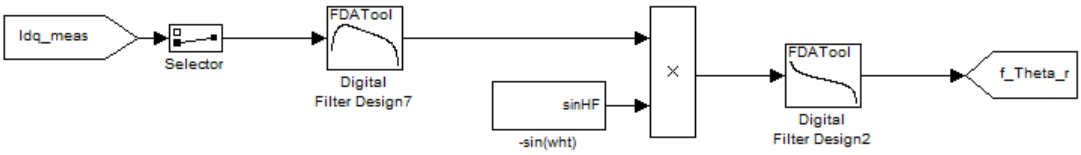

Rotor position and speed estimator

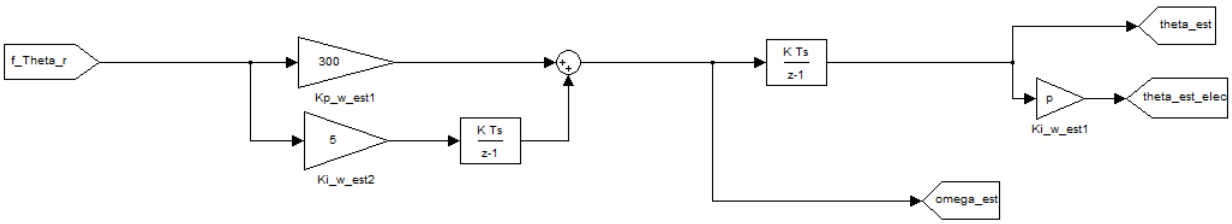

Appendix F

Contents of CD

- Report
  - Word
  - Pdf
- References
- Simulation Files
- Laboratory Files